Constraint-Induced Crack Initiation and Crack Growth at Electrode Edges in Piezoelectric Ceramics

dem Fachbereich Material- und Geowissenschaft
der Technischen Universität Darmstadt

zur Erlangung des akademischen Grades
Doktor - Ingenieur
(Dr.-Ing.)

genehmigte Dissertation von
Dipl.-Ing. Sergio Luis dos Santos e Lucato
aus São Paulo, Brasilien

Referent:	Prof. Dr. J. Rödel
Koreferent:	Prof. Dr. H. von Seggern
Tag der Einreichung:	11. Januar 2002
Tag der mündlichen Prüfung:	12. Februar 2002

Darmstadt 2002
D17

Diese Arbeit wurde im Fachbereich Material- und Geowissenschaften, Fachgebiet Nichtmetallisch-Anorganische Werkstoffe unter der Leitung von Prof. Dr. J. Rödel in der Zeit von April 1999 bis Januar 2002 angefertigt.

Trademarks

The following names used in this work are trademarks of their owners:

Leica QWin®, Leica Quips®, Chemtronics CircuitWorks®, 3M Flourinert®, Ansys®, Fischertechnik®, Nylon®, Voltcraft®

Acknowledgements

I would like to thank all the people who helped me during this work. First of all, I would like to thank Prof. Jürgen Rödel and Dr. Doru Lupascu for the interesting topic, the scientific support, and all the friendly and helpful discussions.

Some parts of this work were only possible with cooperation partners. I would like to thank Dr. Bahr, Dr. Van-Bac Pham, Prof. Balke, Prof. Bahr and their group from the Dresden University of Technology for the fracture mechanical analysis and Dr. Marc Kamlah from the Forschungszentrum Karlsruhe for the non-linear finite element analysis. Nils Hardt and Thorsten Fugel from the High Voltage Institute were of very valuable help with the high-voltage equipment.

I would like to thank Prof. Chris Lynch and his group from the Georgia Institute of Technology in Atlanta for the very instructive times in Atlanta as well as Lisa Mauck and Thomas Karastamatis for their help with all the needs of a student in Atlanta. I would furthermore like to thank Prof. Robert McMeeking, Prof. Fred Lange and their groups, especially Michael Pontin, for the very friendly and interesting discussions during my short trip to the University of California at Santa Barbara.

I would like to thank Emil Aulbach and Herbert Hebermehl for their help preparing my specimens and Roswitha Geier for her endless patience with the paperwork I provided. Jürgen Nuffer helped me a lot learning the details of this tricky material. The discussions with my roommate Astrid Dietrich were always very helpful and enjoyable. Thank you and all the other members of the group.

I thank the Deutsche Forschungsgemeinschaft and the Deutscher Akademischer Austauschdienst for their financial support.

I would like to thank my friends and my parents for their help and support during the past years. They helped me to see things from another standpoint, something invaluable for new ideas and new solutions. And sometimes it was that glass of wine we had together that helped to forget and restart, once I reached a dead-end.

For enduring my chaos, her love and her neverending support and patience throughout the past years I would like to very specially thank my wife Heike.

Preface

Piezoelectric ceramic actuators are nowadays used for numerous applications in adaptive structures and vibration control [1, 2]. Respective components have been accepted in the aircraft and automobile industry as well as in printing and textile machinery. Albeit exhibiting some ferroelastic toughening, the fracture toughness of ferroelectric actuator materials is rather small. They are susceptible to fracture under high electric fields or mechanical stresses. Therefore, the limited reliability of the component due to cracking constitutes a major impediment to large scale usage.

A cost efficient geometry for actuators with large displacements is that of the cofired multilayer geometry. The common design consists of two interdigitated electrodes. This geometry carries the disadvantage of electrodes ending inside the ceramic. As a consequence, the ceramic material, which exhibits ferroelectric, ferroelastic as well as piezoelectric behavior, experiences a strain incompatibility between the electrically active and inactive material regions. A complex mechanical stress field originating at the electrode edge arises and can lead to crack initiation in this area, crack growth, and finally to the failure of the device.

To obtain a better understanding of the underlying mechanisms crack nucleation and crack propagation have to be separated. In ferroelectric ceramics crack nucleation is governed by statistics of defects. Knowledge of the geometrical and electrical conditions resulting in critical stresses is therefore required. After crack initiation the crack propagation is the dominant mechanism which is characterized by an equilibrium of crack driving and crack resistance forces. Both are highly dependent on the geometry and the applied boundary conditions.

The present work provides a study of crack nucleation as well as crack propagation in model geometries under various electrical and mechanical boundary conditions. Non-linear finite element modelling and fracture mechanical analysis are used to investigate the material response and the equilibrium conditions.

A close cooperation with the Dresden University of Technology and the Forschungszentrum Karlsruhe for the modelling aspects is part of this work. Consequences of the modelling requirements are included in the choice of the specimens and experiments. Parts that were partly or in whole result of the cooperation partners are marked at the beginning of each section. They are included in this thesis as the experimental work was designed for the modelling and therefore the experimental results have to be read in the context of the modelling results.

Contents

Preface **v**

1 Introduction **1**

1.1 Ferroelectric and Ferroelastic Materials 1

1.1.1 Piezoelectricity 1

1.1.2 Ferroelectricity and Ferroelasticity 2

1.1.3 Lead - Zirconate - Titanate System 4

1.1.4 Investigated Material 5

1.1.5 Multilayer Actuators 6

1.2 Fracture Mechanics 7

1.2.1 Crack Propagation Behavior 7

1.2.2 Crack Deflection 10

1.3 Fracture Mechanisms of Piezoceramics 12

1.3.1 Material Behavior 12

1.3.2 Damage in Multilayer Actuators 14

1.4 Behavior of Cracks under Strain Incompatibility 16

1.4.1 Thermally Induced Strain Incompatibility 16

1.4.2 Electrically Induced Strain Incompatibility 19

2 Crack Initiation **21**

2.1 Experimental Methods 21

2.1.1 Specimen Preparation 21

2.1.2 Strain and Coercive Field Measurement 22

2.1.3 Mapping of the Crack Pattern 23

2.1.4 Evolution of the Crack Pattern 24

2.2 Experimental Results 24
    2.2.1 Strain 24
    2.2.2 Coercive Field 27
    2.2.3 Crack Patterns 27
    2.2.4 Crack Pattern Evolution 29
2.3 Finite Element (FE) Analysis 29
    2.3.1 Linear Piezoelectric FE Analysis 29
    2.3.2 Non-Linear Piezoelectric FE Analysis 31
2.4 Finite Element Results 33
    2.4.1 Linear Piezoelectric FE Results 33
    2.4.2 Non-Linear Piezoelectric FE Results 35
2.5 Discussion 35
    2.5.1 Local Effect 35
    2.5.2 Global Effect 37
    2.5.3 Thickness Effect 38

3 Mechanically Driven Crack Growth 41
3.1 Experimental Methods 41
    3.1.1 Specimen Preparation 41
    3.1.2 Poling 42
    3.1.3 R-Curve Measurement 42
3.2 Experimental Results 44
    3.2.1 Thickness Dependence of R-Curves 44
    3.2.2 Polarization Dependence 46
3.3 Discussion 46
    3.3.1 Thickness Dependence 46
    3.3.2 Polarization Dependence 48

4 Electrically Driven Crack Growth 51
4.1 Experimental Methods 51
    4.1.1 Specimen Preparation 51
    4.1.2 Poling 53

4.1.3 Displacement Measurement 54
4.1.4 Crack Propagation Measurement 54
4.2 Experimental Results 56
4.2.1 Measured Displacements 56
4.2.2 Crack Propagation Measurement 58
4.2.2.1 Crack Shapes 58
4.2.2.2 Crack Length as a Function of Electric Field 62
4.3 Quantitative Fracture Mechanical Analysis 68
4.3.1 Finite Element Model 68
4.3.2 Stress Intensity Factor for a Straight Crack 70
4.3.3 Curved Crack Shape Simulation 71
4.3.4 Crack Extension 73
4.4 Discussion 76

5 Summary 81

A Details on the Modelling of Crack Propagation 83
A.1 Calculation of the Incompatible Strains 83
A.2 Calculation of the Stress Intensity Factors for the Applied Load 84

B Custom Software 85
B.1 Data Logging Software 85
B.2 Connection to the Leica Microscope Software QWin 86
B.3 Crack Mapping Software 87
B.4 R-Curve Measurement Software 88

C Tables 89

Bibliography 91

Symbols 97

Zusammenfassung 101

Chapter 1

Introduction

1.1 Ferroelectric and Ferroelastic Materials

Only a brief introduction into the concept of piezoelectricity, ferroelectricity and ferroelasticity along with the basic relationships is given here. A more detailed description can be found in standard textbooks [3, 4, 5, 6].

1.1.1 Piezoelectricity

If an electric field E is applied to a material, the internal charge centers are displaced relative to each other and a polarization $P_i = \varepsilon_0 \chi_{ij} E_j$ is induced. The polarization can depend on other parameters such as temperature and mechanical stress or be the result of a phase transition in a crystal. The polarization is added to the vacuum dielectric displacement to yield the total dielectric displacement D:

$$D_i = \varepsilon_0 E_i + P_i = \varepsilon_0(\delta_{ij} + \chi_{ij})E_j = \varepsilon_{ij} E_j. \tag{1.1}$$

In almost all substances without a symmetry center (the point group 432 is an exception due to its high symmetry [7]) the polarization can also be induced by a mechanical stress σ. Such substances are called *piezoelectric* and for small stresses and no electric field the piezoelectric effect is described by the relationship $P_i = d_{ijk}\sigma_{jk}$ with d being the piezoelectric modulus. The dielectric displacement in such substances now depends on the applied electric field and the mechanical stress:

$$D_i = \varepsilon_{ij} E_j + d_{ikl}\sigma_{kl} \tag{1.2}$$

The piezoelectric effect can also be reversed such that an applied electric field yields a mechanical strain $S_{jk} = d_{ijk}E_i$ which is known as the converse piezoelectric effect. By the electro-mechanical coupling the total strain of the specimen is now given by an electrical and a mechanical argument:

$$S_{jk} = d_{ijk}E_i + s_{jklm}\sigma_{lm} \tag{1.3}$$

Only the induced polarization has been introduced so far, but there are substances with a so called spontaneous polarization P^S without an applied external field. The spontaneous electric moment p^S of a unit cell is given as sum of all electronic and atomic dipoles $\sum_j^N p_j$. Summation over all unit cells of a crystal yields the macroscopic spontaneous polarization. The direction of the polarization is called the polar axis. In crystalline substances the direction of the polar axis is given by the crystal structure.

1.1.2 Ferroelectricity and Ferroelasticity

The microscopic and the macroscopic polar axis are usually identical but in some substances the direction of the microscopic polar axis can vary within a crystal. Depending on the actual material the direction and polarity of the local polar axis can be changed by an external electric field. That effect is called *ferroelectricity*. Similarly the term *ferroelasticity* classifies a remnant deformation by a stress field.

The basic mechanism of reorientation will be discussed for a tetragonal unit cell shown in figure 1.1. Due to the crystal structure only reorientation angles of 90° and 180° are possible. An applied electric field above a certain threshold will interact with the dipoles and reorient (or switch) it to the field direction. The threshold is called *coercive field* E_C. Fields below the coercive field will only lead to a reversible distortion but not to a permanent reorientation.

While 90° and 180° switches are possible by the ferroelectric effect, ferroelasticity is by definition associated with a deformation. The 180° switch does not result in a deformation and can therefore not be invoked by a stress field. Only 90° switching is possible ferroelastically. A compressive stress along the long axis will switch the unit cell to one of the four possible perpendicular directions. Tensile stresses will lead to switching in one of the two directions parallel to the stress. As for the electric field, the stress has to pass a threshold value, the *coercive stress* σ_C, to induce switching.

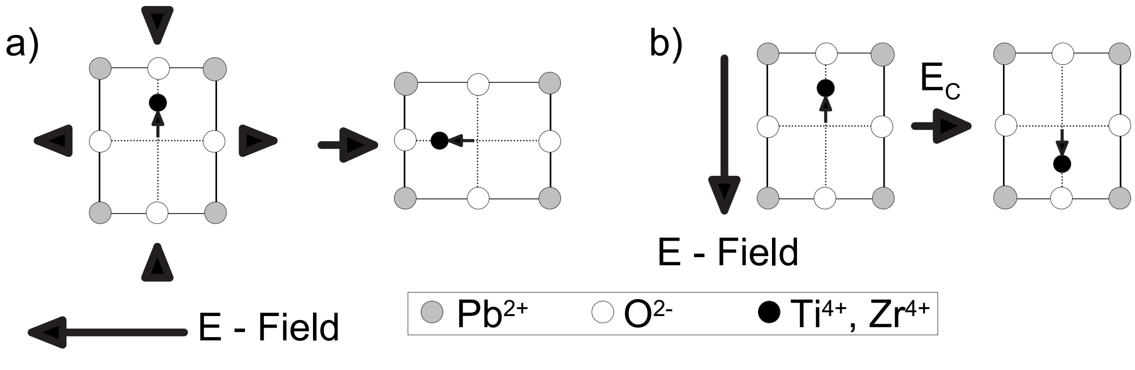

Figure 1.1: Schematic representation of the unit cell reorientation by electric and stress fields. The tetragonal structure of the PZT-system was chosen for simplicity reasons. a) 90° switching and b) 180° switching.

More generally the switching criterion is given by an energy argument. The unit cell will switch if the sum of mechanical and electrical energy is greater than a critical energy given by the spontaneous polarization and the coercive field [8]:

$$W_{mech.} + W_{el.} \geq W_{crit.} \Leftrightarrow \sigma_{ij}\Delta S_{ij} + E_i \Delta P_i \geq 2P^S E_C \tag{1.4}$$

Δ designates the difference between the state before and after switching. Eqn. 1.4 is given in the local coordinate system of the unit cell. The electric field and the stress tensors are the orthogonal projection of the externally applied fields.

In ferroelectric and ferroelastic materials the relationships in eqns. 1.2 and 1.3 are approximately linear only for small stresses and low electric fields. The tensors d, ε and s depend on the polarization state of the material. At high fields the relations become highly non-linear and hysteretic as shown in figure 1.2 for the electric field. Furthermore, the above described domain processes are mostly reversible and time-dependent [9] with according implications on the material properties.

In a polycrystalline material the macroscopic switching is not as sharp as the above described microscopic behavior for two reasons. The domains will usually not be oriented parallel to the external field. A higher external field has to be applied to yield the coercive field in the projection. The most favorably oriented domains will switch first while others need a higher external field. Switching also incorporates a mechanical deformation. Neighboring domains have a different orientation such that switching would lead to high mechanical stresses. The associated mechanical energy has to be compensated electrically. An applied external mechanical pressure parallel to the electric field for example increases the required electric field [10] due to a similar energy argument. The grain size will also have an effect such that larger grains exhibit a lower coercive field [11].

A new definition of the coercive field is needed for ceramics because the switching is not as sharp as on the unit cell level. Usually the intersection of the dielectric hysteresis loop with

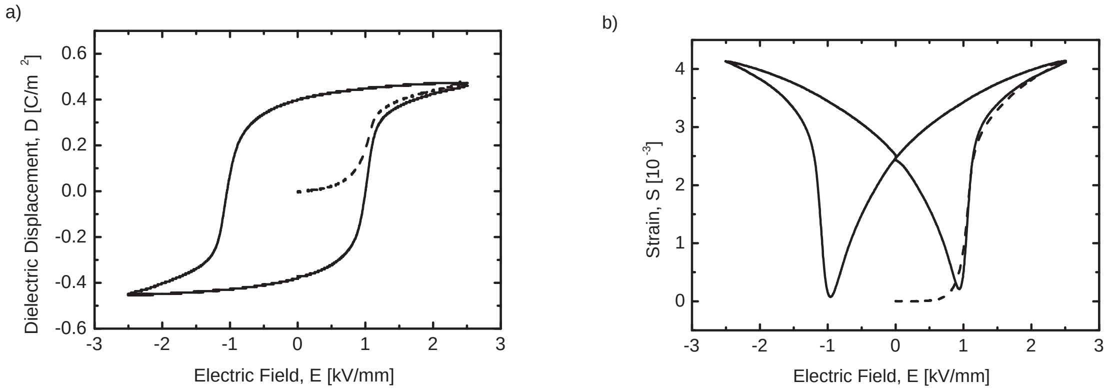

Figure 1.2: Hysteretic behavior of a) the dielectric displacement and b) the strain in field direction for the investigated material. The first poling of a virgin material is shown as dashed line.

the abscissa is used. In case of the first loop no intersection exists and therefore the inflexion point of the strain loop is used in this work, which is a good approximation for the investigated material as it can be seen in figure 1.2.

Since the grains in a crystalline material are randomly oriented the initial net external polarization and strain are zero. If an external field is applied, some domains will be oriented more favorably, and will grow by domain wall motion. At high fields most of the domains have switched and no further switching is obtained by higher fields. The situation is now a superposition of domain switching and piezoelectricity. If the external field is removed the converse piezoeffect will reduce to zero. Because of mechanical misfit stresses that were compensated by external fields some domains will switch back but most will remain. The permanent value after removal of the field is termed *remnant polarization* P^R or *remnant strain* S^R, respectively. The material is now macroscopically polarized and thus piezoelectric. This first poling is shown as dashed line in figure 1.2.

1.1.3 Lead - Zirconate - Titanate System

For actuator applications the lead-zirconate-titanate (PZT) system is the most widely used because of it's high electro-mechanical coupling [12]. The system crystallizes in the cubic perovskite structure with lead on the edges, oxygen in face centers and zirconium and titanium in the body center. Cooling the material below the Curie-temperature T_C a phase transformation into the tetragonal, rhombohedral or orthorhombic structure occurs depending on the Zr^{4+}/Ti^{4+} concentration (figure 1.3). The boundary between the tetragonal and rhombohedral forms is nearly independent of temperature (morphotropic) and is marked by coexistence of both phases. The exact compositions and shape is subject of ongoing research [13].

The distortion from the cubic phase beneath T_C is governed by the size of the central ion. There are several equivalent directions of the distortion and, therefore, of the polar axis for each structure. In the tetragonal structure these are the [001] directions with six possible configurations (two on each axis). Reorientation angles of 90° and 180° are possible. The rhombohedral structure offers eight configurations along the diagonal [111]-directions with angles of 71°, 109° and 180°. While all reorientations can be invoked ferroelectrically, it is obvious that the 180° reorientation can not be invoked ferroelastically as no deformation results therefrom.

Besides the Zr^{4+}/Ti^{4+}-concentrations the electro-mechanical properties can be altered by doping. Acceptor-ions such as Fe^{3+}, Mn^{2+} and Ni^{2+} on Ti^{4+} or Zr^{4+} sites will result e.g. in a high coercive field and are called *hard ferroelectrics*. In order to maintain charge neutrality oxygen vacancies are introduced that form dipoles with the dopant-ion and hinder domain wall motion [3]. Such materials are used in ultrasonic applications. Materials for actuator applications need lower coercive fields and especially a large piezoelectric coupling. This is achieved with donor-dopants as La^{3+}, Nb^{5+}, Bi^{3+}, Sb^{5+} and others occupying the lead or titanium / zirconium positions depending on their size [4]. Such materials are called *soft ferroelectrics*. The terms hard and soft have their analogy in magnetism.

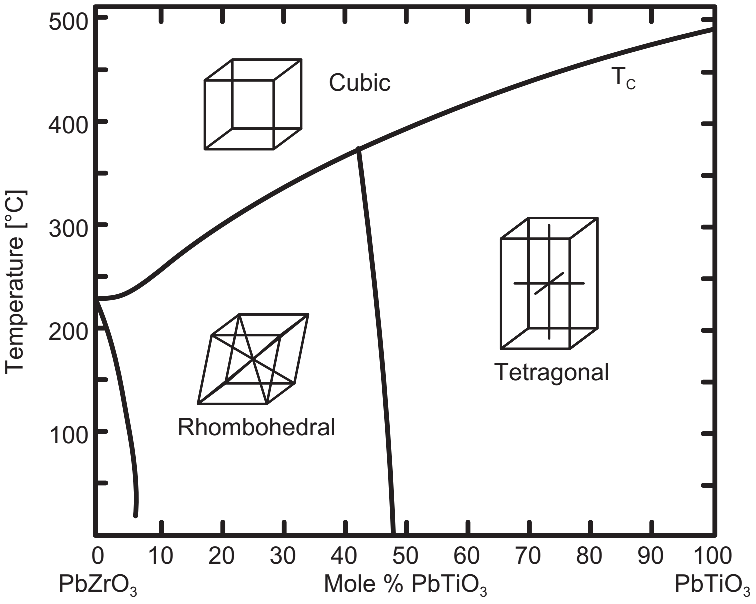

Figure 1.3: Phase diagram of the Lead - Zirconate - Titanate System. The possible orientations of the central ion and thus the polar axis are shown in the inserts [1].

1.1.4 Investigated Material

All experiments in this work were performed on a commercial lead-zirconate-titanate material (PIC 151, PI Ceramics). It is a tetragonal nickel and antimony doped soft PZT material near the morphotropic phase boundary. The exact composition as given by the manufacturer is $Pb_{0.99}[Zr_{0.45}Ti_{0.47}(Ni_{0.33}Si_{0.67})_{0.08}]O_3$. A detailed discussion of this composition can be found in [14]. One of the problems with this composition is the high vapor pressure of the antimony during sintering. Thus, the grain size is controlled by the antimony content so that small variations of the sintering process can lead to different grain sizes even for identical powders with the already discussed consequences on the material properties.

The material is produced by the “mixed-oxide-process” used for other oxide ceramics. Raw material ground to fine powder is wet-chemically homogenized, dried and calcinated. This product is used for sintering. The sintering has to be done with a PbO excess because of the high vapor pressure of PbO. Variations in the PbO content lead to large variation of the material properties.

To ensure minimal material variations specimens of only one reserved powder batch were used for all experiments. A total of five sinter batches (denoted by S1 - S5) were used. The first two batches (S1 and S2) were used during the previous work characterizing the polarization and grain size dependence of the R-curve [15]. In the present work only the batches S3 through S5 were used.

1.1.5 Multilayer Actuators

If large actuation is needed actuators made of a piezoceramic require a considerable height because the achievable strain is only in the range of 10^{-3}. The large voltages required to achieve the high driving electric fields (usually in the kV/mm range) are prohibitive in most applications due to the cost of a high-voltage equipment, due to safety considerations and the increased failure rate of piezoelectric devices at high fields. If an ultrasonic device for instance breaks during the examination of a patient, a couple thousand volts at high current and high frequencies would be surely harmful.

As the achievable strain and the required electric fields are material inherent, the only option is to reduce the thickness of the piezoelectric layer and stack many together to still obtain the same actuation. For high-precision devices this is done by hand or by use of robots. Either way is slow and expensive and therefore not suitable for mass-production. Actuators produced by this route are used for many specialized applications e.g. in atomic force microscopy, semiconductor industry etc.

More cost efficient ways to produce high-displacement, low-voltage actuators are required for mass production such as valve control in engines. In order to reduce production steps it is desirable to produce the actuator and the electrodes in one single step. This is done in the co-fired multilayer actuators (figure 1.4a). Electrodes are printed onto tape-cast sheets of the piezoceramic. The layers are then stacked and sintered. An electrode material has to be used that is compatible with the sintering temperatures of about 1300℃. A silver/palladium mixture fulfills this requirement.

Yet, with a layer thickness of less than 100 µm and a total height of several centimeters for the full actuator this design combines low driving voltages, large displacements and low cost. It also incorporates one drawback. Since the layers are very thin, the electrodes can not be contacted by gluing wires to the single layers. Instead the electrodes end inside the material on alternating sides as is schematically shown in figure 1.4b. The electrodes are then simply contacted by applying a conductor to both sides. The consequences of such a design will be discussed later.

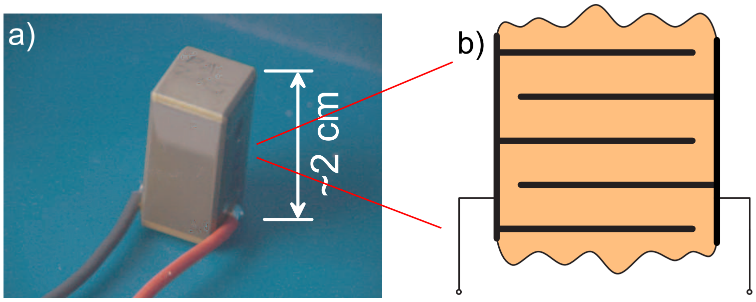

Figure 1.4: a) Photo of a commercial multilayer actuator. b) Schematic representation of the internal electrode configuration.

1.2 Fracture Mechanics

Only a brief introduction into fracture mechanics is given in the first part. A more specialized description of the fracture mechanics of a mixed mode crack in the investigated geometry is provided.

1.2.1 Crack Propagation Behavior

Processes in the neighborhood of the crack tip are of special interest for describing the crack propagation behavior. The stresses acting on the crack tip are influenced by the crack and specimen geometry as well as by the applied external stresses. Three different modes are used to distinguish the deformations of the crack under applied stress:

- Mode I: Tensile stresses normal to the crack surfaces.
- Mode II: Longitudinal shear of the crack surfaces in direction of the crack propagation.
- Mode III: Lateral shear of the crack surfaces perpendicular to the crack propagation direction.

For a given crack in an isotropic elastic and infinite specimen the stresses σ around a crack tip are given by

$$\sigma_{ij} = \frac{K_I}{\sqrt{2\pi r}} f_{ij}(\Theta) \qquad \text{and} \qquad \sigma_{ij} = \frac{K_{II}}{\sqrt{2\pi r}} g_{ij}(\Theta). \tag{1.5}$$

The stresses are singular with the magnitude given by the distance r from the crack tip and the stress intensity factor K. Equations 1.5 are only valid in a neighborhood of the crack tip excluding the crack tip area itself. Far from the crack tip the stresses would decrease to zero which is incorrect as at least the externally applied stresses are present. Very near the crack tip the stresses would be infinite which is also incorrect as no real material would endure such stresses.

The stress intensity factor depends on the externally applied load and the crack and specimen geometry. Equation 1.6 gives a general description with a being the crack length and F_I, F_{II} being the geometry terms available in tabular form [16, 17].

$$K_{Iappl.} = \sigma_{appl.}\sqrt{\pi a}\ F_I \qquad \text{and} \qquad K_{IIappl.} = \tau_{appl.}\sqrt{\pi a}\ F_{II} \tag{1.6}$$

If the stress intensity factor attains a critical material specific value, $K_I \geq K_{IC}$ or $K_{II} \geq K_{IIC}$, the crack will propagate. The critical value is called *fracture toughness*. In case of a mixed loading the stress intensity factor is generally obtained by superposition of the single loads and the crack propagation criterion becomes more complex.

Another approach to crack propagation is an energy criterion. By increasing the crack length, elastic energy stored in the specimen is relieved. At the same time new surfaces are created and thus surface energy has to be provided. This is the approach initially taken by Griffith [18]. Similar to the stress intensity factor approach, crack propagation sets in, if the energy release

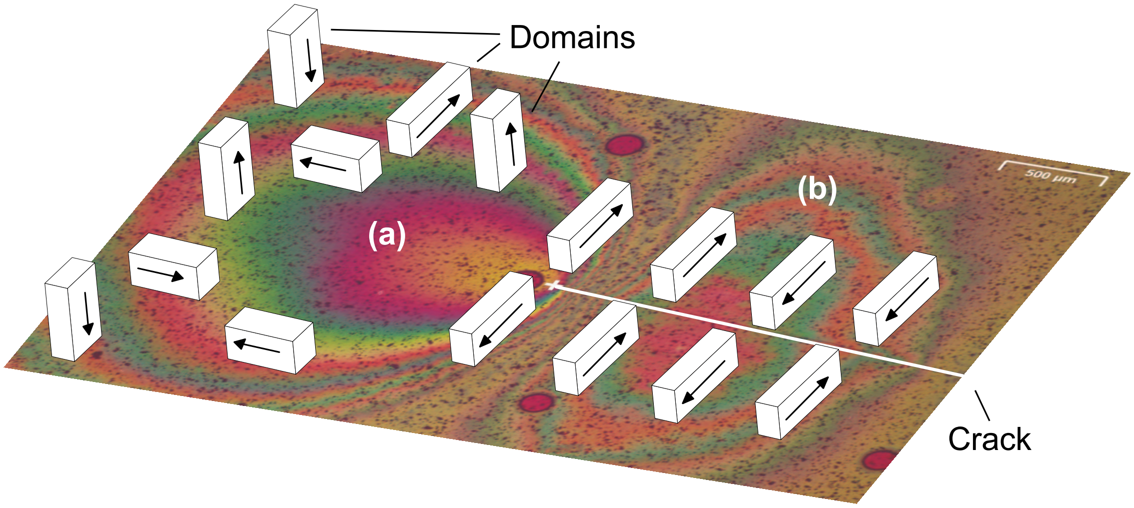

Figure 1.5: Toughening by domain switching in PZT. The domains switch under the influence of the crack tip stress field (a). A zone of compressive stresses develops in the crack wake (b) while the crack grows. The underlaid picture shows the elastic-plastic stress fields in a PZT specimen visualized by a liquid crystal technique [20].

rate $\mathcal{G}$ reaches a critical value $\mathcal{G}_C$. Both approaches can be converted into each other in the elastic case by

$$\mathcal{G} = \frac{K_I^2}{Y'} + \frac{K_{II}^2}{Y'} + \frac{(1+\nu)K_{III}^2}{Y'} \tag{1.7}$$

with the Young's modulus $Y' = Y$ for plane stress and $Y' = Y/(1-v^2)$ for plane strain.

The material part of the thermodynamical equilibrium between crack driving force and crack resistance force $K_{appl.} \geq K_R$ for crack growth can be expressed as $K_R = K_0 + K_\mu$ with K_0 being the crack tip toughness and K_μ a structural shielding term. The latter can be attributed to mechanical bridges between grains for example. Some materials can induce crack closure stresses by a phase transition with a volume increase (e.g. ZrO_2 [19]). In ferroelastic materials a contribution comes from domain processes as symbolized in fig 1.5, electrical fields and in some cases also from phase transitions.

Such dependence of the structural term from the crack length is called *R-curve*. In materials with $K_\mu = 0$ the R-curve is constant at the intrinsic toughness K_0. Window glass is an example for such behavior. Otherwise K_μ depends on the crack length as closure stresses do normally not act on a single point but over a certain area. After a certain distance from the crack tip the crack surfaces cannot interact anymore. The R-curve stays constant from there on at a plateau value K_C. In a poled PZT material the stresses can be visualized by a liquid crystal technique as shown in fig 1.5 [20]. It is clearly visible that the stresses decay at a certain distance behind the crack tip.

It is now of importance to distinguish between stable and unstable crack propagation. Attaining K_R is a necessary condition for crack propagation but it is not possible to determine the further crack propagation. Therefore an additional criterion has to be used.

$$\frac{d\mathcal{G}_{appl}}{da} > \frac{d\mathcal{G}_R}{da}, \frac{dK_{appl}}{da} > \frac{dK_R}{da} \qquad \text{(unstable)} \tag{1.8}$$

$$\frac{d\mathcal{G}_{appl}}{da} < \frac{d\mathcal{G}_R}{da}, \frac{dK_{appl}}{da} < \frac{dK_R}{da} \qquad \text{(stable)} \tag{1.9}$$

Unstable crack growth is characterized by catastrophic failure of the material. Stable crack growth will terminate after a certain length because the crack driving force $\mathcal{G}_{appl}$ will eventually drop beneath the critical value.

So far only the thermodynamics of crack growth was considered. Kinetic effects allows crack growth at stress intensity levels beneath the thermodynamically defined value, a behavior called *subcritical crack growth* [21]. The atomic bonds at the crack tip are weakened by chemical corrosion and thus the stress intensity factor is reduced [22]. Plotting the crack growth velocity over the applied stress intensity factor usually yields three regions [23, 24]. The first region is characterized by a strong dependence of the crack velocity on the stress intensity factor given by the reaction rate of the corrosive species with the crack tip bonds. Only a small dependence is obtained in the second region, controlled by the speed at which the corrosive species reaches the crack tip. The third region is again dominated by the stress intensity factor and is determined by the kinetics of the atomic bonds. This is true for materials, where no other time-dependent deformations may occur.

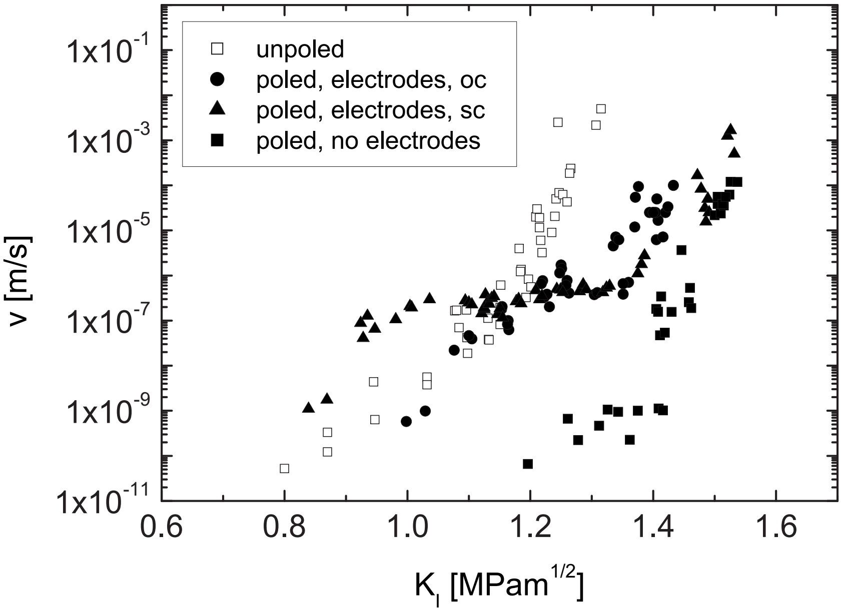

Figure 1.6: v-K-curves of unpoled PZT 151 as compared to specimens poled in thickness direction under various electrode configurations (oc: open circuit, sc: short circuit) measured in the compact-tension geometry for 3 mm thick specimens [25].

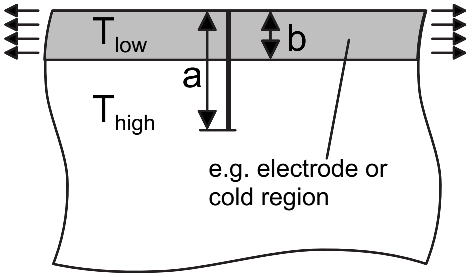

Figure 1.7: Simplified model for discussion of crack deflection.

Ferroelastic toughening is the dominant toughening mechanism in the investigated materials. Therefore the switching velocity of the domains is also an important criterion because fast crack growth should hinder domain switching. As domain switching is strongly dependent on the electric boundary condition, the kinetic effects will also depend thereupon. A qualitative impression of the v-K behavior of the investigated material is shown in figure 1.6.

1.2.2 Crack Deflection[1]

A single crack in a specimen that is subject to a tensile stress along a strip on the edge will grow. An example of such a case is a hot plate dipped in cold water. Some aspects of the different crack propagation regimes will be discussed using some simplifying idealizations: A semi-infinite specimen exhibits a constant stress σ in the top region ① due to strain incompatibility as shown in figure 1.7. Furthermore, the material parameters remain identical for both active ① and inactive ② zones and quasi-static fields. Under these assumptions, the quasi-static squared stress intensity factor can be sketched qualitatively in figure 1.8 for two situations: a straight crack and a primary straight and then deflected crack with total crack length of a. In anticipation of the actual experiments the active zone is termed electrode and the imposed load is an electric field. The similarity to the thermal case of a hot plate dipped in a cold medium will be shown later.

For a constant electric field, i.e. constant σ, in figure 1.8 the squared stress intensity factor K_I^2 increases linearly with crack length a in the electroded zone as an edge crack under constant stress ($K_I^2 = 3.95\ \sigma^2 a$ [17]) and decreases outside of the electroded zone like an edge crack under point force for $a \gg b$ ($K_I^2 = 2.13\ \sigma^2 b^2/a$ [17]). Note that the asymptote for the straight crack is $K_I^2 = 0$ and for the deflected crack $K_I^2 = 0.343\sigma^2 b$ [27]. Larger indices in figure 1.8 stand for increased σ, i.e. higher electric fields.

In the following analysis linear-elastic fracture mechanics for a non-kinked crack is applied:

$$K_I \geq K_{IC}, \qquad K_{II} = 0 \tag{1.10}$$

---

[1] Cooperation with Dr. H.-A. Bahr, Dr. V.-B. Pham and Prof. Balke, Dresden University of Technology [26].

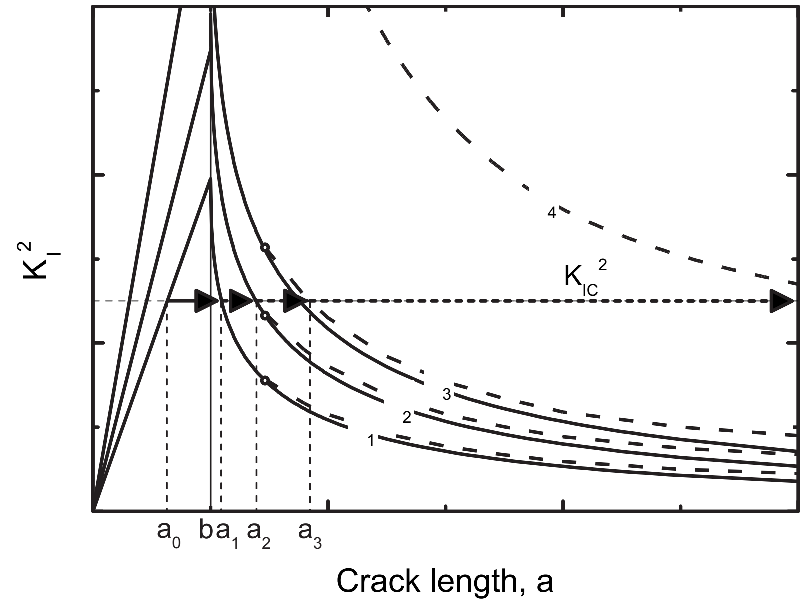

Figure 1.8: Squared mode I stress intensity factor for a crack in a semi-infinite specimen for different σ. The full line denotes the straight crack along the symmetry and the dashed line the primary straight and then deflected crack (full arrow: unstable crack propagation, dashed arrows: stable crack propagation).

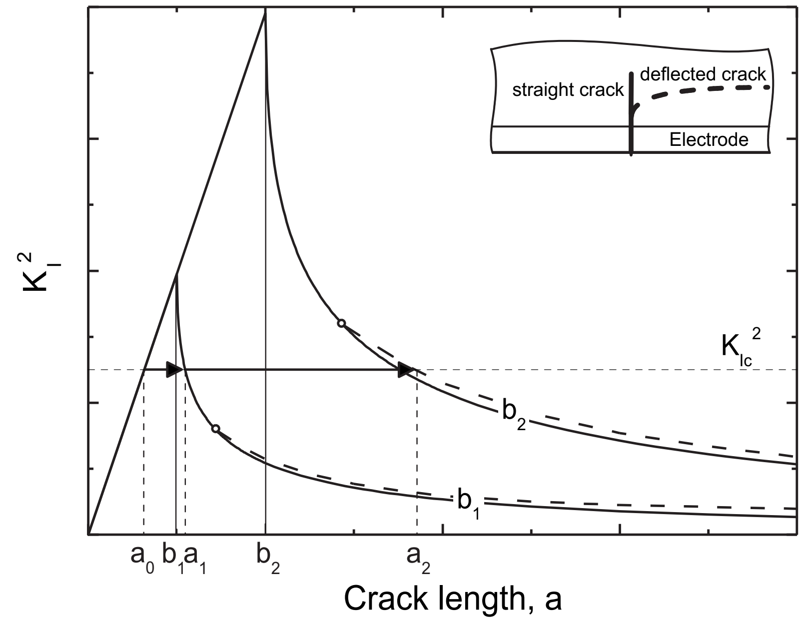

Figure 1.9: Squared mode I stress intensity factor for a crack in a semi-infinite specimen by variation of the width b. The full line denotes the straight crack along the symmetry and the dashed line the primarily straight and then deflected crack (full arrow: unstable crack propagation).

The criterion of local symmetry for a non-kinked crack $K_{II} = 0$ determines the curved crack path [28] and is automatically fulfilled by a straight crack on the symmetry line. Note that the dielectric displacement intensity factor K_{IV} [29] vanishes everywhere over the entire crack because in the electrode zone the electric field is parallel to the crack front due to symmetry arguments and zero in the inactive, unpoled zone.

A set of crack propagation scenarios is used to illustrate the problem with the aid of figure 1.8. An initial crack $a_0 < b$ starts propagating unstably (full arrow) at a given σ_1 satisfying the conditions (1.10). This unstable stage will end at the crack length a_1, where the condition $K_I = K_{IC}$ is met at the downward slope of the K-curve for σ_1. Dynamic effects, which should drive the crack to a length $a > a_1$, are not considered. An increase of stress σ will prompt stable crack propagation under the condition $K_I = K_{IC}$ up to the crack length a_2 at σ_2 (dashed arrow). The crack path remains straight, as long as the bifurcation (open circle) point between straight crack (full line) and deflected crack (dashed line) in figure 1.8 remains below K_{IC}^2. An increase of σ to σ_3 moves this point above K_{IC}^2. Therefore, the crack will deflect, as it can release more energy on the deflected path than on the straight one. It will continue growing stable until the K_I -asymptote reaches K_{IC} at $\sigma_4 = K_{IC}/\sqrt{(0.343b)}$. Then it grows unstable again to an infinite crack length.

The different crack paths depending on the electrode width b are discussed by means of figure 1.9. Note that the bifurcation crack length corresponding to the open circle scales with b as the only characteristic length in this problem where the crack path follows from $K_{II} = 0$. A small electrode width b (b_1 in figure 1.9) favors a straight crack in the first unstable stage. The straight crack cannot turn, as long as the stress field cannot be further increased to reach the branching point. In contrast, a large electrode width b (b_2 in figure 1.9), leads to a bifurcation point above K_{IC}^2 and thereby to crack deflection during the first unstable stage.

This simple model of the quasi-static stress intensity factors provides an understanding of the qualitatively different crack paths (straight and deflected) depending on electrode width and the stable and unstable stages of these paths. It is similar to the model assessing different crack paths in thermal shock cracking [30].

1.3 Fracture Mechanisms of Piezoceramics

1.3.1 Material Behavior

For the scope of this work the material behavior concerning cracking is of primary interest. Other areas of interest in the ferroelectric/ferroelastic material area are aging, fatigue, constitutive behavior and modelling or new single crystal materials with controlled domain structure (so called “domain engineering”). Some recent review articles give a good overview over those areas [2, 31, 32, 33].

From past investigations using short cracks, which were produced using Vickers or Knoop indentations, it is well known that electrically poled piezoelectric ceramics exhibit a strongly anisotropic fracture toughness (e.g. [34, 35]). This is mainly attributed to the different switching ability of domains in the crack tip stress field. Both, poling direction as well as degree of polarization, have to be considered. While most investigations focused on indentation techniques, publications on R - curve behavior in ferroelectric materials are recent developments. Measurements on bend bars with various methods were preformed by Fett et al. [36]. Meschke et al. measured R-curves in the compact tension geometry for $BaTiO_3$ [37] and showed that the R-curve is almost entirely reversible by unloading and depends on grain size. Investigations of the fracture toughness revealed a strong influence of the polarization state [38]. A ranking of the fracture toughness as function of the polarization is given by $K^B > K^X > K^A > K^C$. Here, B is the thickness direction, X is unpoled, A is poled parallel and C is poled normal to the crack growth direction. The presence of electrodes without an electric field during crack growth greatly reduces the fracture toughness [39]. With an applied electric field parallel to the crack front the fracture toughness increases [40]. Summarizing the experimental results it can be stated that the fracture toughness sensitively depends on the applied electrical and mechanical boundary conditions as well as on the load history. All measurements proved a very low fracture toughness between 1 and 2 $\mathrm{MPam}^{\frac{1}{2}}$.

It is agreed that toughening is based on a process zone mechanism similar to transformation toughening [41, 37], with domain reorientation being an additional complicating feature in ferroelastic switching. Besides the toughening mechanisms like crack bridging, branching and deflection, microcracking is also present [42]. Studies in a Lanthanum doped PZT proved that domain switching is actually the dominant toughening mechanism [43]. X-ray diffraction studies confirmed domain-switching not only in the crack wake of stable crack growth, but on a reduced level also during unstable crack growth [44]. With the aid of a newly developed technique using liquid-crystals the elastic-plastic stress fields could be visualized [20]. An extension of the anelastic zone in the sub-millimeter range was measured. This agrees well with X-ray diffraction measurements yielding a process zone height of approx. 600 µm [45]. The switching itself is governed by the Tresca yield condition [46]. In consequence thereof the switching zone will be larger under plane stress conditions than under plane strain conditions with consequences on the toughening behavior and therefore on the R-curve.

A considerable amount of literature concerning the analytical analysis of fracture in piezoelectrics was developed (e.g. [47, 48, 49, 50, 51]). Most of them are limited to pure dielectric, linear piezoelectric or electrostrictive materials and the crack is mostly assumed to be either impermeable ($\varepsilon_r = 0$) or conductive ($\varepsilon_r = \infty$). Especially the first assumption is problematic as at least the vacuum permittivity ($\varepsilon_r = 1$) is present in the crack. For the simple case of a Griffith crack, statements on the influence of an electric field in the plane of the crack propagation can be made. McMeeking [51] showed that it will lower the crack driving force if the permittivity of the crack is lower than the permittivity of the dielectric as the electric field in the piezoelectric corresponds to a lower energy state than the electric field in the crack. Incorporating a realistic assumption on the crack permittivity reduces the influence of the electric field. The energy release rate for a Griffith crack in a linear dielectric becomes

$$\mathcal{G} = \left(\frac{\sigma_\infty^2}{Y'} - \frac{(\varepsilon_d - \varepsilon_c)\frac{\sigma_\infty}{Y'} E_\infty^2}{(\frac{\varepsilon_c}{\varepsilon_d} + \frac{2\sigma_\infty}{Y'})} \right) \pi a, \tag{1.11}$$

where ε_d and ε_c are the permittivities of the dielectric and the crack, σ_∞ and E_∞ the externally applied stress and electric field [51].

It can be seen from equation 1.11 that the crack driving force is increased if the permittivity of the crack is higher than that of the dielectric as it is the case for a conducting crack. Another conclusion from the simple case presented above is that a crack must be opened, i.e. an external stress has to be applied, in order for the electric field to have an effect. That is a manifestation of the fact that a closed crack is “invisible” to the electric field. Including piezoelectricity makes matters more complicated because of the electro-mechanical coupling. An electric field by itself will open the crack and thus provide an energy release rate, which under certain circumstances can be positive and in consequence drive the crack [52]. Application of an electric field superposed on a stress field can both increase and decrease the energy release rate, depending on the polarization, the permittivity of the crack and the fields themselves. Yet, an electric field applied parallel to the crack surface (thickness direction in a CT-specimen) has no effect on the crack driving force, regardless of the assumptions on the crack, but it will have an effect on the crack resistance if domain switching is included [40].

An expression of the toughening behavior due to domain switching was obtained analytically, ranking the achievable toughening as function of the polarization in the order $K^B > K^A > K^X > K^C$ [53, 54, 55]. This order agrees very well with the experimental findings in [38], regarding the fact that no mechanical clamping in A-direction is introduced in the analytical model. The model consists of two steps. In the first step the geometry of the switching zone is assessed by introducing the effective electric and stress fields in equation 1.4. The second part uses the geometry and the achievable strain by switching and calculates the toughening in the sense of transformation toughening [19]. By such an approach it is possible to introduce the effect of an externally applied electric field on the toughening by domain switching [53]. Depending on the permittivity of the crack and the sign of the applied electric field the fracture toughness can be increased but also significantly decreased by an electric field.

Common to all analytical investigations, regarding the crack driving or crack resistance force is that the boundary conditions significantly influence the cracking behavior. It is therefore very difficult to achieve theoretical results for a problem incorporating highly inhomogeneous boundary conditions as it is the case around the electrode edge of a multilayer actuator.

1.3.2 Damage in Multilayer Actuators

In cofired multilayer actuators as shown in figure 1.4 the electrodes end inside the material. In first approximation the actuator can be divided into the middle and outer parts. In the middle, electrodes of both polarities (i.e. electric potentials) are present while only electrodes from one side are located in the outer parts. As in the outer part the electrodes have all the same potential, no electric field is present and no actuation is obtained. In the middle, the electrodes have alternating potential and therefore an electric field exists which will lead to an actuation of the material. The result is a strain incompatibility between the middle and outer part and high stresses arise. A similar case is given by a hot plate that is cooled in the middle giving rise to a thermal strain mismatch. In reality matters are more complicated as the electric field at the electrode edges is inhomogeneous.

Studies of the damage mechanisms in ceramic multilayer actuators made of piezoelectric materials have revealed that cracks are actually formed preferentially at the internal electrode edge [56, 57]. Takahashi et. al. [58] calculated the stress distribution around the electrode edge by means of a linear finite - element method and showed that the magnitude of the tensile stresses is comparable to the strength of the ceramic. Further investigations on model and real actuators under cycling bipolar and unipolar electric fields showed that cracks are formed during the first few cycles [59, 60]. This leads to the assumption that the cracks might be initiated during the very first poling and grow during subsequent loading.

An analytical approach to the problem of cracking was presented by Suo [61]. He studied different conducting paths and described the basic cracking mechanism as a localized switching zone around the end of a conducting sheet (like an electrode). He demonstrated that the electric field at the tip of a conducting layer is inhomogeneous and much higher in magnitude than the nominally applied electric field. For a linear dielectric as an unpoled ferroelectric ceramic the magnitude of the electric field around the tip of a conducting sheet is

$$E = \frac{K_E}{\sqrt{2\pi r}}. \tag{1.12}$$

As in the similar case of the mechanical stress intensity factor this solution is only valid in a certain environment of the tip. Those electric fields give rise to an incompatible deformation due to the piezoelectric effect and to ferroelectric-ferroelastic switching. With $E = E_C$ the radius of the switching zone can be estimated to

$$r_{switch} = \left(\frac{K_E}{E_C}\right)^2 \frac{1}{2\pi}. \tag{1.13}$$

This approach was refined with non - linear finite element modelling for electrostrictive ceramics [62] calculating stress distributions and stress intensity factors for a multilayer actuator model. Hao et al. attained an analytic expression of the lower layer thickness limit t_c below which no cracking occurs [63]:

$$t_c = \left(\frac{K_{IC} E_S}{\Lambda \Omega Y S^S E_{appl.}}\right)^2. \tag{1.14}$$

This expression is based on the small-scale saturation assumption in which $r_{switch} \ll t, b$. In the above equation (1.14), Ω is a geometry term and Λ a material dependent term. It was further developed to lift the restrictions imposed by the small-scale saturation assumption by Gong et al. [64]. They investigated the effect of different flaw sizes and load levels and calculated a limit for the layer thickness. Assuming a multilayer actuator like the one shown in figure 1.4 the above terms become $\Omega = \sqrt{2}$ and $\Lambda = 0.25$.

The theoretical study of the fracture toughness as function of the applied electric field around voids showed that the singular electric fields around a crack lead to a reduced fracture toughness of the material [53] in contradiction to the uniform field between the electrodes. The electrode edge is also a source of a singular electric field and thus the above result still holds if a void is located just at the tip of the electrode. In all the above studies, cracking is always the result of a strain incompatibility inside the device. Electric breakdown also leads to failure, but only at much higher electric fields. So far, no experimental work is available concerning the crack nucleation.

1.4 Behavior of Cracks under Strain Incompatibility

1.4.1 Thermally Induced Strain Incompatibility

The most natural cause for cracking induced by a strain incompatibility is the thermal case in which e.g. a hot plate is only partially cooled. Early experiments including fracture mechanical methods were performed by Hasselmann [65]. Nemat-Nasser et al. theoretically investigated the problem of multiple edge crack growth and conducted experiments on precracked glass plates [66, 67]. A more recent and detailed experimental work and analysis on quenched hot glass ceramic bars was provided by Bahr et al. [30, 68].

Depending on the temperature difference between the glass and the water different crack patterns develop. Large temperature differences lead to the formation of many small cracks with an alternating sequence of larger and smaller cracks while small thermal differences yield few large deflected cracks.

The crack driving force is given by the stresses induced by the thermal strain mismatch between hot and cold parts of the bar. As the bar remains in the cold medium, the temperature will penetrate further inside the material and the zone of strain mismatch, and thus stress, is increased. For an ideally cooled surface of a bar with the thermal diffusivity κ, the temperature distribution $T(x,t)$ as function of time t is given by

$$\begin{aligned} T(x,t) &= T_{bar} - \Delta T \cdot \mathrm{erfc}(x/2\sqrt{\kappa t}) \\ \mathrm{erfc}(u) &= 1 - \tfrac{2}{\pi} \textstyle\int_o^u \exp(-\zeta^2)\mathrm{d}\zeta . \end{aligned} \tag{1.15}$$

The stress distribution is easily obtained by $\sigma(x,t) = -Y\alpha(T(x,t) - T_{bar})$ with x pointing from the cold surface into the interior. Now, the stress intensity factor can be calculated by the weight function method for an arbitrary flaw of the length a on the surface:

$$K_I(a,t) = \int_0^a M(a,x) \cdot \sigma(x,t)\mathrm{d}x . \tag{1.16}$$

The weight function $M(a,x)$ weights the applied stress according to the distance form the crack tip. For the given geometry of an infinite bar it is [68]:

$$M(a,x) = \frac{1}{\sqrt{a-x}}\left(1 + 0.6147\frac{a-x}{a} + 0.2502\left(\frac{a-x}{a}\right)^2\right). \tag{1.17}$$

Eventually, the fracture toughness of the material for a flaw located at the edge will be reached, a crack initiates at the flaw and is driven by the penetrating temperature field. The time dependent penetration depth is given by $\delta(t) = 2\sqrt{\kappa t}$. As the tensile stresses are present only in the front region of the bar, the stress intensity factor will increase in the front region, reach a maximum and then decrease as the stress decreases. This is very similar to the case of a stressed strip in an otherwise unloaded specimen introduced in section 1.2.2. The major difference is that the transition zone between loaded and unloaded zone is not sharp and that the width of the stressed zone increases with time. Figure 1.10 shows the stress intensity factor as function of the crack length for various times. Note that the fracture toughness is lower for a high ΔT because of the normalization.

Two scenarios can be discussed by means of the above model. If the temperature difference between the bar and the coolant is large, the stress intensity factor peaks for small flaws. As many flaws are located at the surface multiple cracks will emerge. Yet, every crack unloads the surrounding material in a neighborhood approximately equal to the length of the crack and a

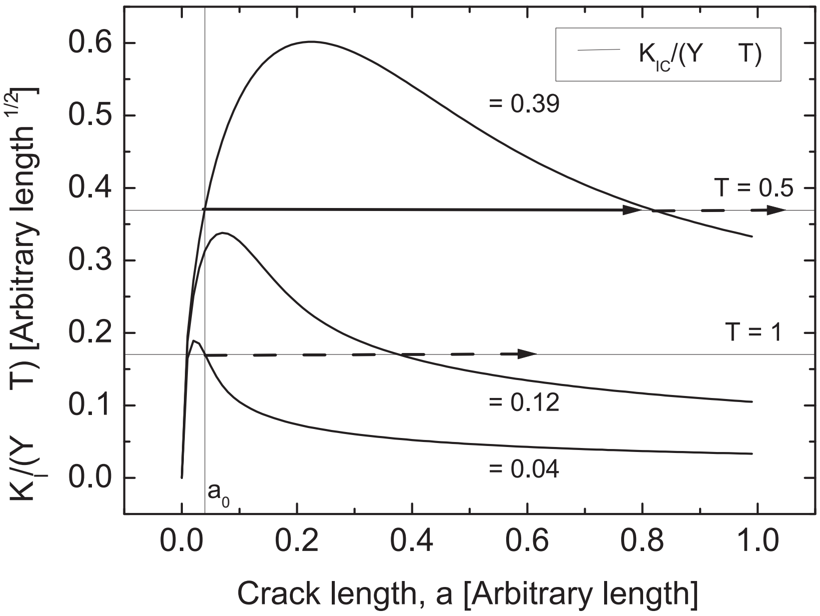

Figure 1.10: Normalized stress intensity factor as function of the crack length for a single crack in a half space ideally cooled on the surface. The penetration depth of cooling is varied. Stable crack growth is symbolized by dashed arrows and unstable crack growth by solid arrows.

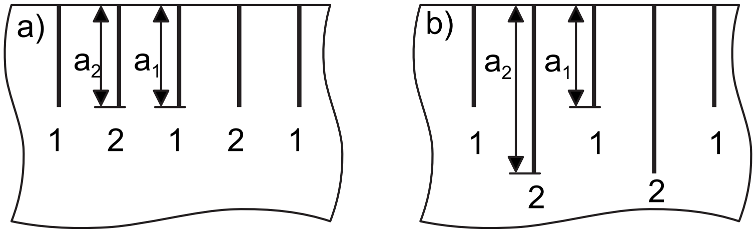

Figure 1.11: Schematic model of two sets of cracks (labelled 1 and 2) growing from one edge.

more or less regular pattern of cracks is observed. As the flaws, which are activated first, are small, many can grow because the corresponding unloading zone is also small. In the course of time the cracks grow and therefore the unloading zone of every crack increases and some cracks are left behind. An alternating pattern of long and short cracks develops.

For a fracture mechanical treatment of this scenario, consider the case of two sets of cracks labelled 1 and 2 with lengths a_1 and a_2 growing parallel from one edge as shown in figure 1.11. Under stable conditions they have the same length (figure 1.11a) and grow under the condition $K_1 = K_2 = K_C$ (the index I is omitted for simplicity). The fracture criterion at equilibrium is given by [30]:

$$\mathrm{d}K_1 = \frac{\partial K_1}{\partial a_1}\mathrm{d}a_1 + \frac{\partial K_1}{\partial a_2}\mathrm{d}a_2 + \frac{\partial K_1}{\partial \delta}\mathrm{d}\delta = 0 = \frac{\partial K_2}{\partial a_1}\mathrm{d}a_1 + \frac{\partial K_2}{\partial a_2}\mathrm{d}a_2 + \frac{\partial K_2}{\partial \delta}\mathrm{d}\delta = \mathrm{d}K_2. \qquad (1.18)$$

If one set (e.g. 1) is stopped for a moment ($\mathrm{d}a_1 = 0$, figure 1.11b), K_1 will get beyond K_C in the next load increment. At the same time the cracks 1 are unloaded by the larger cracks 2. The bifurcation point at which the cracks 1 cannot catch up anymore can be written as

$$\frac{\partial K_1}{\partial a_2} = \frac{\partial K_2}{\partial a_2} \qquad \text{with} \qquad \frac{\partial K_1}{\partial \delta} \approx \frac{\partial K_2}{\partial \delta}. \qquad (1.19)$$

As long as the left hand side of eqn. 1.19 is larger than the right hand side, the cracks will catch up. The actual relationship between the distance of the cracks and their lengths is included implicitly in the stress intensity factors K_1 and K_2 and can be calculated numerically.

In the second scenario ΔT is small and therefore the largest flaws will be activated first, because K_I now peaks for larger a. With increasing time the penetrating stress field will drive the few cracks to significant lengths. As only few cracks are present little interaction is observed. With increasing lengths the cracks will eventually attain a critical length for deflection. A similar result is obtained if a controlled starter crack is introduced before quenching the bar. The fracture mechanical description of this case is already given in section 1.2.2.

The drawback of the thermal shock experiments from the modelling standpoint is that the driving force cannot be stopped in the experiment, neither can it be measured for every step of crack extension.

1.4.2 Electrically Induced Strain Incompatibility

In ferroelectric/ferroelastic ceramics the driving force, the electric field, can be precisely measured and controlled allowing more accurate and precise model experiments. Unpoled ceramics are isotropic and therefore an analogy to the thermal shock case which bears a certain similarity to the strain incompatibility found in the multilayer actuator geometry.

To investigate crack nucleation and crack growth experimentally a simple model incorporating a similar strain incompatibility as in the multilayer actuators is used for all experiments. For the crack initiation experiments small rectangular specimens with centered electrodes are used as shown in figure 1.12. If an electric field is applied between the two electrodes the material will shrink in the directions perpendicular to the field and expand in the direction of the applied electric field. As the adjacent material is not affected by the electric field it will mechanically clamp the active strip. A strain mismatch is induced and high stresses arise leading to crack initiation and growth.

The specimens for the crack initiation experiments should primarily lead to massive crack initiation. The centered electrodes are preferred, because four electrode edges are available for investigation and also for symmetry reasons. As in a ceramic crack nucleation is a statistical process, many specimens with a wide variation of geometries should be investigated. Small plates of 10×10 mm^2 with different thicknesses t and electrode widths $2b$ were chosen. The specimen geometry is shown in figure 1.13a. Due to the symmetric position of the electrode this geometry is termed symmetric configuration.

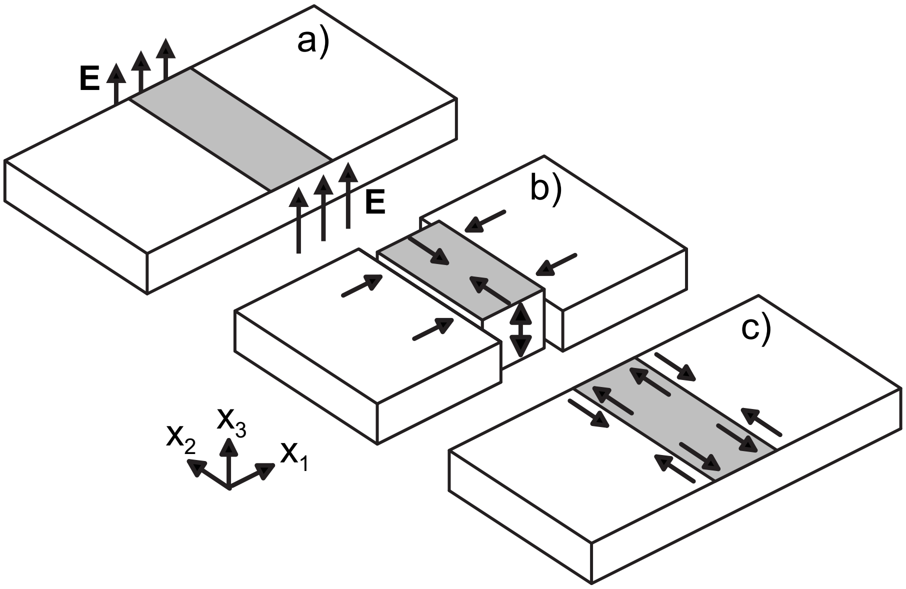

Figure 1.12: Stress generation by mechanical clamping due to partial electrode coverage. a) The Electric field is applied on the centered electrodes (active material). b) Shrinkage in x_1 and x_2 directions and expansion in x_3 direction of the active part ensues. c) Adjacent material mechanically clamps the active strip and high stresses arise.

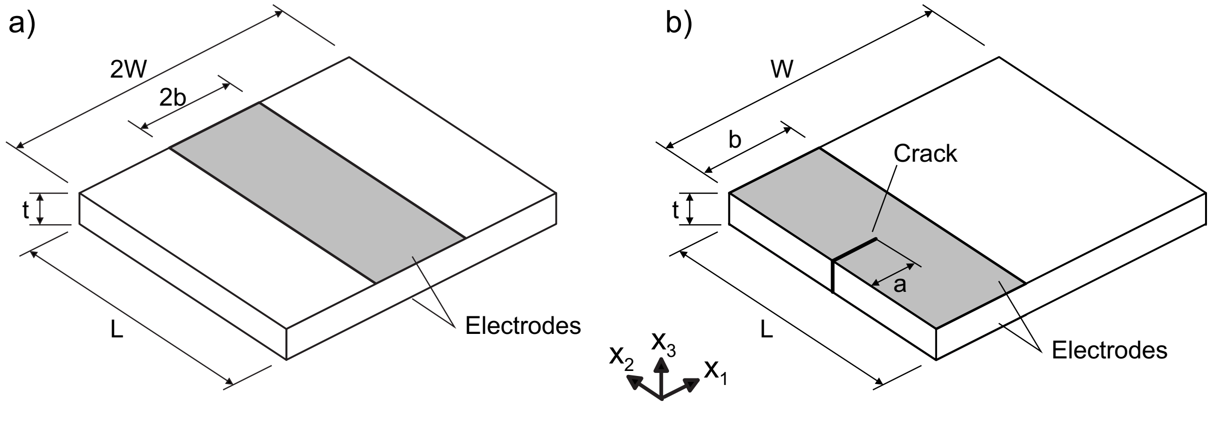

Figure 1.13: Geometries for the a) crack initiation and b) crack propagation experiments.

More considerations went into the choice for the geometry for the crack propagation experiments. The fracture mechanical modelling imposed many of the requirements. The crack had to go through the entire thickness of the specimen and have a simple crack front. Furthermore, electrical fringing fields and the electric field singularity should be as small as possible leading to thin specimens ($b \gg t$). As crack growth is to be studied, a controlled starter crack should be introduced into the specimen and so the electrode was placed at the specimen edge. The stress in the electrode area introduced by the incompatible strains should be maximized which is achieved by choosing long specimens compared to the electrode width ($L \gg b$). By this choice stress relieve due to bending of the outer edges are confined to a comparably small area far away from the crack (see also figure 4.5). Finally, the clamping and the stresses should be as homogeneous as possible and so the electrodes should be narrow compared to the specimen length ($W \gg b$). A compromise of those requirements and the needs to ensure safe specimen handling led to plates of 40×40 mm^2 size and a thickness of 0.5 mm with a variation of the polarization state and the electrode coverage as seen in fig 1.13b. This configuration is called asymmetric as the electrode is not centered.

As mentioned above, the electrical field is used in combination with the ferroelectric and piezoelectric behavior of the material to induce a strain incompatibility. The similarities to the thermal strain experiments are evident. The penetration depth of cooling $\delta(t)$ is equivalent to the electrode width b and the temperature difference ΔT is equivalent to the applied electric field E.

A coordinate system is used in both geometries as follows. Direction x_3 is the electrical field direction, x_2 is parallel to the electrode edge and x_1 is perpendicular thereto forming a right hand coordinate system. The electrode coverage is defined by b/W, were b ($2b$) is the electrode width and W ($2W$) the specimen width in the asymmetric (symmetric) geometry. The volume between the electrodes will be defined as active material and the remainder as inactive material.

Chapter 2

Crack Initiation

In the first part the influence of geometrical constraints on crack nucleation is investigated. The geometrical constraint is given by a variation of electrode coverage and specimen thickness. Local effects of the electrode edges leading to cracking are analyzed as well as global effects characterized by the achievable strain. The coercive field is evaluated as a measure of the actual constraint. Non-linear finite element modelling is used to understand the internal processes.

2.1 Experimental Methods

2.1.1 Specimen Preparation

All crack initiation experiments were performed on the batch S3. The specimens were delivered as plates of dimensions 40×40 mm^2 with thicknesses of 1 mm and 2 mm. They were polished on one side to a 1 µm finish with a special polishing procedure for this material developed previously [15]. Some of the 1 mm thick plates were ground down to 0.5 mm after polishing. Finally the plates were cut to specimens of approx. 10×10 mm^2.

Electrodes of approx. 50 nm thickness consisting of gold / palladium (80% / 20%) were sputtered onto the polished specimens (Sputter Coater SCD 050, Balzers) using a plasma current of 40 mA for 200 s. To achieve only partial coverage stencils of overhead transparencies were cut with a carpet knife and attached to both surfaces by superglue (Sekundenkleber Blitzschnell, Uhu) and removed after sputtering. The stencils were drawn with a design software program (Designer 8.0, Micrografx) and had 0.5 mm rulers on both sides of the slit (figure 2.1b) to facilitate the centering on the specimen. A narrow strip of silver - paint (Leitsilber 200, Hans Wolbring GmbH) was applied along the center of each electrode to ensure complete contact along the electrode length in all stages of cracking. With a very fine brush a line width of about 0.7 mm could be attained. Thin copper wires were glued to the electrodes using a conducting 2 - component epoxy (CircuitWorks CW2400, Chemtronics). Figure 2.1a displays the final configuration. 18 different geometries were prepared, thicknesses of 0.5 mm, 1 mm and 2 mm,

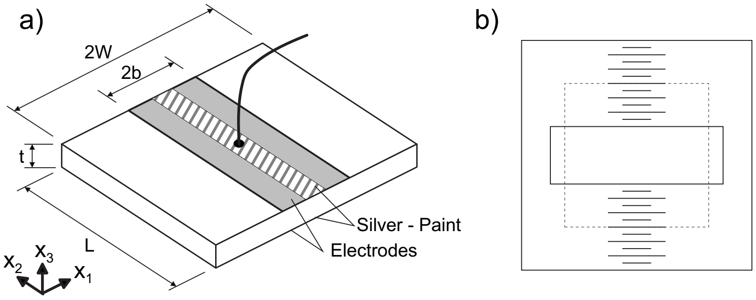

Figure 2.1: a) Schematic overview of the symmetric geometry with attached electrical contact. b) Stencil used for application of the electrode. The specimen position is marked as dashed line.

each with electrode widths of 1 mm, 2 mm, 4 mm, 6 mm, 8 mm and fully covered. At least 3 specimens of each geometry were prepared and measured.

2.1.2 Strain and Coercive Field Measurement

In order to obtain a global material response to the mechanical constraint the global strain was measured and the coercive field was determined therefrom. The displacements were measured parallel (x_2) and perpendicular (x_1) to the electrode edge in the electrode plane. Displacements in the field direction were not characterized. Three identical linear variable displacement transducers (LVDT, W1T3, HBM) with alumina tips were used. The displacements in x_2 - direction were measured differentially as shown in figure 2.2. Special care was taken to ensure that the tips of the LVDTs and the ground fixture were centered on the small specimen faces. Silicone oil with a molecular weight of 1000 (AK 1000, Wacker) was applied to the electrodes with a pipette for electrical insulation.

The LVDT - data was processed by an a.c. measuring bridge (AB12, MC55, AP01, HBM). Two custom built amplifiers were used to amplify the analogue output of the bridge by a factor of 20. A computer with an AD/DA-card (KPCI3102, Keithley) and a custom designed software (see appendix B.1) was used to record the displacement values and to control the unipolar high-voltage source (HCN 35-35000, FUG). The half electric field loop from 0 kV/mm to 2 kV/mm and back to 0 kV/mm was applied at a constant rate of 25 V/(mm·s) for the hysteresis measurement. The data were logged with a rate of 50 points per second and smoothed over 50 data points.

The displacements in x_2 direction were normalized by the length L of the specimen yielding the total strain. In x_1 the width of the electrode $2b$ was used as reference. The strain hysteresis curves were used to determine the coercive field present when the specimen was first poled. The coercive field was taken as the inflection point in the displacement - electric field curve.

To obtain accurate values for the coercive field, the inflexion point had to be well determined. A simple fit to the data points with the inflexion determined from that curve were not sufficient to differentiate between the different clamping conditions, but the experimental accuracy and

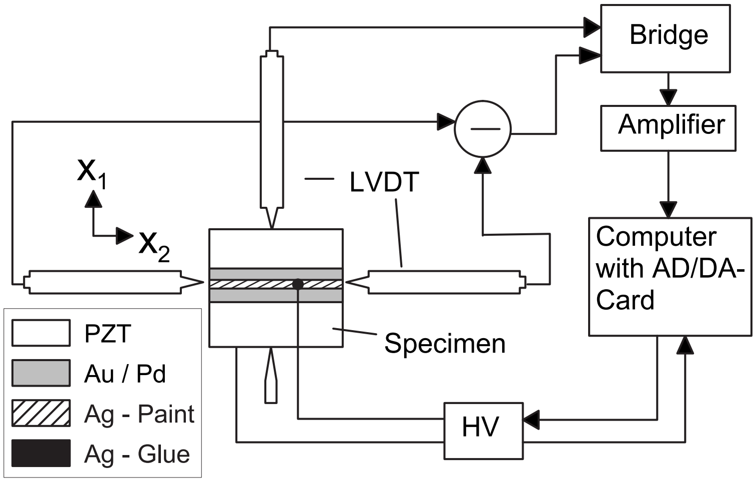

Figure 2.2: Experimental set-up to measure the displacement hysteresis loop.

precision were sufficient for further analysis. The procedure was the following: The experimental data points were taken at constant time intervals. The electric field was linearly increased, which then corresponded to equidistant field increments modified only due to the digitization scatter. The field value for the largest corresponding strain increment marked the first value adopted for E_C. The second one was taken from the largest geometrical distance between two points of a normalized plot also accounting for the digital scatter in field. The third one used the largest slope of the tangent between two adjacent points in a normalized plot. All three maxima were smoothed using a top-hat-algorithm (commonly used in spectroscopy [69]) and the average of these three values yielded E_C given in the plots. The coercive field was discarded if the three E_C values differed by more than 0.02 kV/mm. The data smoothing was done with a programmed data sheet in Microsoft Excel. The error bars represent the maximum and minimum values for each value.

2.1.3 Mapping of the Crack Pattern

After the electric field was applied to the specimens, the crack - patterns were mapped in an optical microscope (DM RME, Leica) at a magnification of 200×. First, the silver - paint was carefully washed off using acetone. Then, the specimens were placed on the computerized coordinate desk (Leica) attached to the microscope. The crack tips were targeted with the crosshairs in the eye pieces and the coordinates were transferred to a custom designed CAD - type software (see appendix B.3). In case of long cracks additional points in the crack path were also included. By this, an up-to scale map of the cracks on the specimen surface was obtained.

As the crack opening is much less than 1 µm for cracks smaller than 500 µm in length, most of them cannot be observed directly even at 200× magnification. An indirect observation method is used instead. The incident light of the microscope is focused on a spot a little aside of the crack. Light scattered on the surface forms a characteristic pattern around the crack by which the crack as well as the crack tip can be clearly localized.

To acquire the actual geometry the four corners of the specimens and the electrode were also mapped. The length and the width of the specimen and the electrode across the center was calculated from the edge coordinates.

2.1.4 Evolution of the Crack Pattern

An in-situ study of the evolution of the crack patterns was done to investigate the processes that lead to formation of different crack types. Only two geometries were chosen for this study. Both of them had a thickness of approx. 2 mm. The first geometry with an electrode width of 1 mm was chosen because this geometry leads to the formation of two crack types (see section 2.2.3). As a reference with only one crack type a geometry with an electrode width of 4 mm was used. The preparation procedure was the same as before except that the copper wires were not mounted on the center of the electrodes but on the side.

The observation of the crack pattern evolution was done in an optical microscope at 200× magnification. A small plastic box mounted on the computerized coordinate desk of the microscope was used for specimen fixture. The box was filled with Flourinert 77 (3M) for electrical insulation. The unipolar high-voltage source was connected to the specimen and the electrical field was manually increased in small steps of about 0.2 kV/mm up to a maximum field of 3.5 kV/mm. At each step the length of the first crack on each electrode edge was measured from the electrode edge using the coordinates provided by the computerized coordinate desk. No additional software was used in this step.

2.2 Experimental Results

2.2.1 Strain

An overview of the dependence of the strain hysteresis in the x_2 - direction on geometry is shown in figure 2.3. In the first set of measurements (figure 2.3a) the electrode coverage was varied while the thickness was kept constant at $t = 2$ mm. A fully covered specimen attained a remnant strain of -1.26×10^{-3} and a strain of -1.93×10^{-3} of highest magnitude (absolute value) at 2 kV/mm. By reducing the electrode coverage the strain magnitude became smaller. At about 10% coverage the remnant and the strain at maximum field of -0.38×10^{-3} and of -0.62×10^{-3} were reduced in magnitude. The coercive field increases slightly from 0.90 kV/mm to 0.93 kV/mm. In the second part of figure 2.3 the coverage was fixed at about 40% and the thickness varied. Now, the remnant and the strain at maximum field stayed basically constant at -1.05×10^{-3} and -1.60×10^{-3}, respectively. The coercive field underwent a major shift from 0.91 kV/mm for a thickness of 2 mm to 1.01 kV/mm for $t = 0.5$ mm. The solid lines in figures 2.3a and 2.3b represent the identical measurement.

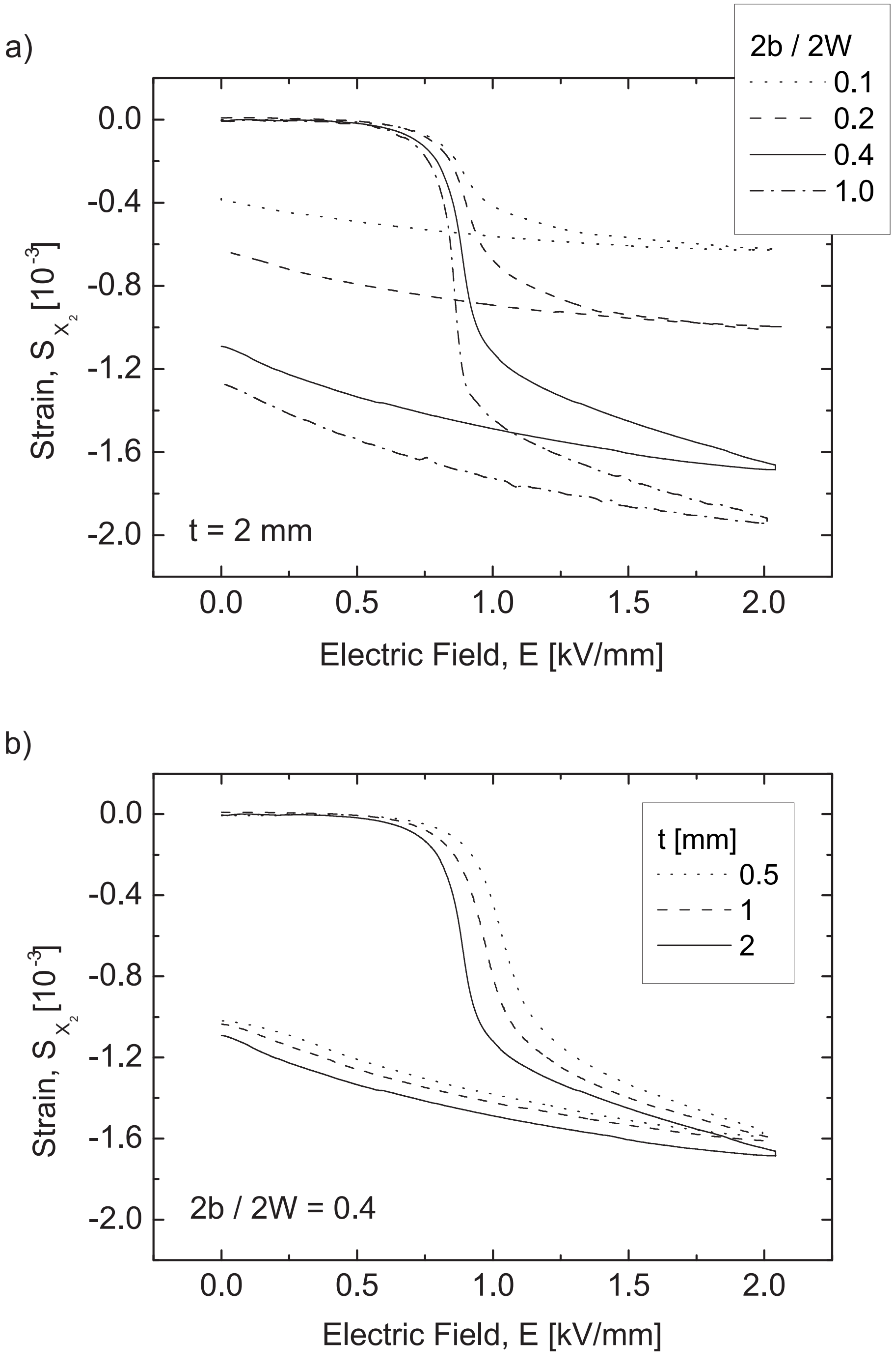

Figure 2.3: Development of the strain hysteresis parallel to the electrode edge (x_2) for different geometries. a) Variation of the electrode coverage for constant thickness. b) Variation of the thickness for a constant electrode width. The hysteresis shown as a full line is the same in both plots.

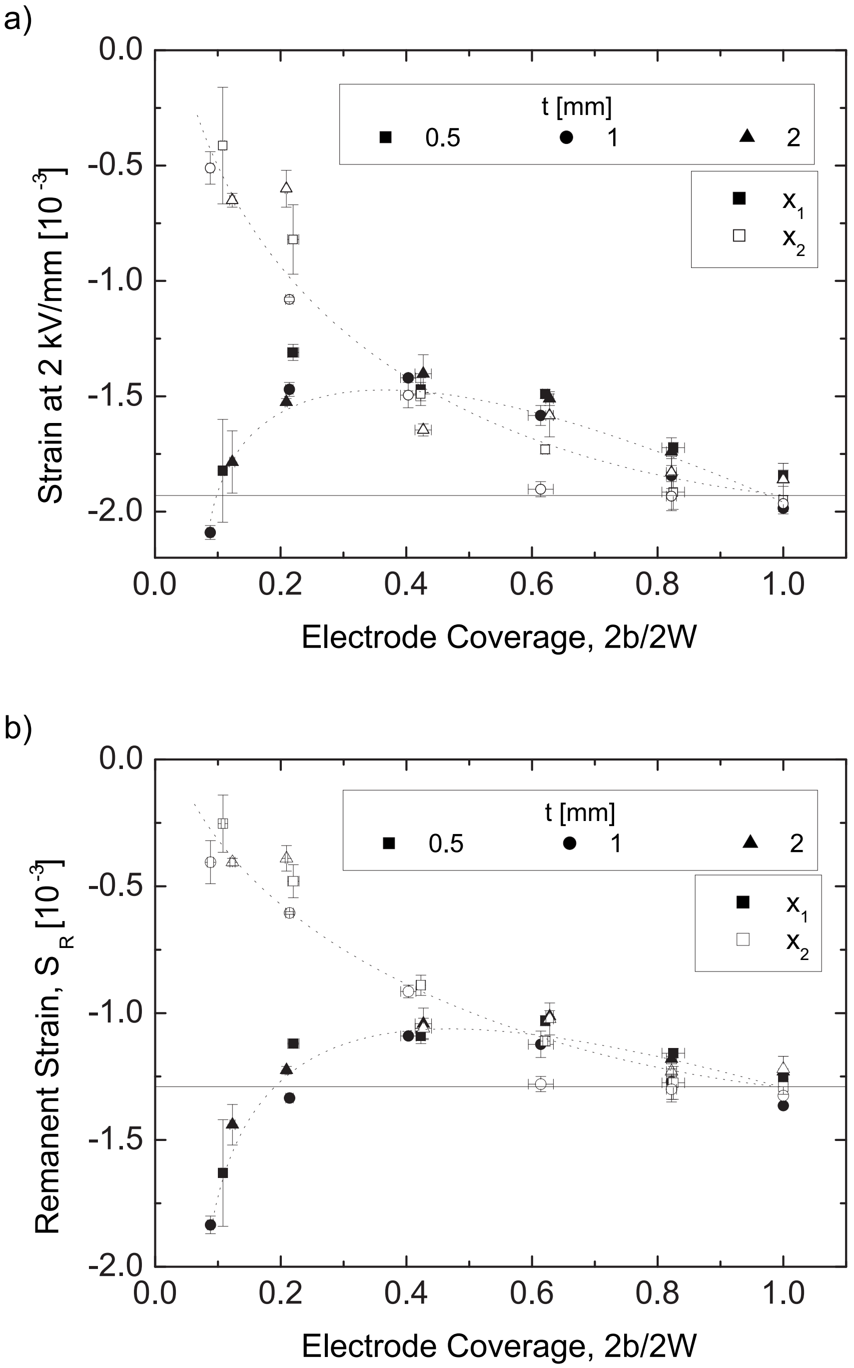

Figure 2.4: a) Strain at the maximum field of 2 kV/mm and b) remnant strain for the x_1 (solid symbols) and x_2 (open symbols) - direction. The thin line represents the strain for a fully covered specimen. The dashed lines are guidelines for the eye and do not represent a fit to the data.

Figure 2.4 presents the strain data at the maximum electric field of 2 kV/mm (figure 2.4a) in both directions and the remnant strains (figure 2.5b) for all of the 18 analyzed geometries. As stated above the sample thickness has only minor influence on the achievable strain. The strain in x_2 - direction is smallest for the lowest electrode coverage (about -0.5×10^{-3} at 2 kV/mm and -0.6×10^{-3} for the remnant strain). By increasing the electrode width the strain increases until it reaches the value of the free specimen (about -1.9×10^{-3} and -1.3×10^{-3}, respectively) indicated by the solid line. For strains in the x_1 - direction the same is true for coverages larger than 40%. For very low coverages the apparent strains exceed the value for the free specimen because of electrical fringing fields at the electrode edges (see discussion). The dependence of the strain on the electrode coverage follows the same pattern at 2 kV/mm and after unloading (remnant strain). The remnant strains are about 68% of the corresponding strains at 2 kV/mm. This factor is the same for all geometries and for both directions except for the x_1 - direction with electrode coverages less than 40%. In these cases the fringing fields lead to a non-linear scaling.

2.2.2 Coercive Field

The apparent coercive fields are shown in figure 2.5 for all geometries. A strong dependence on the thickness is apparent. In specimens with a thickness of 2 mm only a very small influence of the coverage is observed (from 0.90 kV/mm for a fully covered specimen to 0.93 kV/mm for 10% coverage). 1 mm thick specimens exhibit a significant dependence of electrode coverage on the apparent coercive field. The coercive field decreases linearly from 1.00 kV/mm to 0.91 kV/mm with an increase in electrode coverage. Both specimen types, thickness of 1 mm and 2 mm, have the same coercive field of about 0.90 kV/mm for the fully covered case. Specimens with a thickness of 0.5 mm exhibit an apparent coercive field of about 1.02 kV/mm regardless of electrode coverage.

2.2.3 Crack Patterns

Two types of cracks have to be distinguished, short and long cracks. Figure 2.6 displays the resulting crack patterns for the partially electroded specimens, representative for each geometry. For wide electrodes only short cracks are formed at the electrode edges. The narrower electrodes generate long cracks that extend from one side to the other and divide the electrode into two and more fractions. Long cracks appear in electrodes with a coverage of 10% and are sometimes found in electrodes of up to 20% coverage. By viewing the crack pattern for rising electric fields in-situ it was shown that they are formed from two small cracks joining (see section 2.2.4).

The number of short cracks formed depends on the specimen thickness, whereas the lengths of the starter cracks depend on the electrode coverage. Numerous cracks are found in the 2 mm thick specimens and only few in the 0.5 mm specimens. The amount of cracks in the 1 mm and 2 mm thick specimens is comparable. The lengths of the longest short cracks range between approx. 0.6 mm - 0.9 mm in the wide electrodes to approx. 0.2 mm - 0.4 mm in the narrow

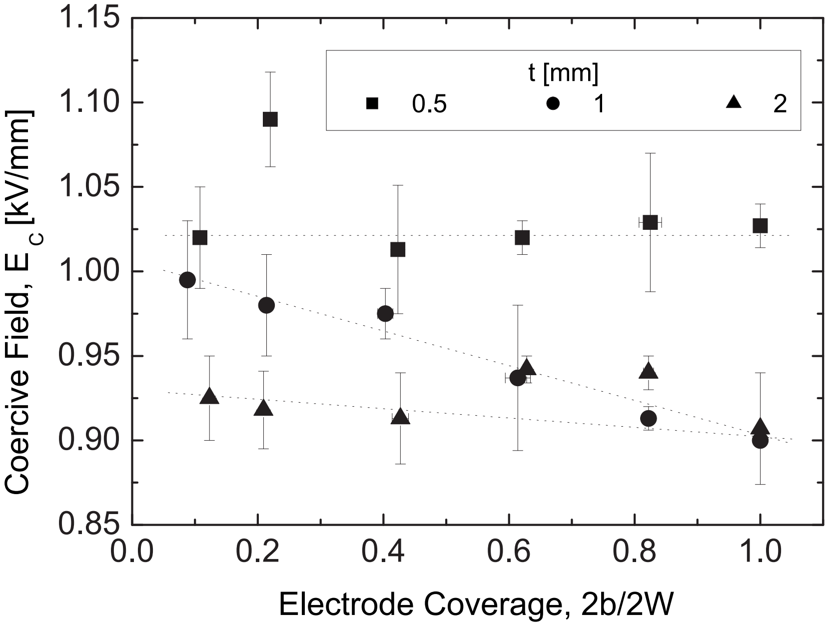

Figure 2.5: Coercive fields as determined from the strain hysteresis. The dashed lines are guidelines for the eye and do not represent a fit to the data.

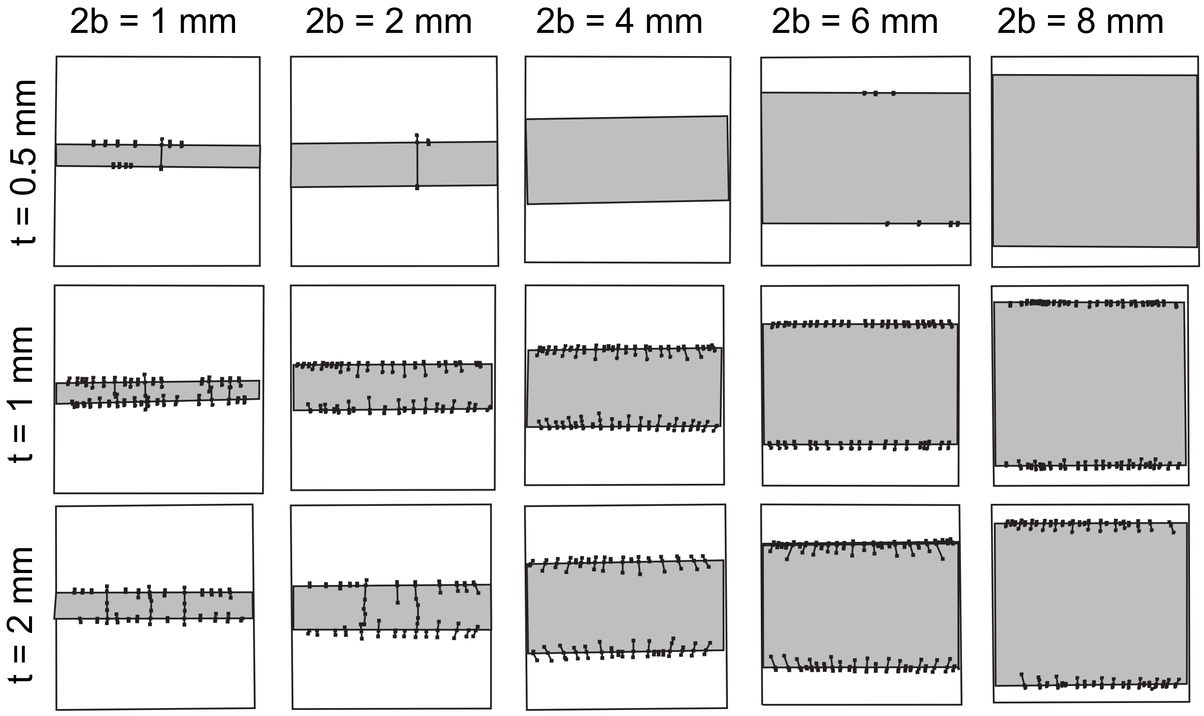

Figure 2.6: The crack patterns for partially covered specimens. The true crack, sample, and electrode geometries are shown. The specimens are sized approx. 10 × 10 mm^2.

electrodes. Variations of the crack lengths could not be correlated to the specimen thickness, except that in thick specimens the cracks tend to form an alternating sequence of long and short cracks whereas they are all of the same length in thinner specimens. As it will be shown later, small cracks in the neighborhood of larger cracks are closed due to stress relief even under applied load. Yet, these maps were obtained after unloading and therefore not all cracks are visible, not even by the indirect observation method.

In specimens with electrode widths larger than 4 mm the cracks did not all grow perpendicular to the electrode edge as expected. An almost radial crack growth with respect to the specimen center was observed (figure 2.6, middle to right columns). Only cracks at the center of the electrode edge were precisely perpendicular to the edge. This effect was not seen for 1 mm wide electrodes and only to a smaller extent for 2 mm wide electrodes. The crack growth direction did not depend on the specimen thickness and was only determined by the electrode coverage. It will be shown by FEM calculations that shear stresses due to the finite size of the specimen are responsible for this effect (see section 2.4.1).

2.2.4 Crack Pattern Evolution

The short starter cracks developed at an electrical field somewhat lower than the coercive field of 1 kV/mm (figure 2.7 bottom). They all appear within a very small field range. By further increasing the field some grow faster than others and those slower cracks close as the stress is relieved by the faster growing cracks. A decrease in the number of visible cracks is the result. The region between 0.9 and 1.25 kV/mm is characterized by the fastest crack growth (figure 2.7 top). Above 1.25 kV/mm the cracks grow approximately linear with the electric field and finally at about 2.5 kV/mm the specimen saturates and the crack growth is stopped. This behavior agrees very well with the strain hysteresis obtained for that material (solid line in figure 2.3a). The stresses responsible for crack nucleation and growth originate from the strain incompatibility along the electrode edges and therefore the dependence of the stress on the electric field is governed by the strain - electric field relation.

In the case of narrow electrodes some of the starter cracks joined and formed large cracks. Figure 2.8 top shows the crack lengths of two opposing small cracks. The filled dots represent the inner part of the cracks. It can be seen that the inner and the outer part of the cracks initially grow with the same rate. At 1.05 kV/mm the inner parts have attained a critical length and joined by unstable growth.

2.3 Finite Element (FE) Analysis

2.3.1 Linear Piezoelectric FE Analysis

To obtain an insight into the mechanical and electrical fields inside the specimens two finite element modelling approaches were undertaken. In the first approach the experiment was mod-

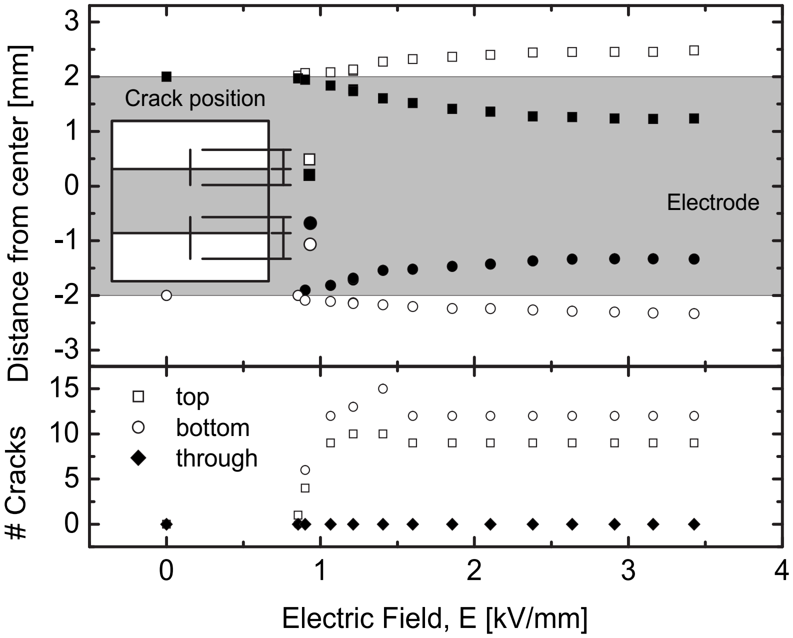

Figure 2.7: (top) Crack lengths measured from the electrode edge for an electrode width of 4 mm. The inner cracks do not join. (bottom) Amount of cracks on both electrode edges and amount of joined cracks.

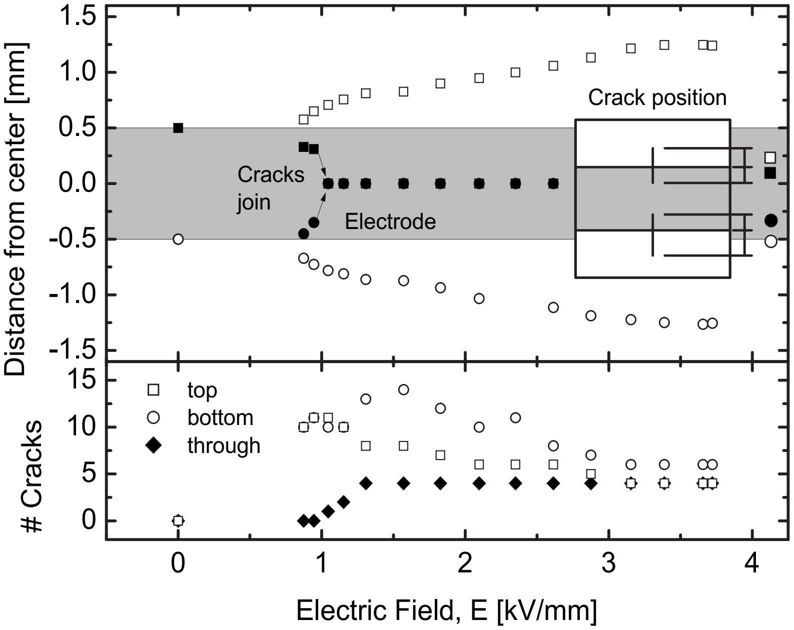

Figure 2.8: (top) Crack lengths measured from the electrode edge for an electrode width of 1 mm. The inner cracks join at 1.05 kV/mm. (bottom) Amount of cracks on both electrode edges and amount of joined cracks.

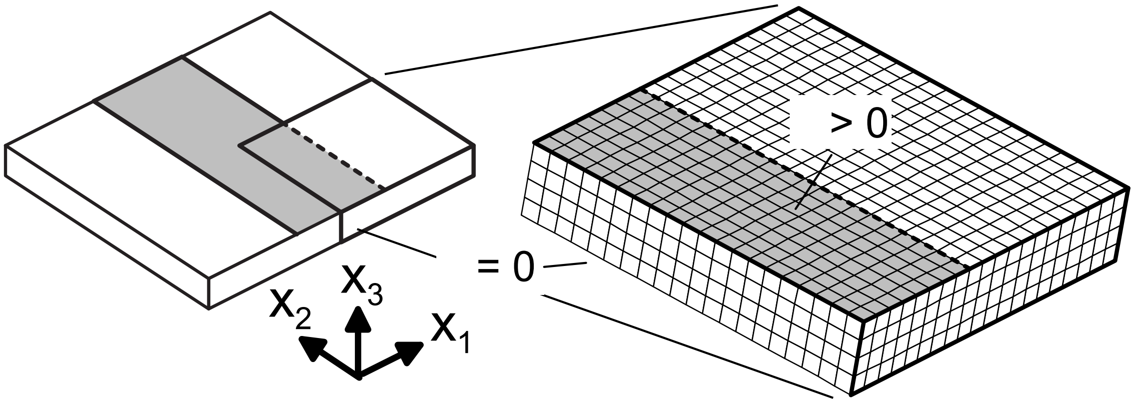

Figure 2.9: Mesh and boundary conditions used in the linear FEM analysis. The front and left surfaces are the surfaces of symmetry. The electrode is shown on the top surface.

elled 3 - dimensionally using the linear piezoelectric element (Solid 5) of a commercial FEM - Code (Ansys 5.5). A rather coarse mesh of about 0.25 mm element size was used, because the geometry is simple and only a qualitative result is desired. The electrodes were implemented by coupling the voltage degree of freedom of the surface nodes. As the electrodes on the real specimens were very thin it was not necessary to model the electrode material. The piezoelectric and mechanical coefficients provided by the manufacturer were used (table C.3). For symmetry reasons only a quarter of the specimen was modelled (figure 2.9).

The boundary conditions were chosen as follows. The bottom electrode was set to a potential of 0 V and the top electrode was set to 1 kV. The symmetry was introduced by fixing the displacements and the electric field of the front and left surfaces in x_1 and x_2 direction, respectively. Finally the displacement in x_3 of the lower left edge was fixed. Three geometries were modelled all with a thickness of 1 mm and electrode widths $2b$ of 1, 2 and 4 mm.

2.3.2 Non-Linear Piezoelectric FE Analysis[1]

In the second approach a finite element tool was used, which is based on a constitutive model taking into account the main ferroelectric and ferroelastic hysteresis phenomena of piezoceramic materials [33, 71]. Finite element tools based on linear piezoelectric behavior are not appropriate for discussion of the influence of ferroelectric - ferroelastic hysteresis phenomena due to switching processes during poling on the electric and stress fields as they presuppose a fixed prepoled state, thus excluding any changes of the poling state by the loading.

The constitutive model is based on an additive decomposition of the polarization and strain into reversible and remnant parts. The reversible parts are related to the electric field and stress by relations possessing the structure of linear piezoelectricity, where, for simplicity the elastic and dielectric tensors are assumed to be isotropic. However, the history dependence of the tensor

---

[1] Cooperation with Dr. M. Kamlah, Forschungszentrum Karlsruhe [70].

of piezoelectric coefficients is chosen such that it is transversely isotropic with the current axis of anisotropy being given by the actual direction and orientation of the remnant polarization.

In order to close the set of constitutive equations, evolution laws in terms of differential equations are needed for the remnant quantities. These quantities can be considered macroscopic averages of the microscopic spontaneous polarization and strain of the domains in the neighborhood of the location under consideration. The evolution laws are constructed by means of four loading criteria of different nature.

The first two criteria indicate the onset of switching processes either due to an electric field above the coercive field or due to a mechanical stress above the coercive stress. The second two criteria indicate either a saturated remnant polarization state or a saturated remnant strain state due to a fully switched domain structure. By means of these loading criteria, the classical dielectric, butterfly, and ferroelastic hysteresis, as well as mechanical depolarization and the field-dependence of the coercive stress are described in a simplifying multilinear manner.

This constitutive law offers the possibility to study the influence of ferroelectric and ferroelastic large signal hysteresis effects on multiaxial stress states in complex components. For this purpose, it was implemented in the finite element code PSU of Stuttgart University for the analysis of quasistatic problems. In this context it has to be noted that the computation times for the nonlinear finite element tool are much higher compared to a linear piezoelectric tool. For further details about the constitutive law and the finite element implementation refer to [33, 71].

In order to reduce the computational efforts to a resonable amount, the finite element analysis of the specimen was restricted to a two dimensional model representing a cross section in the x_1 - x_3 - plane. The plane strain / plane electric field assumption was employed, which is generally considered to well reflect the constraint acting on cross sections situated remote from the free boundary. In our case, the stresses will be overestimated in cross sections close to the free boundary with respect to the x_2 - direction. The electric potential is constant out of plane and thus the electric field components lie in the plane of the calculation.

Exploiting symmetries, only one quarter of the cross section needs to be modelled by a finite element mesh (figure 2.10). The mesh is refined in the neighborhood of the electrode edge with a minimum element size of less than 1% of the half electrode width b. While the singularity directly at the edge might not be described correctly, this is sufficient to represent the electromechanical fields in the neighborhood and still does not require too much computation time.

Material constants of the constitutive law were chosen approximating the behavior of PIC151 (table C.1). The meaning of some constants is given in the first column of table C.1, while the meaning of the other constants can only be understood in the context of the equations of the constitutive model [33].

Two types of boundary conditions are prescribed, where the first type enforces the symmetry conditions. Along the vertical and horizontal lines of symmetry the horizontal and vertical displacements are suppressed, respectively. Furthermore, the electric potential is taken to vanish

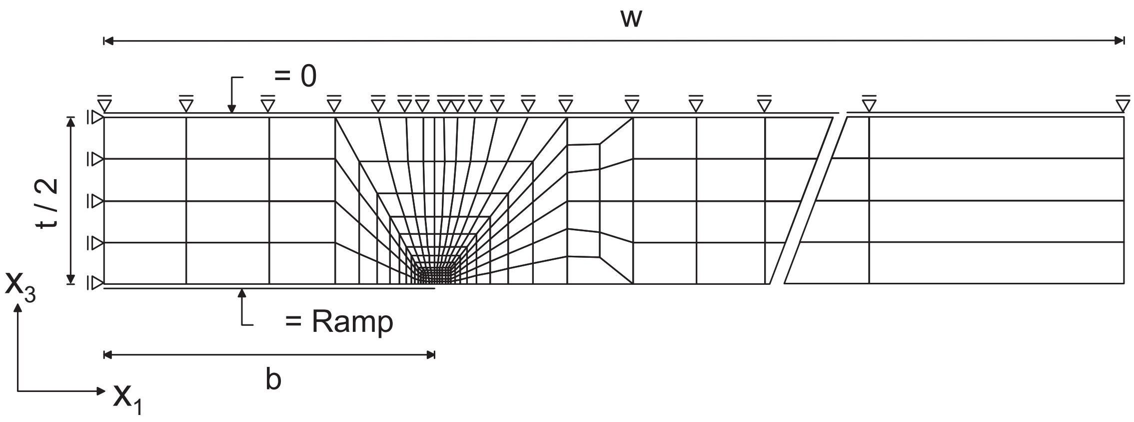

Figure 2.10: Mesh and boundary conditions used in the non-linear FEM analysis. The top and left lines are the lines of symmetry. The electrode is shown below the bottom line.

along the horizontal line of symmetry. The second type of boundary conditions refers to the loading, which is given by an electric potential at the electrode as a ramp-like history such that it terminates at a nominal electric field of 2.0 kV/mm. For those parts of the boundary, where nothing else has been stated, zero stresses and dielectric displacement are implied. Thus, besides the limitations due to the plane strain assumption discussed above, the loading of the specimen is fully represented. In this analysis four geometries were modelled. The first geometry with a thickness of 2 mm and an electrode width $2b$ of 4 mm is used to discuss the basic behavior. A variation of the thickness (0.5, 1 and 2 mm) with $2b = 1$ mm is used for the thickness dependence.

2.4 Finite Element Results

2.4.1 Linear Piezoelectric FE Results

The first principal stresses on the specimen surface as calculated by a linear piezoelectric FEM are shown in figure 2.11. The actual crack pattern obtained for a specimen of the modelled geometry is overlaid while the electrode area is marked in grey. It can clearly be seen that the cracks grow perpendicular to the first principal stresses (black arrows). Due to piezoelectric deformations of the specimen shear stresses are introduced in a large volume of the specimen. In fact, only a very small region around the x_1 center line is not affected. A comparison to specimen with less electrode coverage shows that the shear stresses influence a zone approximately equal to the electrode width.

Along the $x_1 - x_3$ symmetry plane the principal stresses are almost entirely given by the stresses in x_2-direction. For small electrode coverages the stresses in the x_2-direction are sufficient to discuss the crack initiation problem in a 2-dimensional non-linear analysis.

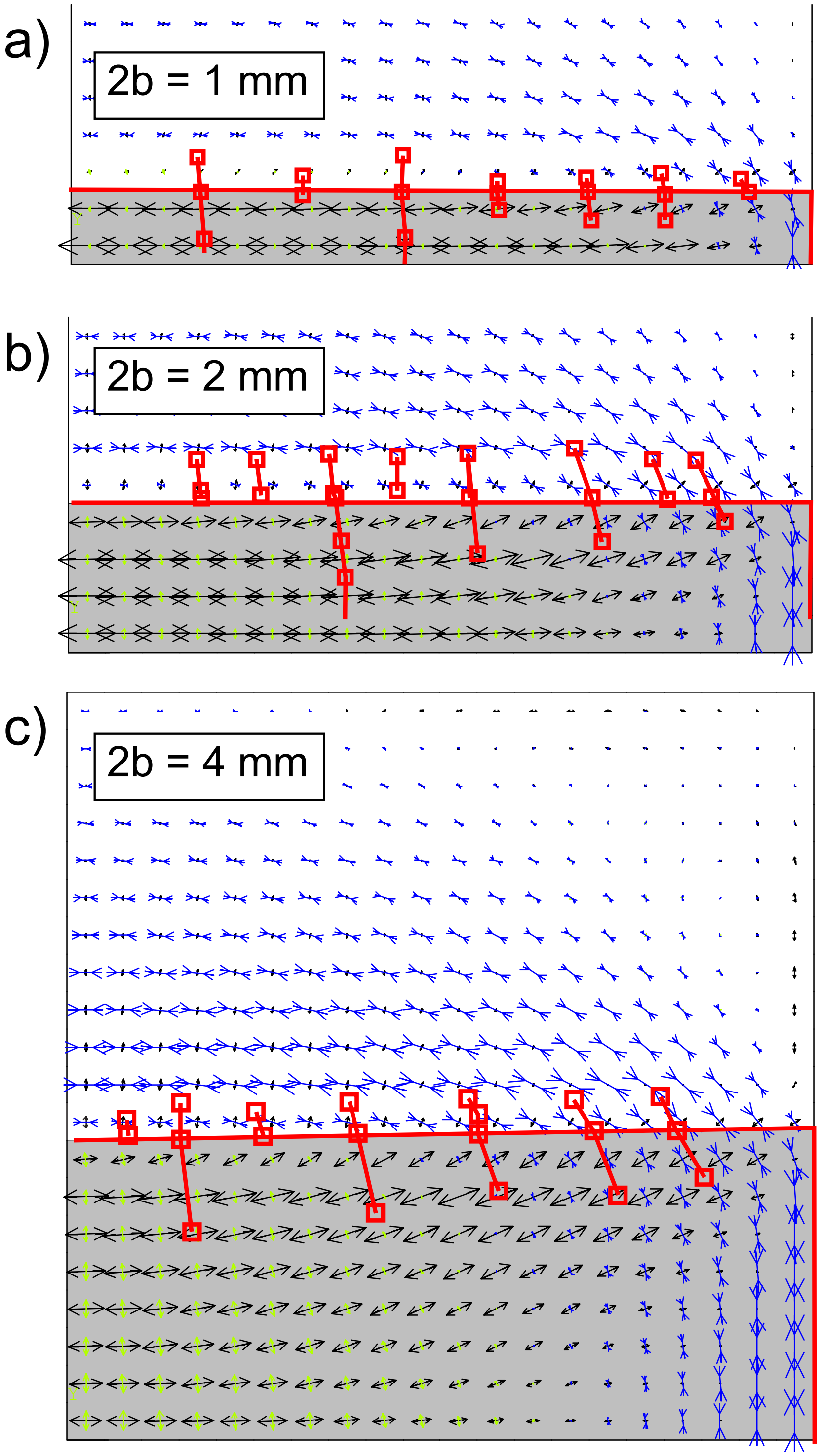

Figure 2.11: Top view on the direction and magnitude of the principal stresses (1st black, 2nd green, 3rd blue) in a quarter of the specimens with an electrode width $2b$ of 1 mm, 2 mm and 4 mm. The crack patterns obtained from real specimens are overlaid in red and the electrode area is marked gray.

2.4.2 Non-Linear Piezoelectric FE Results[2]

Analytical calculations predict a field singularity at the electrode edge. It can be seen in figure 2.12a that non-linear FEM analysis also yields extremely high electrical fields underneath the electrode edge and fringing fields outside the electrodes. Yet, the specimen both inside and outside the electrode does not experience an electric field high enough to induce domain switching. Only a small region under the electrode edge is subjected to electric fields large enough to switch domains. The dielectric displacement serves as a measurement of the amount of domains switched (figure 2.12b). That region acts against the remainder of the specimen and generates high localized stresses parallel to the electrode edge (figure 2.12c). The calculations were made for a nominal electric field of 1 kV/mm, that is a field just below the coercive field.

The calculations were continued up to a nominal field of 2 kV/mm. The resulting electric fringing fields (figure 2.12d) will lead to domain switching outside the active volume as can be seen from figure 2.12e. A width of about half the sample thickness is affected by the fringing field. In the surface near region the direction of the electric field leads to an almost horizontal domain orientation (figure 2.12j). Far outside the electrodes no resulting dielectric displacement is seen. The mechanical stresses parallel to the electrode edges (x_2 - direction) as calculated by non - linear FEM are shown in figure 2.12(f-i) for different geometries. They follow a similar pattern as the electric displacements. A zone of high tensile stresses is located directly underneath the electrode edge. Outside of the active volume the specimen is under low compressive stresses. In the center of the active material the tensile stresses increase from the middle to the surface of the specimen.

The size of the zone where high stresses are obtained in the bulk underneath the electrodes, is much larger in thick specimens than in thin specimens (figures 2.12f-h). Yet, it does not depend on the electrode width (figures 2.12h-i).

2.5 Discussion

The macroscopic parameters can be explained by the global strain mismatch in the specimen. The crack initiation and growth on the other hand have to be interpreted by localized edge effects. These edge effects dominate at voltages around the coercive field of the bulk material. At higher fields the global material response dominates over the local effects.

2.5.1 Local Effect

At low applied electric potential differences only a small region underneath the electrode edge will experience a field high enough to induce domain switching (figure 2.12b). The electric field in the volume between the electrodes will facilitate domain switching due to mechanical stresses,

---

[2] Results from cooperation with Dr. M. Kamlah, Forschungszentrum Karlsruhe used [70].

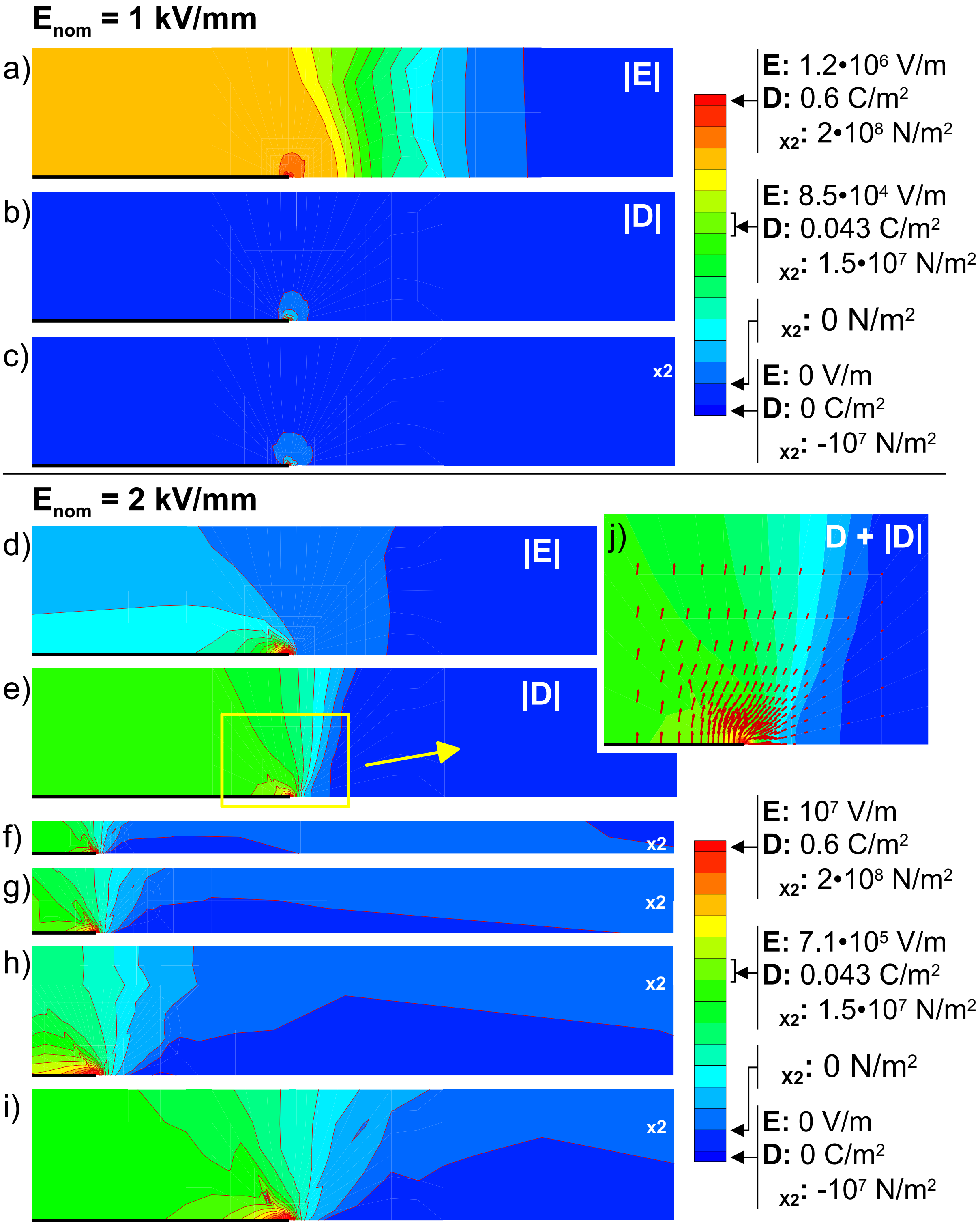

Figure 2.12: Result of the non-linear finite element analysis. The nominal electric field was 1 kV/mm for a)-c) and 2 kV/mm for d)-i). a) Distribution of the electric field with the maximum values under the electrode edge. b) and e) Illustration of the dielectric displacement. c) and f) through i) Stresses in the x_2 direction (out-of-plane) for different geometries. j) Vector illustration of the dielectric displacement around the electrode edge in e).

but the field values are too low to induce ferroelectric switching here. Thus we encounter the case that a very small volume of half - cylindrical shape underneath the electrode edge attempts to switch against the entire remainder of the sample volume. Because of the shape of this switching volume it will be referred to as “half - cylinder”. A strain mismatch arises if two competing volumes differ in strain. The competing volumes are a half - cylinder underneath the electrode edge and the remainder of the specimen. Only very small compressive stresses are present in the bulk and very high tensile stresses in the half - cylinder, but confined to such a small volume that it barely shows in figure 2.12c.

Due to the finite size of the specimens, the specimen is not fully clamped in x_2 - direction for cases with electrode coverage larger than about 30%. At about 50% a strong bending of the specimen edges towards the center is observed which is also responsible for the radial crack pattern. This will reduce the local tensile stresses to some extent but shear stresses are introduced. With even wider electrodes the bending and the overall clamping will be further reduced. The strains in both x_1- and x_2-direction stay almost constant between 80% and 100% electrode coverage.

As the specimens consist of a ceramic material with natural flaws, small defects will be located in the half cylinder under tensile stress. Some of those defects will be greater than a critical size and cracks will be initiated. A further increase of the electrical field prompts a further extension of the critical tensile stresses into the material. Stable crack growth ensues both underneath the electrode and into the outside. Once the global effects dominate over the electrode edge effect the cracks may split the volume underneath the electrodes into separate parts according to the mechanisms discussed in 2.5.2. If two cracks from opposing electrode edges are large enough they will coalesce (see section 2.2.4).

2.5.2 Global Effect

Increasing the electric field the volume between the electrodes now acts against the inactive volume outside, resulting in (x_2-) tensile stresses in the active volume and compressive stresses in the inactive volume. The global tensile stresses are thus readily explained.

The change in the field values for the inflexion point is slightly more subtle. The mechanical stresses generated by the strain incompatibility hinder the extension of the material between the electrodes in the direction of the applied electric field. The elastic-ferroelastic material behavior transfers tensile stresses in x_2-direction into an effectively compressive stress in x_3-direction. In the purely elastic case this would be solely due to Poisson’s ratio, in ferroelastic materials this is also due to volume constancy of domain switching. Due to partial domain switching the actual material behavior lies between these two limiting cases. As the clamping is only along the x_2-direction the specimen is not fully clamped in the electrode plane and the boundary conditions are not entirely plane strain. This is in good agreement with measurements done by Lynch [10]. A considerable decrease of the strain hysteresis was observed while the specimen was exposed to a compressive stress in x_3-direction.

Yet, the clamping does not explain why the apparent strains in x_1-direction exceed the value for the free sample. This fact is due to the electrical fringing fields (see also figure 2.12e). As the electrode width is used as reference length to determine the strain from the surface displacements, the strain is only normalized to the volume underneath the electrodes. For electrodes narrower than the thickness the active volume as defined above is of the same size as the volume affected by the fringing field. In case of very narrow electrodes the fringing field far exceeds the active volume and the strains are greatly overestimated.

The alternating crack pattern observed in some geometries is another expression of the global strain incompatibility as it develops during crack growth driven by the increasing stresses. In thermal shock experiments on glass ceramic [30] the critical crack length required for the development of the alternating pattern could be related to the distance between the cracks. The larger the spacing the higher the critical length that has to be attained. The argument is that a crack unloads its environment up to a distance of roughly its length. Initially the cracks are all short and so is the unloading range and therefore many cracks can grow. As the cracks grow, more cracks have to be left behind because the still growing cracks unload larger parts of the specimen. A similar rule is valid in case of the electrode edge cracks. The crack spacing in all specimens of 1 and 2 mm thickness is almost identical. Thus e.g., the crack length in a 1 mm thick specimen with an electrode width of 6 mm is very short and no alternating pattern has developed (figure 2.6). On the other hand in a specimen with $b = 4$ mm the cracks are quite large and an alternating pattern is observed.

2.5.3 Thickness Effect

The size of the zone where the high stresses are obtained is correlated to the specimen thickness. A certain electrical field within the approximately singular region at the electrode edge (equation 1.12) depends on the applied voltage. The voltage, however, has to be increased in thicker specimens to obtain the same electric field in the bulk. A qualitative expression of the size of the half-cylinder can be obtained from equation 1.13. In an actuator the electric field intensity factor is given by $K_E = \Omega E_{appl.}\sqrt{t}$ [63] with Ω being a geometry term independent of t. The size of the half-cylinder r_{switch} in which switching occurs becomes

$$r_{switch} = \left(\frac{\Omega E_{appl.}}{E_C}\right)^2 \frac{t}{2\pi}. \tag{2.1}$$

For a constant nominal applied electric field, the half-cylinder scales linear with the layer thickness h, which agrees well with the FEM-results in figures 2.12f-h. As failure in ceramics is governed by weakest link statistics, both the magnitude of local stresses as well as their extension are crucial. Therefore, more edge cracks are formed in thick specimens since the volume of high stresses given by the volume of switched domains around the electrode edge is larger (compare figures 2.12f-h).

In specimens with a thickness of 0.5 mm no or only very few cracks are observed, while thicker specimens showed a large amount of cracks. This might be a clue that the tensile stresses are not high enough to induce cracking and / or that their extension is very small and therefore only few defects are located within. The effect that causes the coercive field in those specimens to remain constant for different electrode coverages and even for a fully covered specimen has yet to be understood. A major difference between the specimens with a thickness of 0.5 mm and the thicker specimens is that the former are almost entirely in plane stress while the latter are mostly in plane strain. Thickness dependent R-curve effects as measured in section 3.2.1 do not contribute at this stage as the cracks are too small.

A more detailed fracture mechanical description of the stress intensity factor of a flaw ahead of the electrode tip is available [63, 64], which allows to introduce a criterion for the lower thickness t_c of the layer under which no cracking should occur (equation 1.14) [64]. With the measured material properties $K_{IC} = 1.3$ MPam$^{\frac{1}{2}}$ [38], $Y = 66.5$ GPa [72] and $S^S = 0.004$ (figure 1.2) and a conservative approximation on the relationship $E_S/E_{appl.} = 5$ [64] the critical layer thickness comes out to be $t_c = 4.85$ mm. That value is about an order of magnitude larger then the experimental findings of 0.5-1.0 mm. If other values for the applied electric load are used (e.g. $E_S/E_{appl.} = 2$) t_c becomes 0.76 mm and gets in the range of the experimental findings. It has to be stated that the material properties used are rounded values and the underlying geometry in equation 1.14 is that of a real multilayer structure which is not used in these experiments.

Specimens with a thickness of 1 mm and 2 mm show almost the same amount of cracking. This leads to the conclusion that there might not only be a lower thickness limit for cracking but also an upper thickness limit for the maximum cracking. Thicknesses over the upper limit will not result in more cracks. In order to induce cracking, the half-cylinder of tensile stresses underneath the electrode edge have to have a minimum extension r_{min}. This size is assumed to be independent of the actual thickness as in this stage the local effects dominate. Once the applied voltage for a given thickness has lead to a half-cylinder of the critical size, cracking will begin. Now, each crack will relieve a certain volume where no new cracks can nucleate. A maximum possible crack density results. By increasing the electric field the extension of the half-cylinder is increased (equation 2.1) and the cracks are driven to larger sizes. Only a few cracks will still nucleate at this early crack growth stage and none in later stages as can be seen in figures 2.8 and 2.7. By increasing the thickness of the specimen the maximum possible extension is also increased. But since the actual size is also given by the applied electric potential which starts at zero, the critical extension r_{min} is obtained with a lower voltage than in thinner specimens and cracking will start. Once the maximum crack density is reached, the increased extension of the half-cylinder will only lead to larger but not to more cracks as can be seen in figure 2.6.

The different cracking behavior is reflected in the dependence of coercive field on the electrode coverage. Mechanical clamping in x_2 - direction yields very high tensile stresses around the electrode edge and moderate tensile stresses between the electrodes. The localized stresses around the electrode edges will initiate cracks which in turn relieve some of the stress. As more energy is needed to switch the domains in the electric field direction (x_1 - x_3 - plane) with tensile stresses present in x_2 - direction the coercive field increases. Cracks will reduce the stresses and therefore the coercive field will also be reduced to an extent correlated to the amount and size of electrode edge cracks. Additional stresses are relieved by the inward bending of the specimen. But since there are still stresses in the specimen, the coercive field will be higher than in a free specimen.

The dependence of the coercive field on the electrode coverage seems to require cracking. In the 0.5 mm tick specimens no cracking is present and the coercive field does not depend on the electrode coverage. On the other hand the large cracks do not influence the coercive field or the achievable strain. They are localized in the interior of the specimen and have no effect on the bulk specimen.

Chapter 3

Mechanically Driven Crack Growth

In this part, crack - resistance curves for different geometrical and polarization conditions will be measured. Two sets of experiments are performed. In the first set the sample thickness dependence is investigated. The second set consists of a variation of the polarization state for a sample thickness of 1 mm. They are used for the fracture mechanical modelling of the electrically driven crack growth. Furthermore, a high voltage poling equipment used for voltages up to 150 kV is introduced.

3.1 Experimental Methods

3.1.1 Specimen Preparation

The mechanically driven crack growth was investigated by measuring R - curves in compact tension (CT) geometry. All experiments were performed on the batches S3, S4 and S5. Specimens of the batch S3 were used to investigate the influence of sample thickness on the R - curve. The batches S4 and S5 were used to measure R - curves needed for the fracture mechanical analysis of the electrically driven crack growth described in chapter 4. The experiments on the batch S4 were performed on unpoled specimens only, while the specimens of the batch S5 were all poled in plane either parallel or perpendicular to the crack growth direction.

The specimens of the batch S3 were delivered as plates of 35 × 33.6 mm^2 with thicknesses of 1 and 3 mm. Some of the 1 mm thick specimens were ground down to 0.5 mm. Batch S4 contained plates of dimensions 40 × 40 mm^2 with a thickness of 1 mm which were cut to 35 × 33.6 mm^2. The plates of batch S5 were 1 mm thick with a dimension of 35 × 33.6 mm^2. Plates with 0.5 mm thickness proved too fragile for mechanical loading. Therefore, R-curves for the fracture mechanical analysis were obtained using 1 mm thick plates.

All batches underwent the same preparation procedure. First one of the large surfaces was polished to a 1 µm finish by the same procedure as in 2.1.1. Due to different polishing times for the different specimens, a small variation of the final thicknesses was obtained. They were then cut and ground to the final geometry and poled if needed. In the last preparation step two holes were drilled using a diamond drill and a notch was cut on the surface grinder (ZB 42T, Ziersch & Baltrusch).

3.1.2 Poling

Poling was always done at an electric field corresponding to 1.5 E_C. The electrodes for poling were silver - painted on the surfaces. Due to the size of specimens an electric field of 1.5 E_C corresponds to voltages of up to 52.5 kV (along the 35 mm length). Particular care had to be taken to avoid breakdown at these high voltages. A special poling device was built using components of Fischertechnik (Construction - set of Nylon) and kept in a plastic bucket filled with silicone oil (AK 35, Wacker). The setup is displayed in figure 3.2.

Voltages of 0 - 230 V with a maximum power of 8.8 kVA were set by a voltage regulator (AEG). A secondary transformer amplified the voltages by a factor of 650 resulting in a maximum voltage of 149.5 kV. The alternating current was rectified by two diodes and smoothed by two capacitors with a total capacity of 11.2 nF. A resistor of deionized water (approx. 2 MΩ) limited the current in case of electrical breakdown. The applied voltage was measured by a voltage divider (200 MΩ by 10 kΩ, 1:20000) with a digital voltmeter (M-4650 CR, Voltcraft) connected parallel to the specimens. An analog ammeter (AEG) connected between the specimen and ground was used to observe the current into the specimen. The circuit diagram is provided in figure 3.1.

The voltage was manually increased within 10 min up to the maximum field, held for 60 s and then decreased within 5 min to 0 V. A maximum drift of the voltage of about ±300 V was maintained throughout the poling process. Finally the electrodes were washed off with acetone.

3.1.3 R-Curve Measurement

The R - curves were measured in a specially designed compact tension frame (ARCO - CT, TU Darmstadt) that was mounted on the coordinate stage of the optical microscope. The test

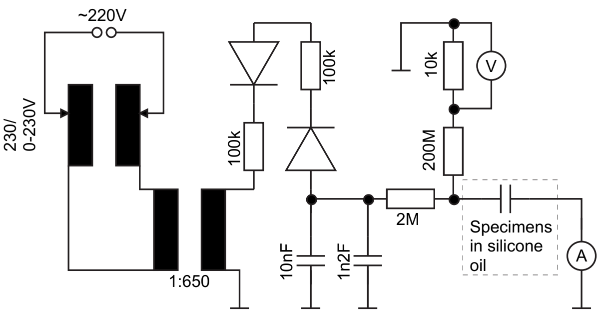

Figure 3.1: Circuit diagram of the poling device.

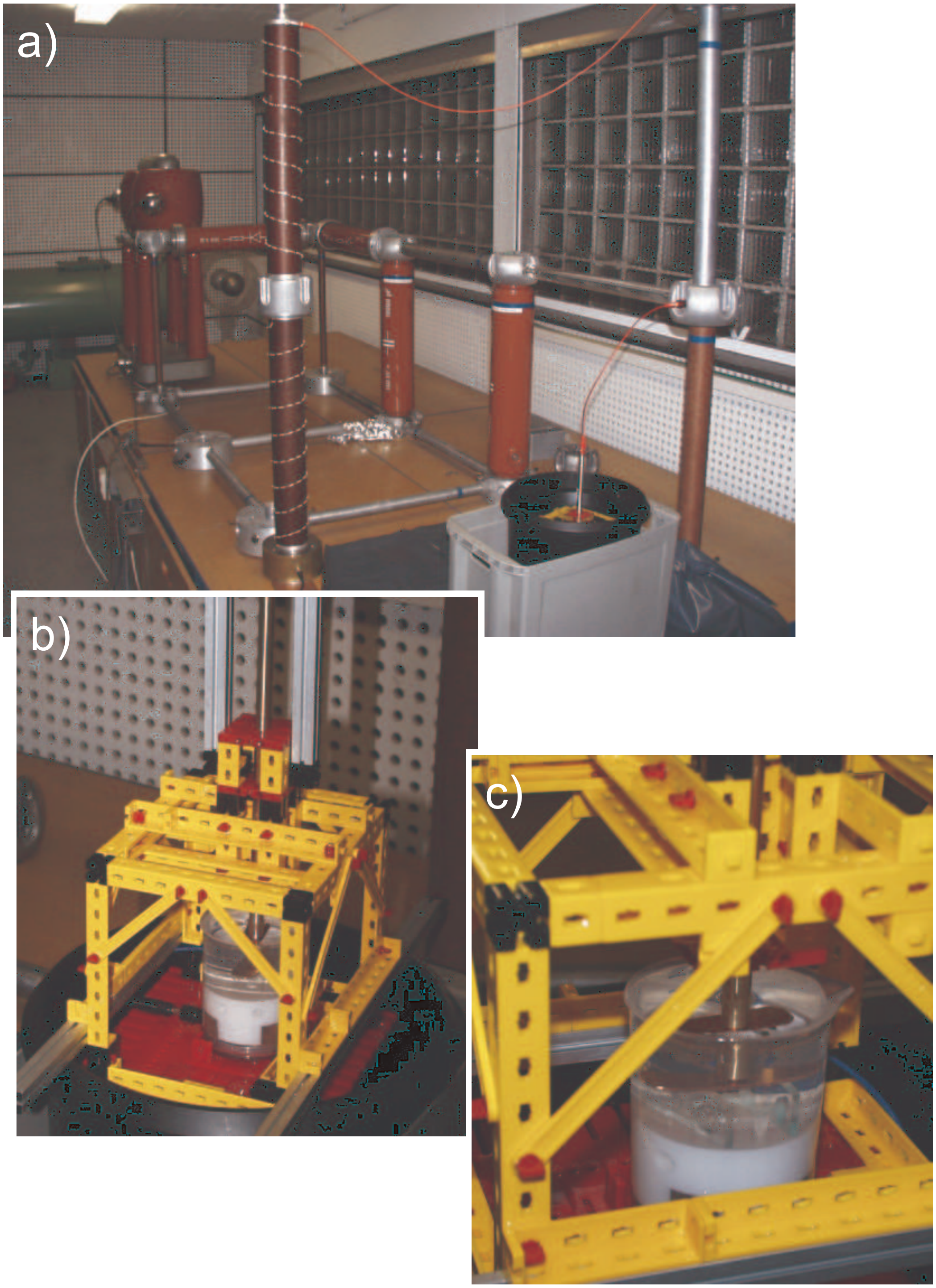

Figure 3.2: a) High-voltage equipment for poling the CT-specimens. The bucket filled with silicone oil for the poling frame is located in the lower right. b) Poling frame with the specimen fixture. c) Specimen fixture for CT-specimens.

itself was performed based on ASTM 399 [73] with some modifications described later. In the present investigation the minimum thickness requirement ($2.5(K_I/\sigma_Y)^2 \leq t$) was not always fulfilled. But the R-curves were intended to be measured for the fracture mechanical analysis of the electrically driven crack growth. They therefore had to be measured in specimens with the same thickness as the specimens used for the electrically driven case.

Prior to the R - curve measurement a sharp pre-crack was produced cutting a half chevron - notch with a diamond wire saw (4240, Well) and placing a Knoop indent (Finotest 38160, Frank) at a load of 50 N in the thin material ligament. After the pre-crack had been driven through the region of the half chevron notch, it was renotched to a final length of approx. 600 µm. The end of the notch was used as origin for the crack extension Δa. Specimens thinner than 3 mm were mounted between two spacers on both sides to ensure a centered position in the load frame as the load frame was built for a thickness of 3 mm. The spacers were from the same sample material and had the same geometry and material properties as the actual specimen. To reduce friction between the load arm and the specimen the polished side of the spacers was mounted towards the load arms.

The load was applied in displacement - control by a preload screw and a piezo - actuator (PI Ceramic). A load cell (FMD 1 kN, Wazau) located in the loading path was used to measure the applied load with an accuracy of ±1 N. A computer with a custom designed software (see appendix B.4) connected to the stage was used to read out the stage coordinates and the applied load. The crack length was obtained by targeting the crack - tip with the crosshairs in the eye pieces. With the crack length and applied load known the applied stress intensity factor and the crack growth velocity were calculated in real - time by the data - acquisition - software. To ensure maximum reproducibility, special care was taken to record data at crack velocities at about 10^{-6} m/s and unlike in previous experiments the crack was not unloaded at any time. A data point was recorded every 25 µm up to the final crack extension of about 5 mm.

The measurement procedure for the thickness dependence was a little bit different in that the data were recorded manually without the data - acquisition - software. To do this the crack was stopped after each data point by slightly unloading the specimen. By reloading the next data-point was acquired at the onset of crack propagation. Furthermore the specimens were renotched to a starter crack length of approx. 150 µm. Since this procedure proved to be very time consuming and to be problematic by adding the uncertainty of unloading the crack, the automatization software was written for the other measurements.

3.2 Experimental Results

3.2.1 Thickness Dependence of R-Curves

Although the specimens were renotched, they were not thermally depolarized after growing the starter crack. The initial value of the R - curve could therefore not be measured with high

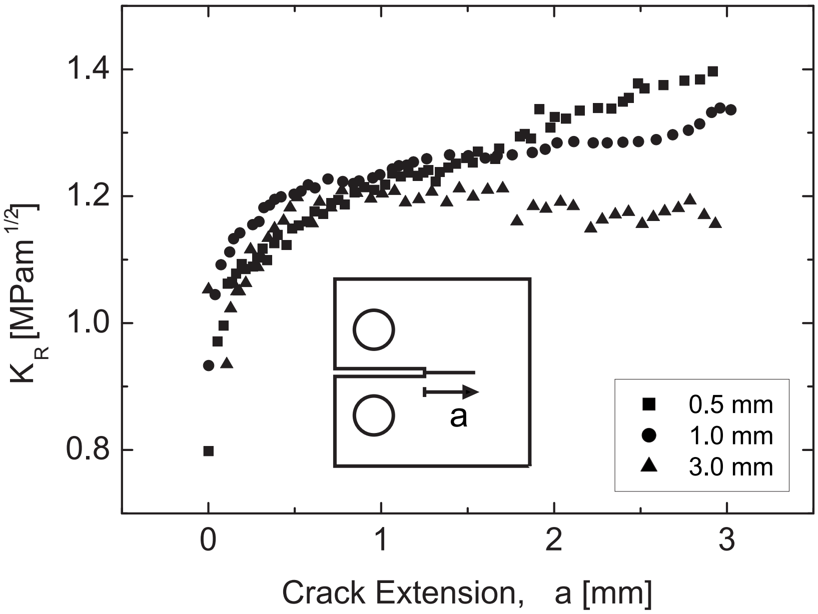

Figure 3.3: Thickness dependence of R-curves for unpoled specimens.

precision. Another difficulty arises from the fact that it is difficult to distinguish real crack growth from a crack already present that is reopening by reloading. The measured starting values for all specimens were between 0.8 and 0.9 $\text{MPam}^{\frac{1}{2}}$.

The three different thicknesses resulted in two distinctly different R - curve - behaviors. The 3 mm thick specimen reaches the plateau of 1.2 $\text{MPam}^{\frac{1}{2}}$ after about 1.5 mm as in previous measurements [38]. Such a plateau could not be identified within the first 3 mm of crack extension in the thinner specimen. After a similar increase in toughening in the first 1 - 1.5 mm, the fracture toughness in the 1.0 mm and 0.5 mm thick specimen continued to increase almost linearly (figure 3.3) with a slightly steeper slope in the 0.5 mm specimen. It will be shown in the next section that an equilibrium is attained only after 4 mm crack extension.

Specimens of 0.5 mm thickness proved very difficult to prepare as they are very fragile. Another problem arises from the low strength of the specimens. With loads in the range of 8 - 11 N the error of the load cell is almost 20%. Thicker specimens required a load of 20 - 24 N (1 mm) and 36 - 51 N (3 mm) which is still low but in an acceptable range. Moreover, the crack growth direction in the 0.5 mm thick specimens was very unstable. In only one of three specimens the crack grew perpendicular to the load points which indicates that shear stresses are introduced either by bending of the thin plates or by friction with the load-arms.

3.2.2 Polarization Dependence

Given the problem with the specimen preparation and the equipment with the thin specimens it was not recommended to use them for precise measurements. Yet, the specimens used for electrically driven crack growth had a thickness of 0.5 mm and therefore the CT - geometry should not differ too much from this value. Measuring the R-curve using plates of 1 mm thickness proved to be the best possible compromise, because the difference to the thinner geometry is not very large.

Due to the same problems as in the thickness-dependent measurements, the initial value of the R - curve could not be measured with high precision. The R - curves in the unpoled specimens start at about 0.8 - 0.9 MPam$^{\frac{1}{2}}$ in figure 3.4a. A steep rise up to 1.15 MPam$^{\frac{1}{2}}$ is observed in the first 500 µm of crack extension. It changes into a linear increase of the fracture toughness up to an extension of about 3.5 mm after which the fracture toughness remains constant. These final toughness values are termed plateau values and range from 1.37 MPam$^{\frac{1}{2}}$ to 1.45 MPam$^{\frac{1}{2}}$. The corresponding crack growth velocity is shown in figure 3.4b. The crack growth velocity was maintained at about 10^{-6} m/s with deviations of less than a factor of 3.

Only one specimen survived the poling in the direction parallel to the crack. The resulting R-curve coincides almost entirely with the measurement in the unpoled specimens. After a start at 0.93 MPam$^{\frac{1}{2}}$ and a steep rise up to approx. 1.18 MPam$^{\frac{1}{2}}$ a linear part followed up to the plateau value of about 1.38 MPam$^{\frac{1}{2}}$ (figure 3.5a). While only very few and very small bridges were observed in the unpoled material, many smaller and several large bridges were seen in the parallel poled material. The large bridges can be seen in the velocity plot (figure 3.5b) at $\Delta a = 3$, 4 and 5 mm and are marked by arrows in figure 3.5a. The latter two stretched over a length of over 500 µm.

Like for the parallel poled specimens only one perpendicular poled specimen was available after preparation. The R-curve in the specimen poled perpendicular to the crack started at about 0.8 MPam$^{\frac{1}{2}}$ and increased at the same rate as the parallel poled specimen up to the plateau value of approx. 1.75 MPam$^{\frac{1}{2}}$ (figure 3.5). At a length of 0.75 mm the first large crack bridge developed and the crack jumped forward by approx. 130 µm. The R-curve increased before and decreased slightly after every bridge. Perpendicular poled specimens contained many more bridges than the parallel or the unpoled specimens. The lower plateau value agrees well with measurements in thick plates [38].

3.3 Discussion

3.3.1 Thickness Dependence

It is known that the fracture toughness in plane stress is higher than in plane strain, because the constraints for yielding are reduced. A larger zone of plastic deformation or in case of a

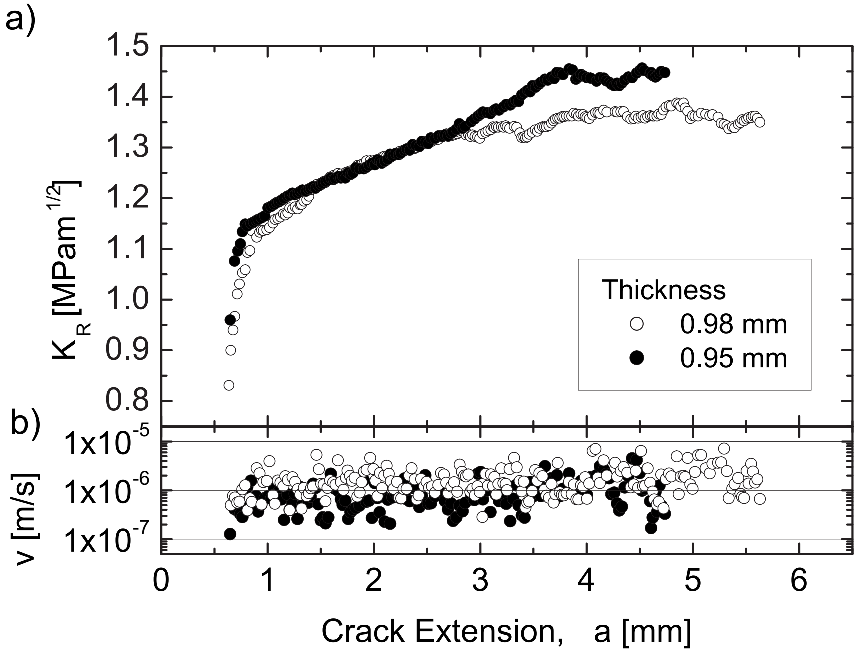

Figure 3.4: a) R - curves for unpoled material. b) Crack growth velocity before each data point.

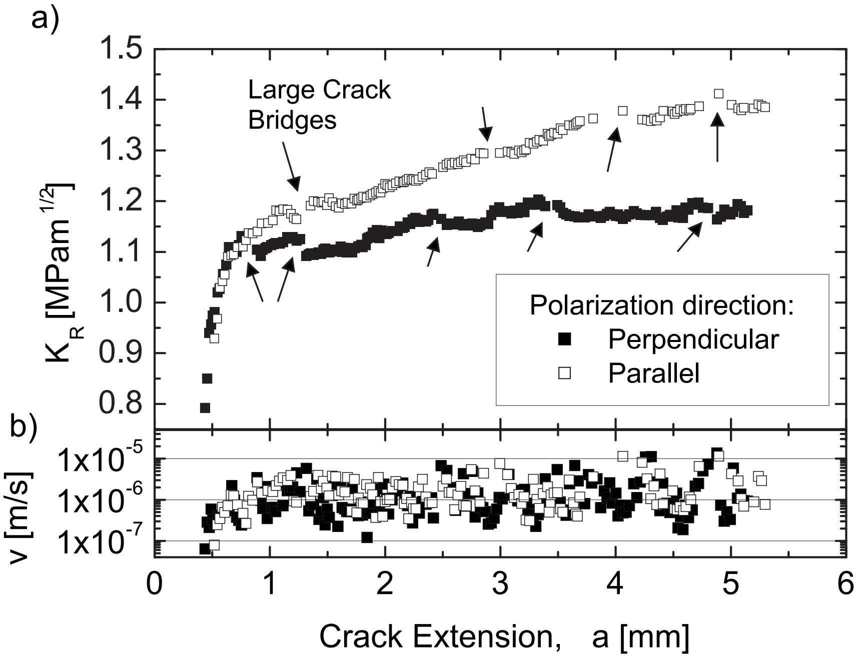

Figure 3.5: a) R - curves for material poled parallel and perpendicular to the crack. Large crack bridges (> 100 µm) are marked by arrows. b) Crack growth velocity before each data point.

ferroelastic material a larger zone of domain switching results. The effective stress state can be estimated using calculations of the plastic zone size as a function of specimen thickness [74]. No plane strain influence is therefore obtained if $K_I/(\sigma_Y\sqrt{t}) \gtrsim 2$. With a yield stress of $\sigma_Y = 53$ MPa [75], a fracture toughness of $K_I = 1.3$ MPam$^{\frac{1}{2}}$ [38] and a Poisson coefficient of $\nu = 0.37$ [72] the zone size of a 0.5 mm thick specimens comes out to be almost entirely given by the plane stress zone size. For a 3 mm thick specimen $K_I/(\sigma_Y\sqrt{t})$ is equal to 0.63 and is well within the ASTM requirement of $K_I/(\sigma_Y\sqrt{t}) \leq 0.89$. The 1 mm thick specimens are in between so that the full spectrum from plane strain to plane stress is covered by the analyzed thicknesses. Yet, the resulting plastic zone size for $t = 3$ mm after [74] of about 0.02 mm is one order of magnitude smaller than what could be measured by the liquid crystal (LC) method [20].

Taking the stress - strain curves for the investigated material [75] into account, it can be seen that the first deviation from the purely elastic behavior, i.e. the first domain switch, occurs at approx. 20 MPa, while the coercive stress as defined by the inflexion point is approx. 54 MPa. An estimate of the extension of the process zone using equation 1.5 with the above material properties, yields a radius of 0.67 mm for 20 MPa and 0.09 mm for 53 MPa. The process zone will therefore start approx. 0.7 mm away from the crack tip with a low fraction of switched domains which will increase with increasing proximity to the crack tip. It is therefore problematic to use a switching rule based solely on the coercive stress for a macroscopic problem. The variation of the fraction of switched domains should be taken into account for a more realistic model.

As the thin specimens are in plane stress and the ferroelastic toughening depends on the macroscopic stress state (following the Tresca criterion), the R-curve depends on specimen thickness. A clear transition between plane stress and plane strain is visible in the R-curves in figure 3.3 such that the process zone seems to be significantly larger in plane stress and therefore the equilibrium crack length is not reached within the first 3 mm of crack extension.

The general behavior of the 0.5 mm and the 1 mm thick specimens is comparable and the absolute difference between the two is less than 10%. Using R-curves measured on 1 mm thick specimens to describe the behavior of 0.5 mm thick specimens seems to be an acceptable compromise, especially taking into account the handling problems with the 0.5 mm thick plates.

3.3.2 Polarization Dependence

As only one result is available from the poled specimens for each poling direction, the conclusions have to be drawn carefully. The difference between the two poled states is relatively small and the scattering within one polarization state is quite large.

The perpendicular poled specimen shows the lowest fracture toughness as the domains are already oriented in the direction of crack closure. Therefore, no closure stresses can be obtained, because no domains would switch under the crack tip stress field if the poling were perfect. However, no perfect poling is possible in a polycrystal, because not all domains will switch during the poling process and some will switch back after the poling process due to mechanical constraints. Those domains can be activated by the high mechanical crack tip stress field and yield some toughening. Additionally there is still the linear piezoelectric effect that will also contribute to toughening.

In specimens poled parallel to the crack the domains could switch by 90° to the perpendicular direction and yield a significant toughening. But the material around the crack tip is mechanically constrained by the surrounding material and thus domain switching is hindered.

Unpoled specimens and specimens poled parallel to the crack show almost the same R-curve. That is in contradiction to measurements with thicker specimens [38] in which the parallel poled specimen attained a significantly lower fracture toughness. The mechanical clamping responsible for the lower toughness in thick specimens seems not to be present in 1 mm thick specimens, or if it is, then only to a small degree and might be responsible for the intensified crack bridging not found to that level in thicker specimens. Yet, since the poled and the unpoled specimens originated from different batches the results cannot necessarily be compared. Previous measurements showed that two sintering batches of the same material can differ by up to 15% [38].

Chapter 4

Electrically Driven Crack Growth

The crack growth behavior is investigated in this last part. A variation of the electrode coverage and the polarization state is used for different crack driving forces in analogy to thermal shock experiments. The crack driving force itself is calculated from displacement measurements on the same geometry. Both the crack path as well as the crack propagation are studied as function of the applied electric field. Fracture mechanical analysis is used to simulate both and to investigate the governing parameters.

4.1 Experimental Methods

4.1.1 Specimen Preparation

All experiments on electrically driven crack growth were performed on the batches S4 and S5. The specimens of the batch S4 were delivered as plates of dimensions 40 × 40 mm^2 with thicknesses of 0.5 mm. The batch S5 was ordered as plates of dimension 40 × 40 mm^2 with a thickness of 0.5 mm. They were polished on one side to a 1 µm finish by the same procedure as in 2.1.1. Due to different polishing times for the different specimens, a small variation of the final thicknesses was obtained. Some of the 0.5 mm thick specimens of both batches were cut to 20 × 20 mm^2.

Two sets of experiments were done. In the first set the electrically driven crack growth was investigated in unpoled specimens. For this study only specimens of the batch S4 were used. The second set of experiments were concerned with prepoled specimens. Here only the batch S5 was used. These specimens were poled according to 4.1.2 after polishing and before further preparation steps. The R-curves were measured with specimens of the respective batch (chapter 3).

The preparation procedure for the displacement and crack propagation measurement was similar to the procedure for the crack initiation experiments (section 2.1.1). First electrodes of approx. 50 nm of gold / palladium (80% / 20%) were sputtered onto 40 × 40 mm^2 specimens

Table 4.1: Electrode geometry of the specimens for electrically driven crack growth. A size of 40×40 mm^2 is used unless marked different.

	Exact electrode width b and thickness t for a nominal width of		
Polarization[a]	1 mm	2 mm	3 mm
unpoled	1.07 mm / 0.44 mm	1.95 mm / 0.51 mm	
		1.87 mm / 0.31 mm	
parallel	1.16 mm / 0.46 mm	2.06 mm / 0.46 mm	
		2.03 mm / 0.47 mm	
perpendicular		2.12 mm / 0.46 mm	2.89 mm / 0.46 mm[b]

[a] relative to the electrode edge

[b] specimen with $L = 40$ mm and $W = 35$ mm

(plasma current 40 mA, sputter time 200 s). The partial electrode coverage was again achieved by stencils of overhead transparencies on both surfaces. As in the crack initiation experiments two rulers were printed onto the stencils as shown in figure 4.1b to facilitate the parallel alignment of the electrodes. An overview of the different electrode widths prepared is given in table 4.1. Similar to the symmetric geometry a narrow strip of silver - paint was applied along the center of each electrode to ensure complete contact along the electrode length in all stages of cracking. Thin copper wires were glued parallel to the electrode edge on both electrodes using a conducting 2 - component epoxy to connect both sides of the crack. One side of each copper wire extended beyond the specimen edge and served as connection to the high voltage source. Figure 4.1a shows the final configuration (no crack for the displacement measurement). The specimens of 20×20 mm^2 size were fully electroded. Since only a few poled specimens were available some were reused by removing a 5 mm strip containing the electrode by the wire saw. The new electrode was applied to the side opposite to the first electrode which should not be influenced by the previous experiment as it was far away from the original electrode.

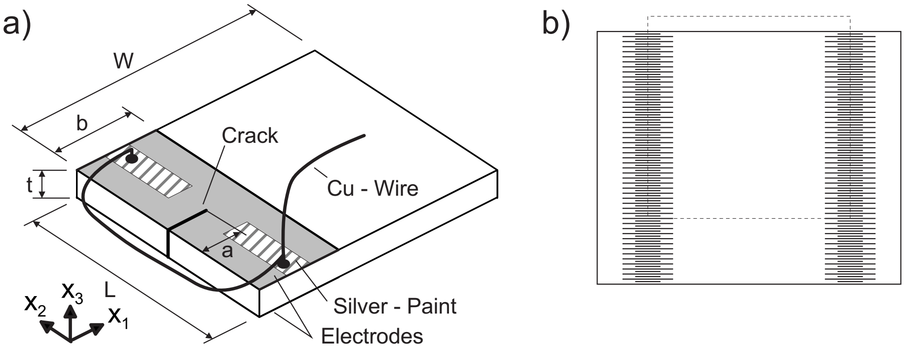

Figure 4.1: a) Schematic overview of the asymmetric geometry with attached electrical contact. b) Stencil used for application of the electrode. The specimen position is marked as dashed line.

The specimen preparation for the crack propagation under electric field measurements was the same as for the displacement measurements but additional steps were needed. A precrack was introduced by placing a Knoop - indent onto the front specimen face. The specimen was clamped in upright position by a high - precision wrench and the indent was placed using a load between 30 N and 50 N for 10 s depending on the desired crack length. Finally, the elastic - plastic contact zone with the attendant residual stress zone was sanded away using alumina paper. A sharp precrack extending from the top to the bottom electrode is obtained.

4.1.2 Poling

The specimens of the batch S5 had to be poled parallel to one of the 40 mm sides after polishing. As the specimens were only 0.5 mm thick they were poled in groups of three. Silicone oil with a molecular weight of 35 was applied between the specimens with a paper tissue. Without the oil air would be left between the plates and would lead to arcing at high electric fields. The stacks were placed between two 8 mm thick glass plates which were mounted by four screws of high-density polyamide. Finally electrodes of conducting 2 - component - epoxy were applied on the top and bottom face of each stack. Silver paint could not be used because it's viscosity is too low and capillary forces would lead to penetration of the paint between the plates yielding arcing during poling. The stack as prepared for poling is shown in figure 4.2.

The poling was done with the high-voltage equipment and under the conditions used previously (see section 3.1.2), except that a new fixture to mount the stacks in the poling frame was built. A field of 1.5 E_C (equivalent to 60 kV) was applied at a slow manually controlled ramp. Initially it was tried to use a field of 1.8 E_C (72 kV), but the setup prohibited the use of such voltages as all specimens cracked (figure 4.2c) and the setup was short-circuited. After the poling the electrodes were sanded away with alumina paper before the glass fixture was unscrewed and the specimens carefully separated.

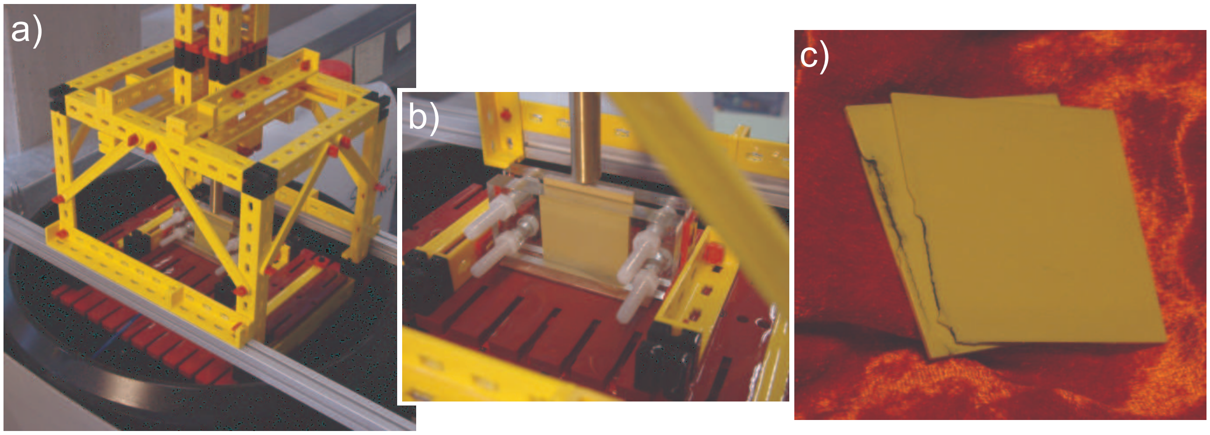

Figure 4.2: b) Specimen fixture for poling specimens of 40 × 40 mm^2 size. a) The fixture is mounted in the frame used for poling CT-specimens. c) Specimen stack after arcing at 72 kV.

4.1.3 Displacement Measurement

The incompatible strains needed for the fracture mechanical analysis cannot be directly measured, but can be computed from displacements. Therefore, displacements were measured parallel to the electrode edge (x_2).

A linear variable displacement transducer (LVDT) with a very thin alumina tip was used as shown in figure 4.3. The tips of the LVDT and the ground fixture were very carefully placed 0.5 mm from the specimen edge on the side specimen faces. The weight of the specimen was sustained on the other side by a plasticine sphere. Silicone oil with a molecular weight of 1000 was applied to the electrodes for electrical insulation. A field of 2 kV/mm (approx. 2 E_C) was then applied at a rate of 12.5 V/(mm·s). The data were logged at a rate of 50 points per second and smoothed over 50 points. Specimens with polarization parallel and perpendicular to the electrode edge as well as unpoled specimens were prepared. Two of each were measured.

A second set of displacement measurements was performed with fully electroded specimens of 20×20 mm^2. The copper - wires were attached in the center of each electrode while the LVDT tips were mounted on the center of the side surfaces and the applied electric field was increased up to 4 kV/mm. In order to prevent arcing at these high fields the specimens were placed in a cup filled with Flourinert 77. The field ramp and the data logging was done with the same rate as the first measurement set. Displacements were measured parallel and perpendicular to the polarization direction on poled specimens and on unpoled specimens. Again, two of each were measured.

4.1.4 Crack Propagation Measurement

The crack propagation under electric field was the main experimental part of this investigation. Two results were to be obtained, which are derived from the same measurement such that a

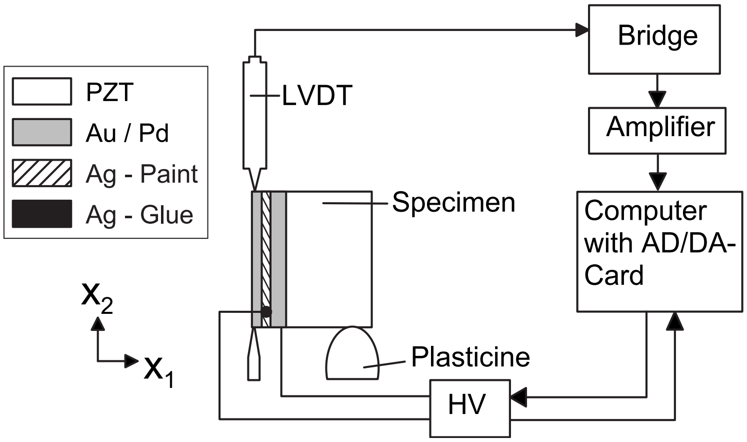

Figure 4.3: Experimental set-up to measure the displacement hysteresis loop.

quantitative description of each crack is available. First, the crack path as function of the electrode width as well as the polarization direction is of importance. In the second evaluation step the crack length as function of the applied electric field and the regions of stable and unstable crack growth are to be obtained.

The precracked specimens were placed in the holding fixture described in section 2.1.4 filled with Flourinert 77 for electrical insulation. The fixture was mounted onto the coordinate stage of the optical microscope (see figure 4.4) and the unipolar high - voltage source was connected to the specimen. A computer with an AD/DA - card was used to control the HV - source.

In the measuring cycle the voltage applied to the specimen was increased by steps of 68 V/mm at a rate of 12.5 V/(mm·s). After waiting for approx. 30 s the crack - tip was targeted with the crosshairs in the eye pieces of the optical microscope and the coordinates were transferred to a custom designed CAD - type software (see appendix B.3). The applied voltage was recorded by a text mark with the applied electric field set at the given coordinates each time the electric field was increased. The waiting time was inserted to let the crack grow subcritically to a very low velocity and therefore maintain uniform conditions for all data points. The increment - measurement - cycle was repeated until no further crack growth was observed. Table 4.1 gives an overview of all the investigated specimens with their exact geometry.

In order to determine the crack mode both fracture surfaces were investigated in the SEM (XL 30 FEG, Philips).

The crack path is directly accessible from the raw data acquired during the measurement by simply reading the coordinates of the data points. In a second step the crack length as function of the electric field was calculated. The length was calculated by taking the first data point as origin and accumulating the geometrical distance to each successive data point. The

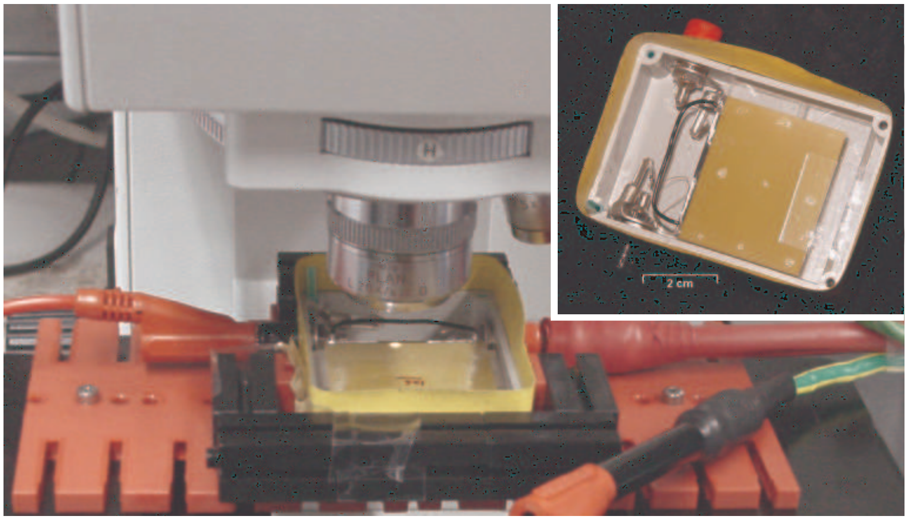

Figure 4.4: Specimen fixture for the crack growth measurement with specimen (insert) mounted on the coordinate desk of the optical microscope.

corresponding electric field was calculated from the voltages stored in the text marks set during the experiment.

4.2 Experimental Results

4.2.1 Measured Displacements

As the displacements were all measured in the direction of shrinkage, the terms “maximum” and “minimum” displacements will always refer to the absolute value thereof.

The measured transverse displacements in the unpoled material for the different geometries are shown in figure 4.5. Beneath the electrode edges in the specimen, electric field singularities occur which give rise to high localized stresses and cracking (small cracks) as discussed in 2.2.3. It is assumed that these small cracks do not essentially affect the measured global displacements and the global field distributions. Therefore, they are not considered in the measurements and in the theoretical analysis (section 4.3). At a field of 1.8 - 1.9 kV/mm one of the many cracks formed at the internal electrode edge grew unstable to the external electrode edge (as indicated in figure 4.5). As the electroded side of the specimen is now divided the displacements on the outer sides where the LVDTs are mounted are reduced. In the fully covered specimens no cracking was observed and therefore the displacements could be measured up to the maximum field of 4 kV/mm. The maximum displacement before the crack appeared in the partially electroded specimens is about -30.6±2.6 µm. At the maximum electric field a displacement of -49.1±1.1 µm was obtained from the fully electroded specimens. The coercive field as defined by the inflexion point is 0.9 kV/mm for the partial and fully electroded specimens. This is in good agreement with the findings of the symmetric geometry in which E_C did not depend on the electrode coverage for specimens with a thickness of 0.5 mm.

In case of the specimens poled parallel to the electrode (figure 4.6) the achievable transverse displacements are much higher. The maximum displacement for the partially covered specimens is -40.7±1.1 µm at an electric field of 1.5 - 1.7 kV/mm at which one crack separated the electrode as in the unpoled specimens. Since the strain is higher than in the unpoled specimens a lower electric field is needed to achieve the same level of tensile stresses and cracking initiates earlier. As in the unpoled specimens no cracks are formed in the fully covered specimens and the measurement could be completed leading to a maximum displacement of -77.9±5.1 µm. The large variation can be attributed to the fact that the specimens might not be cut exactly perpendicular to the polarization direction. Less displacement is obtained if the polarization is not perpendicular to the measurement axis. A coercive field of 0.9 kV/mm is observed and as in the unpoled specimens the electrode coverage did not alter E_C.

With a maximum displacement of the fully covered plates of -35.6±1.7 µm the perpendicular poled specimens (figure 4.7) showed the smallest displacements of all. This is expected as the domain switching from x_1 to x_3 does not yield any strain in x_2. But as not all domains were

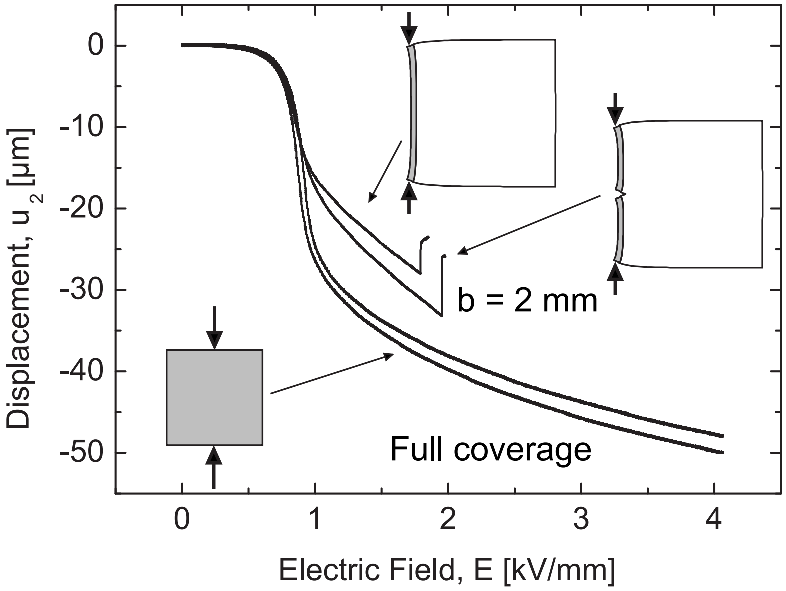

Figure 4.5: Displacements of unpoled specimens. The inserts show the deformations of the specimens during the measurement as calculated by a linear piezoelectric finite element analysis. Arrows mark the position of the LVDT-tips.

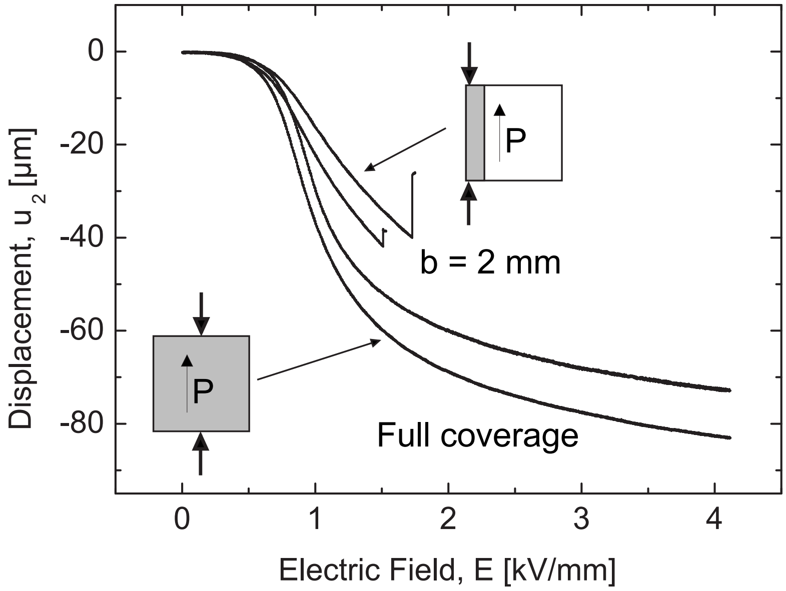

Figure 4.6: Displacements of specimens poled parallel to the electrode. The placement of the LVDT-tips is the same as in the unpoled case. The polarization direction is indicated.

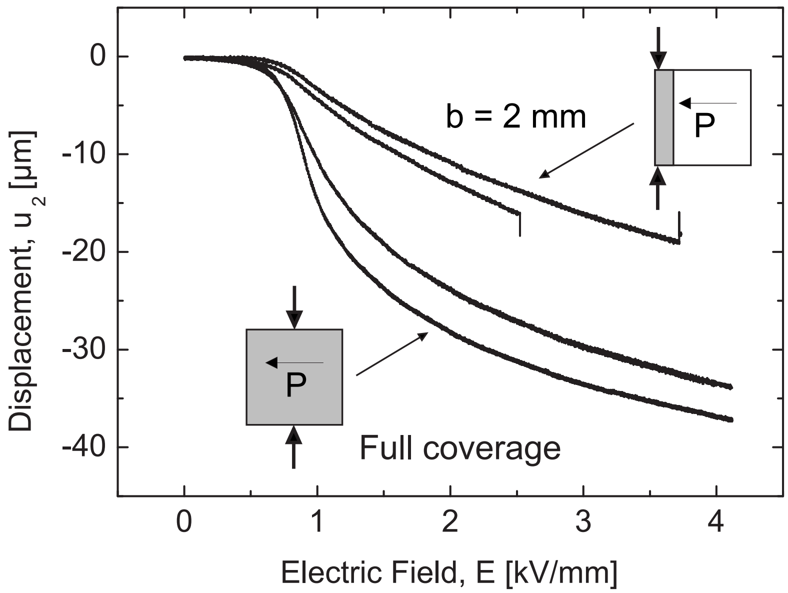

Figure 4.7: Displacements of specimens poled perpendicular to the electrode. The placement of the LVDT-tips is the same as in the unpoled case. The polarization direction is indicated.

oriented in the first poling some strain is still achieved. The variation is much smaller than in the parallel poled specimens as a tilt of the measurement axis from the polar axis is less significant. With a coercive field of 0.9 kV/mm no influence of the polarization state on the coercive field could be measured. The partially electroded specimens achieved a maximum displacement of -14.90±1.2 µm at an electric field of 2.5 kV/mm. In one specimen no crack initiated up to a field of 3.7 kV/mm at which a strain of -18.98 µm was achieved. The low strains induce only a low stress and therefore the electric field at which the cracking starts is much higher than in the other states.

4.2.2 Crack Propagation Measurement

4.2.2.1 Crack Shapes

Two different crack shapes can be identified. A straight crack propagating perpendicular to the electrode edge and a curved crack starting perpendicular to the electrode edge and turning parallel to the electrode edge. The straight crack is obtained in the unpoled specimens with an electrode width of 1 mm and in all specimens poled perpendicular to the electrode edge. Specimens poled parallel to the electrode edge and the unpoled specimens with $b = 2$ mm produced a curved crack. Figure 4.8a provides an overview over all investigated geometries. The secondary cracks emerging from the electrode edges are not shown.

Within each geometry the shape of the cracks can be very precisely reproduced as it is

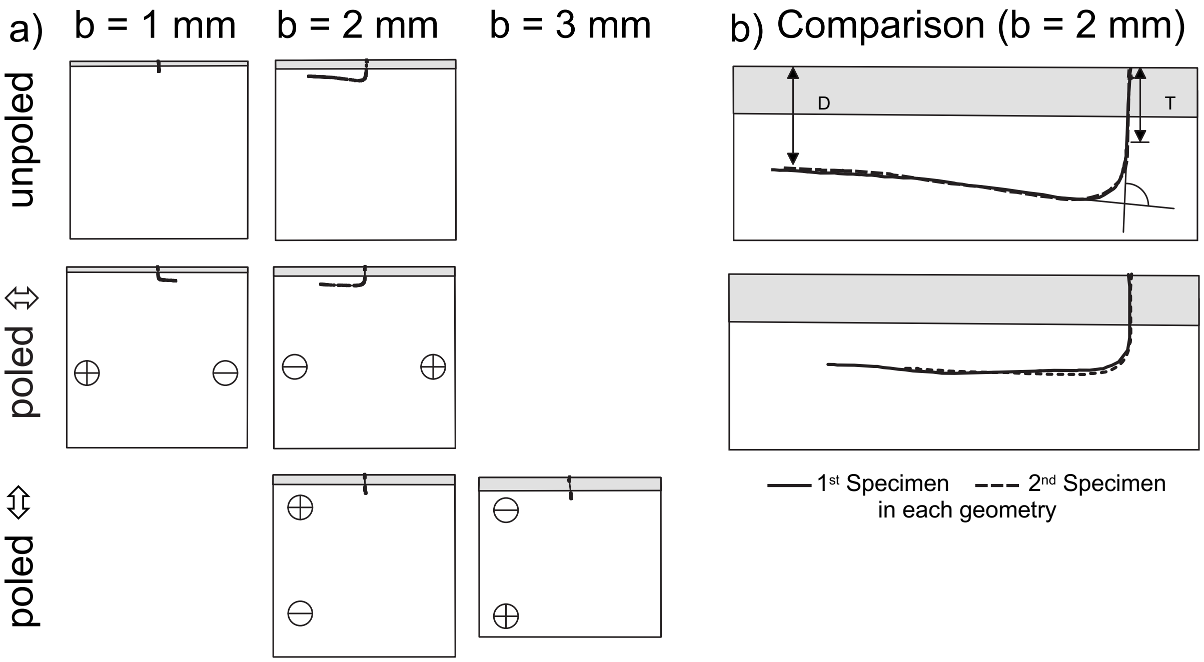

Figure 4.8: a) End crack shapes of all investigated geometries. The true crack, sample, and electrode geometries of selected representative specimens are shown. A geometry of 40 × 40 mm^2 (40 × 35 mm^2) is used. The polarization is shown. b) Crack shapes for $b = 2$ mm in unpoled and specimens poled parallel to the electrode are compared. The different specimens of each geometry are marked by different line styles. The characteristic values of a deflected crack are outlined.

shown for the deflected cracks with an electrode width of 2 mm in figure 4.8b (Please note that the two cracks in each geometry are marked by different line styles). Variations of the shape can be mostly attributed to secondary cracks interacting with the main crack. The shape of the deflected cracks differ from the unpoled to the poled specimens. In the unpoled specimens (figure 4.9) the first straight section of the crack λ_T is about 3.2 mm long followed by a 98° turn from the straight path of the crack. The crack then approaches the electrode as it grows turning slightly parallel to the electrode and reaches a final distance from the specimen edge, the deflection depth λ_D, of about 3.6 mm. The initial straight section of the cracks in the poled specimen (figure 4.10) with an electrode width of 2 mm is about 2.8 mm and therefore only somewhat longer than the electrode itself. After a turn of about 91° the crack maintains a distance from the edge of approx. 3.8 mm deviating much less from a straight line than in the unpoled specimens. The distance from the specimen edges in the unpoled specimen is initially larger than in parallel poled specimen, but decreases rapidly and becomes smaller than in the parallel state after a horizontal growth of about 6 mm. The corresponding values for the poled specimen with $b = 1$ mm as well as the other specimens are listed in table 4.2.

The direction of the crack deflection could not be correlated to the polarization direction. Due to the finite size of the specimen the stresses are higher in the center and therefore a crack can dissipate more energy turning towards the center. The method used to initiate the starter

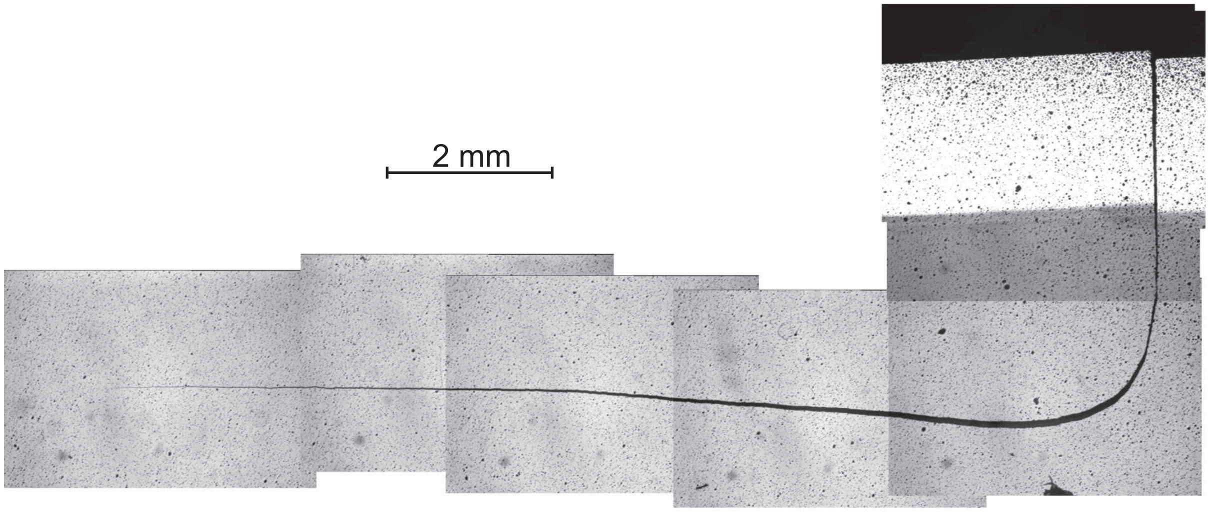

Figure 4.9: Assembled photograph of a crack in an unpoled specimen with an electrode width of 2 mm at the end of the experiment.

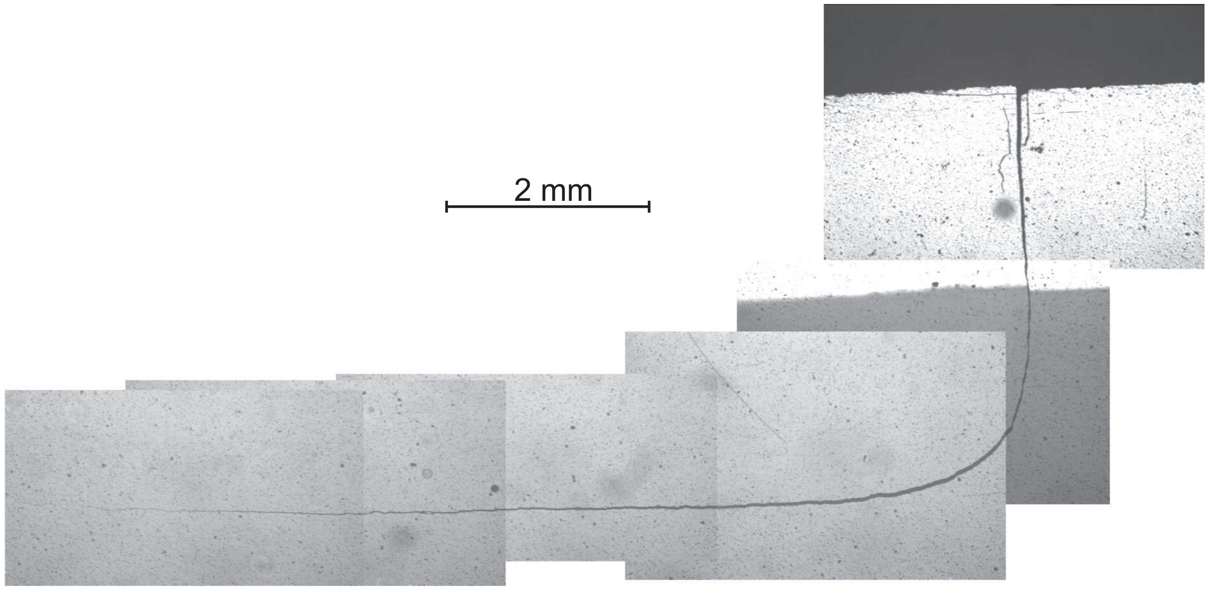

Figure 4.10: Assembled photograph of a crack in a parallel poled specimen with an electrode width of 2 mm at the end of the experiment.

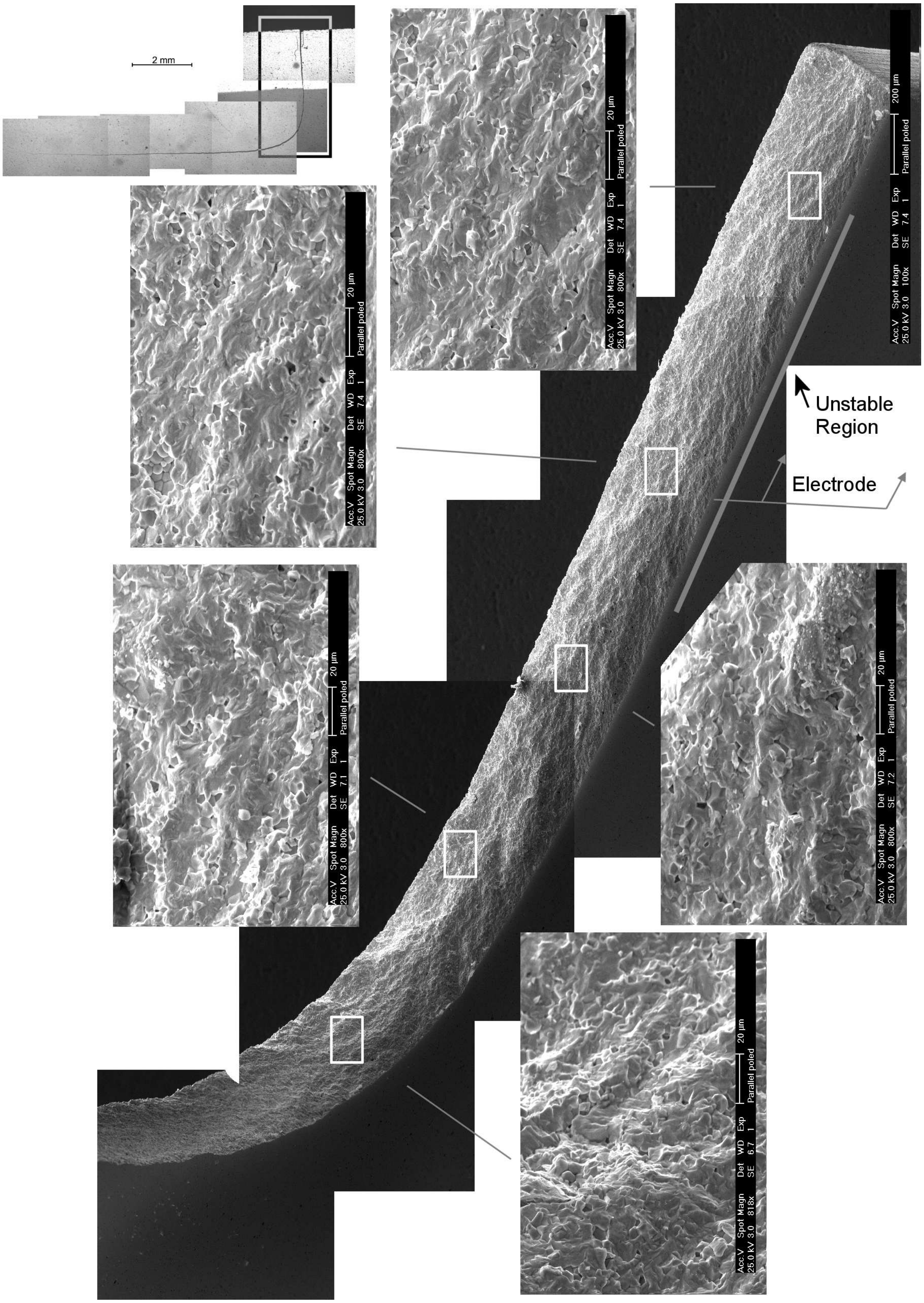

Figure 4.11: Assembled photograph of the surface of the initial straight crack in a parallel poled specimen with an electrode width of 2 mm. The electrode edge and the first region of unstable crack growth are outlined.

crack does not guarantee that the crack is placed exactly on the symmetry line. Furthermore, the initial crack by the Knoop-indent usually grows somewhat tilted. The initial asymmetry finally determines the crack growth direction. Secondary cracks always turn towards the center of the specimen.

An assembled image of the crack surface of the parallel poled specimen with $b = 2$ mm is shown in figure 4.11 along with details along the crack path. Only the first straight part is shown. All other crack surfaces look like the one shown. The crack grew transgranular at all stages of crack propagation. Different areas, such as electrode area or stable and unstable crack propagation areas, could not be distinguished. Specimens of different polarization states could also not be distinguished.

Electrode widths of about 1 mm proved more susceptible to large electrode edge cracks forming more secondary cracks than wider electrodes especially in the parallel poled case. This is in good agreement with the measurements in the symmetric geometry in which electrodes wider than 2 mm did not show large electrode edge cracks at all (see section 2.2.3).

4.2.2.2 Crack Length as a Function of Electric Field

The two different crack shapes described previously yield two different crack growth behaviors. In case of the straight crack two regions of stable and one of unstable crack growth are observed. The initial behavior of the deflected crack is the same as in the straight case, because the crack is still straight. After the deflection an additional unstable and stable region are observed. The resulting crack length - electric field curve is schematically shown in figure 4.12 along with the characteristic values for the crack length and the electric field. An overview over the actual values for all investigated specimens is provided in table 4.2 and the measured crack length curves are shown in figures 4.13 - 4.18. With regard to the modelling the input quantity (electric field) is plotted as the ordinate and the resulting quantity (crack length) as the abscissa.

The results of the measurements will be described by the characteristic values rather than by specimen. A short discussion follows where it is appropriate. The starter crack length a_0 varies from 0.31 - 0.60 mm for all specimens. It turned out that it was difficult to obtain a uniform crack length in every experiment as the final length depends crucially on the exact placement of the Knoop-indenter and the polarization state. Nevertheless, in most cases a crack length of about 0.46 mm could be achieved. The electric field E_0 at which the first crack growth is observed shows a large scatter from 0.15 - 0.65 kV/mm. A major problem with this value is related to the measurement of the initial crack length. It is possible that the initial crack length is underestimated because of the low magnification of 200×. By slightly increasing the voltage the crack reopens under the influence of the low tensile stresses which is difficult to distinguish from true crack growth.

In specimens exhibiting crack deflection the start of the first unstable region a_1 can be clearly identified. The first stable region is characterized by an almost linear relationship between crack

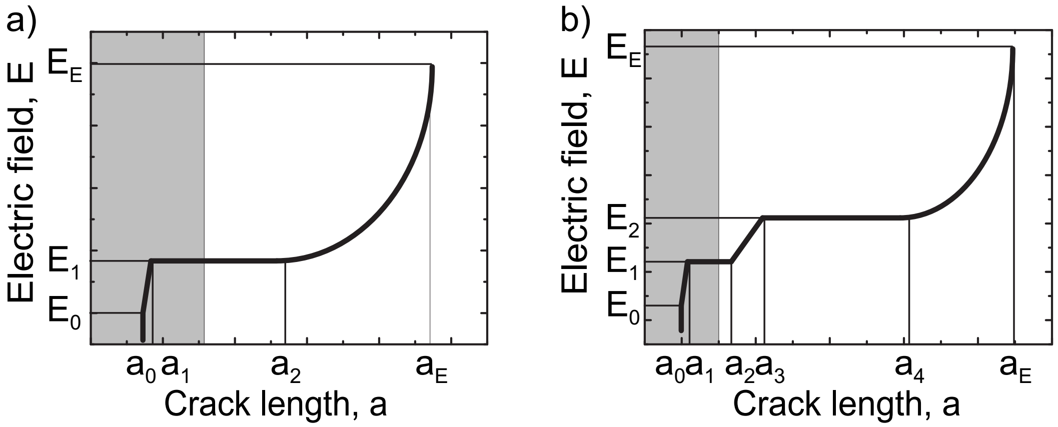

Figure 4.12: Schematic overview of the crack length as function of the electric field for the a) straight and b) deflected crack along with the characteristic values.

Table 4.2: Characteristic value for the electrically driven crack growth as shown in 4.12. λ_T designates the length at which the crack starts deflecting and φ the angle by which it deflects. The final distance from the specimen edge is termed λ_D.

Property	Value for each specimen							
Polarization[a]	—— unpoled ——			—— parallel ——			perpendicular	
b [mm]	1.07	1.95	1.87	1.16	2.06	2.03	2.12	2.89[b]
t [mm]	0.44	0.51	0.31	0.46	0.46	0.47	0.46	0.46
a_0 [mm]	0.36	0.31	0.56	0.49	0.52	0.60	0.49	0.59
E_0 [kV/mm]	0.38	0.13	0.65	0.44	0.15	0.15	0.44	0.44
a_1 [mm]	0.49	0.52	0.59	0.51	0.57	0.65	0.77	0.89
E_1 [kV/mm]	0.85	1.00	0.97	0.59	0.74	0.52	1.33	1.48
a_2 [mm]	1.28	3.05	3.25	1.44	2.62	2.51	2.71	3.61
a_3 [mm]	—	4.37	4.59	2.47	6.64	5.85	—	—
E_2 [kV/mm]	—	1.67	2.13	1.04	1.11	0.89	—	—
a_4 [mm]	—	11.87	12.41	3.98	11.86	9.30	—	—
a_E [mm]	2.37	16.89	16.33	6.36	16.39	13.22	4.15	4.74
E_E [kV/mm]	3.94	3.29	4.19	1.78	2.22	1.26	4.25	2.52
λ_T [mm]	—	3.19	3.17	2.23	2.88	2.67	—	—
λ_D [mm]	—	3.55	3.55	2.93	3.67	3.84	—	—
φ [°]	—	98	98	93	91	91	—	—

[a] relative to the electrode edge

[b] specimen with $L = 40$ mm and $W = 35$ mm

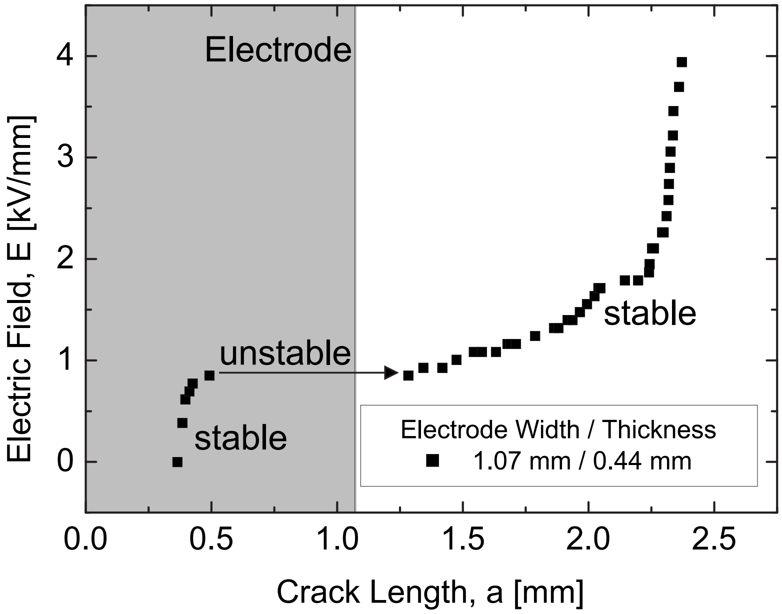

Figure 4.13: Crack length as a function of the electric field for an unpoled specimen with $b = 1$ mm.

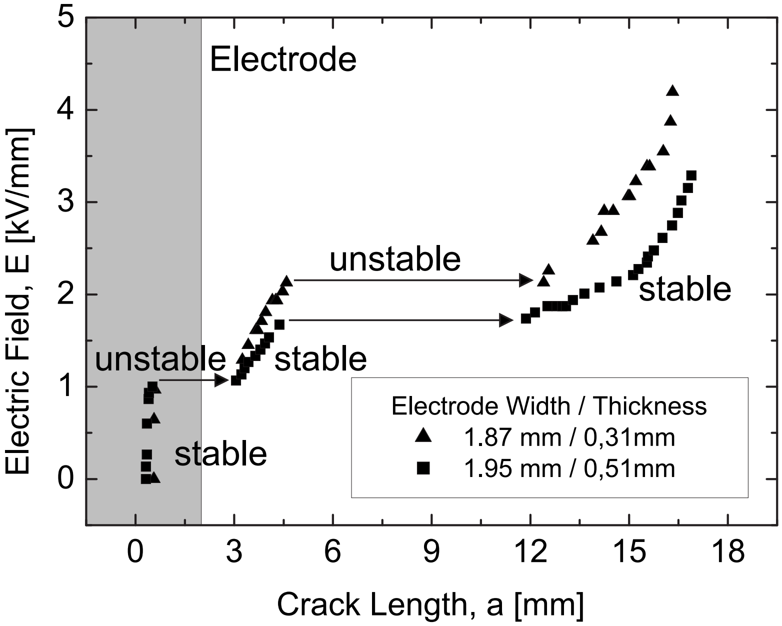

Figure 4.14: Crack length as a function of the electric field for an unpoled specimen with $b = 2$ mm.

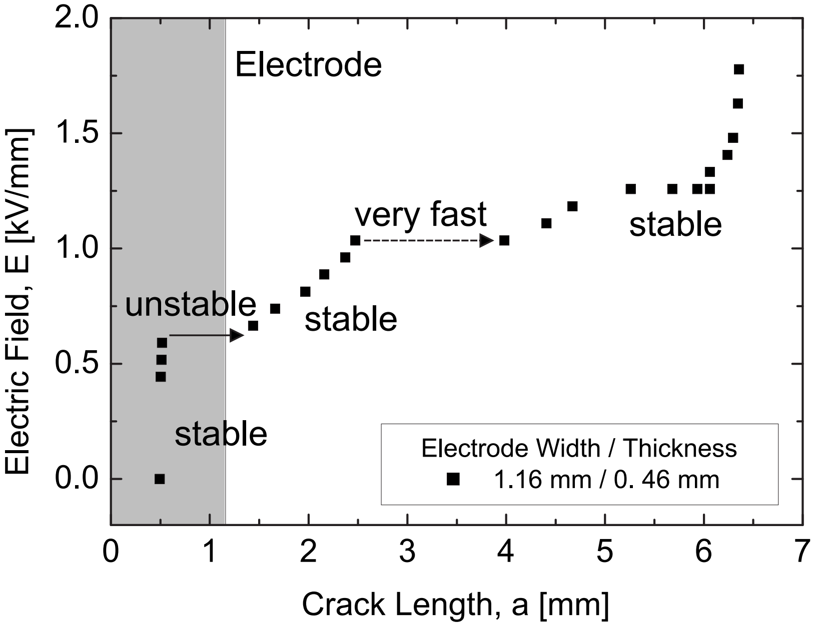

Figure 4.15: Crack length as a function of the electric field for a specimen poled parallel to the electrode with $b = 1$ mm.

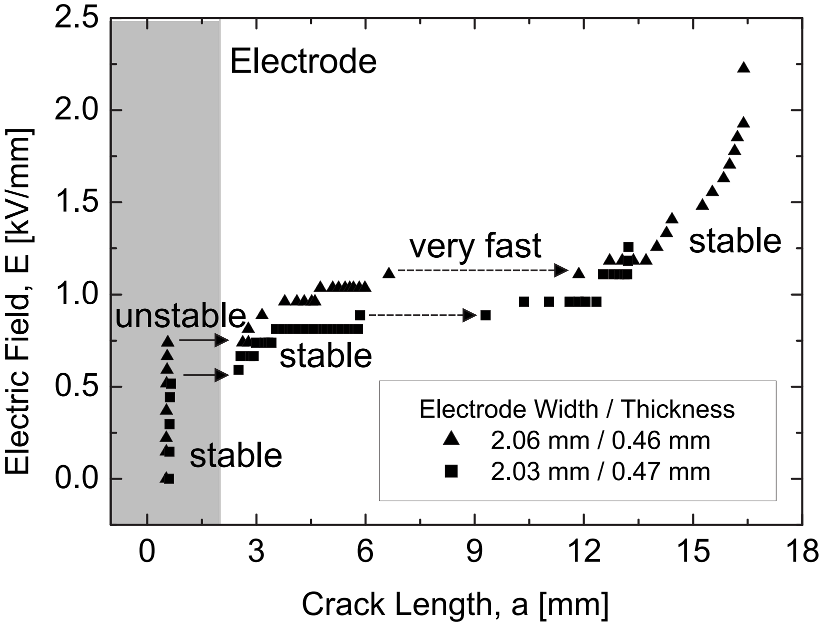

Figure 4.16: Crack length as a function of the electric field for a specimen poled parallel to the electrode with $b = 2$ mm.

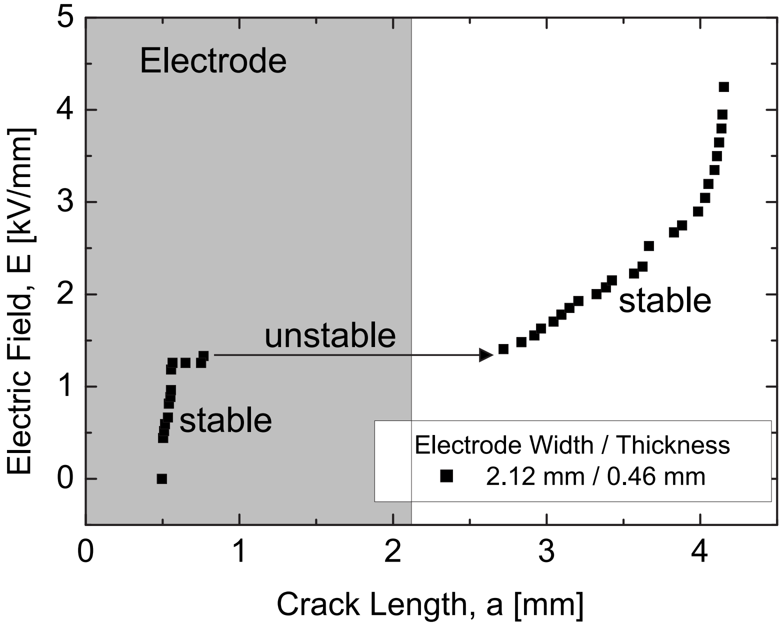

Figure 4.17: Crack length as a function of the electric field for a specimen poled perpendicular to the electrode with $b = 2$ mm.

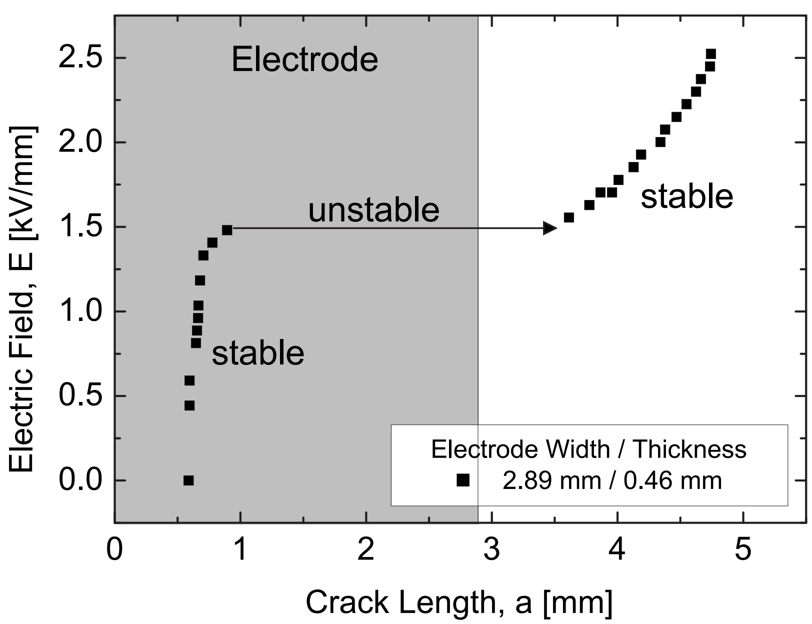

Figure 4.18: Crack length as a function of the electric field for a specimen poled perpendicular to the electrode with $b = 3$ mm.

length and electric field and the unstable crack growth sets in suddenly. In the specimens without crack deflection the above relationship is only initially linear. At higher fields the same electric field increment yields larger crack growth. The stable/unstable transition in those specimens is preceded by a small region of subcritical crack growth with increasing velocity as the crack approaches the critical length. Special effort was made to mark the transition point itself, but a small error can not be avoided.

Within a polarization state the length a_1 increases with wider electrodes. Comparing the different polarization states for each electrode width shows that the shortest lengths can be observed in the unpoled state. In the parallel poled specimens a_1 is only slightly increased compared to the unpoled state. The perpendicular poled material yields a significantly larger a_1 than the unpoled material.

The electric field of the first unstable region E_1 can be clearly identified in all experiments, with lowest fields required in the parallel poled specimens, followed by the unpoled and highest fields are found in the perpendicular poled samples. As the same stress is required in all specimens, the same strain has to be achieved. Yet, the strain depends on the previous polarization state (see section 4.2.1) and therefore E_1 varies with the polarization state.

The end of the first unstable region a_2 is always followed by a region of stable crack growth. It is therefore afflicted with an uncertainty of measurement. The final crack stop was taken as a_2. Similar to the start, the stop length increases with the electrode width. For an electrode width of 1 mm a_2 in the unpoled specimen is slightly shorter than in the parallel poled specimens. The ranking for $b = 2$ mm is clear with the unpoled yielding the largest crack lengths and the parallel poled states the shortest.

The values a_3, E_2 and a_4 are only obtained for the deflected cracks. A comparison of different electrode widths can only be made in case of the parallel poled specimens. In those, both the starting a_3 and the final crack length a_4 of the second unstable region are greatly increased with larger electrodes. While the start length for the unpoled specimens is smaller than for the poled ones, the cracks have about the same final lengths which might be due to the stress relieve by the specimen border. The electric field at the second unstable region does not vary significantly by variation of the electrode width, but is much higher in the unpoled state than in the parallel poled state. In the parallel poled specimens the second unstable crack growth region is not really unstable but with velocities of several millimeters per second very fast.

The final crack lengths and electric fields at the end of the experiments are marked by a_E and E_E. Both values are to be read carefully. At an electric field about 1.2-1.7 times E_1 one of the many electrode edge cracks surpassed the critical length to unstably grow to the specimen edge and forms a secondary crack. Those cracks can become quite large (several millimeters) and interact with the main crack. That can usually be seen in a kink in the crack length vs. electric field data as e.g. in figure 4.13 at a crack length of about 2.2 mm. In the parallel poled specimen with an electrode width of 2.03 mm the secondary cracks led to an early stop of the experiment. Otherwise maximum crack lengths of about 16-17 mm were observed for all deflected cracks. The final crack length of the straight cracks increased with increasing electrode width and were larger in the parallel poled specimens than in the unpoled ones. Perpendicular poled specimens cannot be compared due to the different electrode widths. The final electric field at which no further crack growth of the main crack was observed, was about the same in the unpoled and perpendicular poled specimens (approx. 4 kV/mm), both much higher than in the parallel poled specimens (approx. 2 kV/mm).

As seen in figure 4.8 the crack shapes are well reproduced as well as the transition lengths of the first unstable region a_1 and a_2. The transition lengths of the second unstable region a_3 and a_4 are less well defined, especially in the parallel poled specimens. Uncertainty in measuring the end crack length is one of the reasons. The electric field required for a certain crack length varies by up to approx. 20% between two measurements on one geometry. The discrepancy starts in the first stable region and becomes larger in the second stable region. Small variations in the specimen and electrode geometry can contribute to that effect.

4.3 Quantitative Fracture Mechanical Analysis[1]

Due to the complexity of the analysis the full quantitative fracture mechanical analysis is only performed for one unpoled geometry with an electrode width of $b = 2$ mm which showed a curved crack. A detailed numerical analysis of the crack propagation and a comparison of numerical results with experiments is provided. The discussion of the straight crack in an unpoled specimen with $b = 1$ mm is a direct application of the principles given in the introduction (section 1.2.2).

4.3.1 Finite Element Model

The basis of this analysis is again linear-elastic fracture mechanics and criteria (1.10). Due to the condition $K_{IV} = 0$, the effect of electric field is equivalent to a criterion of thermal expansion in the electrode region.

A numerical thermomechanical analysis is carried out with the finite element method for the finite specimen. A plane stress model of isoparametrical biquadratic elements with quarter-point elements in the vicinity of the crack tip is used in the FE-code ANSYS [76]. The material in the electrode region is considered to be completely poled and transversely isotropic (Young's modulus $Y_{11} = Y_{22} = 59.5$ GPa and Poisson ratio $\nu_{12} = 0.34$). The material in the inactive zone is isotropic ($Y_{iso} = 66.5$ GPa, $\nu = 0.37$). The mismatch zone between the active and the inactive zone is estimated as half the specimen thickness and is not considered in our analysis because of the very thin plate geometry.

The thermoelastic stress-free strains as driving force for crack propagation are the incompatible strains. They consist of ferroelectric, ferroelastic, and piezoelectric strain and can also

---

[1] Cooperation with Dr. H.-A. Bahr, Dr. V.-B. Pham, and Prof. Balke, Dresden University of Technology [26].

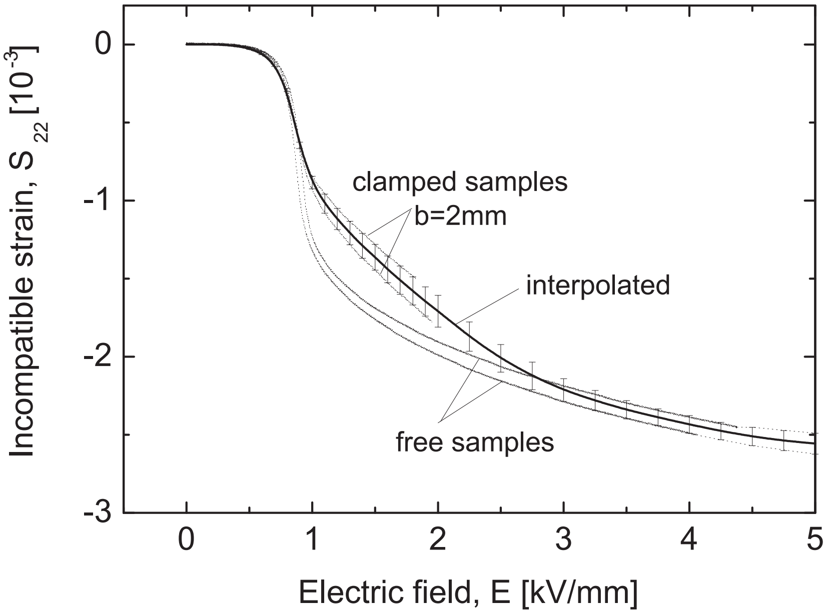

Figure 4.19: Calculated and interpolated incompatible strains depending on the electric field as computed from displacement measurements for an unpoled specimen.

be understood as the difference between total and elastic strain. These quantities are calculated from the measured displacements in figure 4.5. The proportionality factor between the incompatible strains and the displacements has been obtained by means of a FE calculation. It turned out that this relationship is indeed linear and constant over a wide range of the electric field and that the directions x_1 and x_2 are almost entirely linearly independent. The latter is important as only the displacements in x_2 had to be measured to calculate the strain S_{22}. Some details are given in appendix A. As mentioned in section 4.2.1, these displacements could be measured only up to $E = 1.9$ kV/mm in the clamped specimens. For very high electric fields ($E > 3$ kV/mm), they are assumed to be the same as in a free completely poled sample and for electric fields between 1.9 kV/mm and 3 kV/mm, an interpolation between these two curves (see figure 4.19) is applied. In this figure the calculated incompatible strain vs. electric field is plotted including scatter due to the variation of the two displacement measurements (figure 4.5).

The incompatible strains are assumed to be homogeneous, even if a crack passes the electrode and unloads the adjacent region. This unloading zone is estimated to be comparable with the electrode width b which is much smaller than L. In finite sized specimens the stresses in the electrodes are not entirely homogeneous (figure 4.20). Next to the slightly inhomogeneous stress in the electrode area, the stress distribution in the finite samples without crack shows two more differences in comparison to the semi-infinite plate: the magnitude of the tensile stresses decreases and the compressive stresses next to the electrode increase with increasing electrode

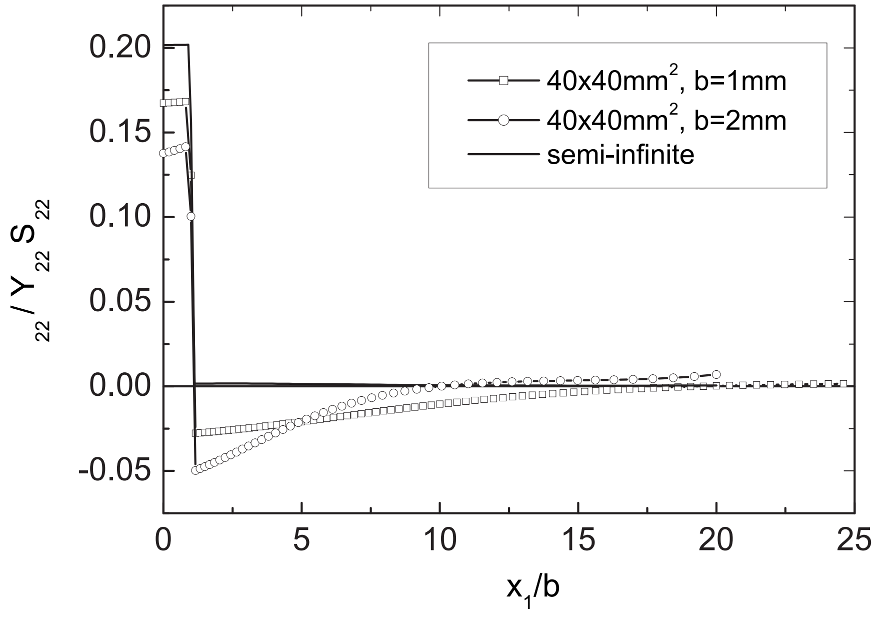

Figure 4.20: Stresses due to strain incompatibility for a real specimen as compared to an idealized semi-infinite specimen without crack.

coverage b/W. In figure 4.20, the stress is normalized by the product of the elastic modulus Y_{22} and the arbitrarily chosen stress-free strain S_{22} in x_2 - direction. In plane stress the results do not depend on Poisson's ratio.

For the crack simulation the crack was modelled as a continuous set of splines by an iteration procedure described later such that no kink is introduced anywhere. The stress intensity factors K_I and K_{II} for a reference load are determined by linear extrapolation of the stresses ahead of the crack tip for $r \to 0$ according to linear fracture mechanics [77]:

$$K_I = \lim_{r \to 0} \sigma_{22} \sqrt{2\pi r} \qquad \text{and} \qquad K_{II} = \lim_{r \to 0} \sigma_{21} \sqrt{2\pi r} \tag{4.1}$$

The stress intensity factors for the actual electrically applied load are calculated from the reference case by linear scaling as it is shown in appendix A.

4.3.2 Stress Intensity Factor for a Straight Crack

In contrast to the semi-infinite specimen, the stress distribution yields significantly smaller K_I for a straight crack in a finite specimen, particularly next to the electrode as consequence of the compressive stresses in this zone (figure 4.21). Another difference to figure 1.8 and 1.9 is the asymptotic behavior of the stress intensity factor for $a/b \to 1$ because of different materials on both sides (Zak-Williams singularity for $a/b = 1$, [27] p.131). However, this latter behavior has no significant consequence for crack propagation.

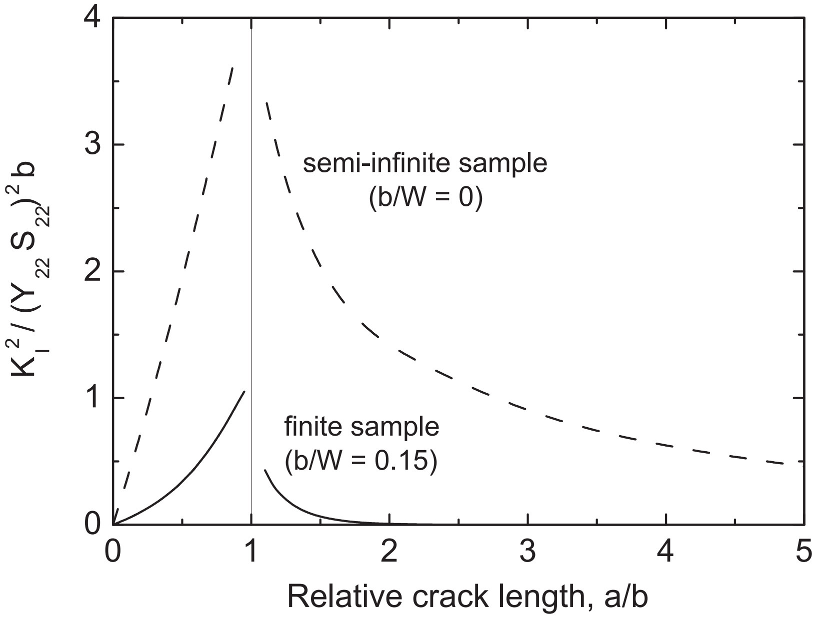

Figure 4.21: Squared normalized mode I stress intensity factor as calculated by FEM along the crack path for the straight crack in a semi-infinite specimen and in a finite specimen.

As a result of these effects in a finite body, the straight crack propagation with three stages is identical as discussed in section 1.2.2, but shifted towards higher electric fields. More interesting is the curved crack propagation which is analyzed in the next section.

4.3.3 Curved Crack Shape Simulation

The path of a curved non-kinked crack can be calculated from the local symmetry condition $K_{II} = 0$ in equation 1.10. Several numerical methods have been proposed for crack path determination using FEM:
a) methods based on the crack path prediction as incremental straight crack extension with a direction angle change calculated from the current crack closure integrals [78, 79] or from the current stress intensity factor - ratio K_{II}/K_I (e.g. [30, 80]).
b) methods based on the crack path prediction as incremental curved extensions [81]. Starting from the first order perturbation solution, the stress intensity factors along a slightly curved crack are solved as analytical terms of arbitrary crack shape parameters and pre-existing crack-tip stress field. The crack path extension results from the crack shape parameters fulfilling the local symmetry condition $K_{II} = 0$. This method requires knowledge of the correction factors representing the effect of stress re-distribution due to crack growth in a finite body. Theilig [82] avoids this by additionally calculating the stress intensity factors for a straight crack extension increment and by comparing them with the stress intensity factors of the curved crack extension

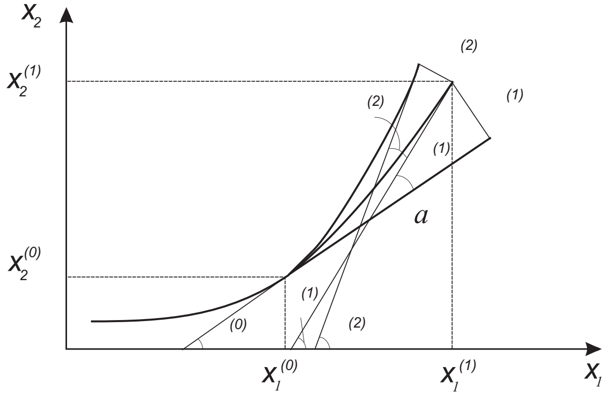

Figure 4.22: Iteration method for incremental simulation of propagation of a curved crack.

increment which fulfils the local symmetry condition. This leads to the curved crack path parameters from the stress intensity factors of the crack with the straight extension.

These predictions provide only good results for extensions of slightly curved cracks due to their derivation from a perturbation solution of first order. Applying these methods to the problem, the simulated crack path always drifts away from the experimental contour, especially in the strongly curved region (figure 4.9), even in the case of very small crack increments. Another disadvantage of these prediction methods lies in the accumulation of errors with progressive increments, so that errors in early increments have decisive implications for the divergence of the crack contour in the subsequent crack propagation. Therefore, an iterative incremental technique for the crack propagation simulation is proposed. Figure 4.22 illustrates the iteration procedure for a crack growth increment Δa.

$$\begin{aligned}
\Delta\lambda^{(i)} &= -\frac{K_{II}^{(i)}}{K_I^{(i)}}\Delta a \\
\Delta\alpha^{(i)} &= -2\frac{K_{II}^{(i)}}{K_I^{(i)}} \\
\alpha^{(i)} &= \alpha^{(i-1)} + \Delta\alpha^{(i)} \\
x_1^{(i)} &= x_1^{(i-1)} - \Delta\lambda^{(i)}\sin\alpha^{(i)} \\
x_2^{(i)} &= x_2^{(i-1)} + \Delta\lambda^{(i)}\cos\alpha^{(i)}
\end{aligned} \tag{4.2}$$

In figure 4.22, the upper index (0) provides the coordinates $x_1^{(0)}$, $x_2^{(0)}$ and tangent angle $\alpha^{(0)}$ at the tip of a pre-existing crack fulfilling the local symmetry condition. Index (i) describes the iteration step (i). The actual simulation is performed as follows: Before the first iteration step (1), the pre-existing crack is extended straight by Δa in the tangential direction $\alpha^{(0)}$ at the crack tip. In the subsequent steps the crack extension is adjusted by quadratic splines. In every step a FE-analysis is performed first to calculate the stress intensity factors $K_I^{(i)}$ and $K_{II}^{(i)}$.

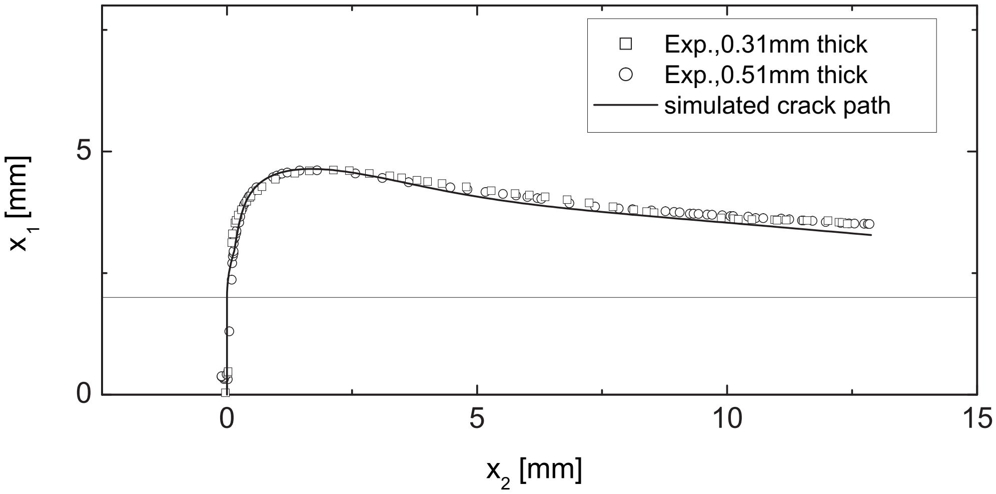

Figure 4.23: Comparison of the experimentally and theoretically determined curved crack paths for an unpoled specimen.

They are used to calculate the corrections $\Delta\lambda^{(i)}$ and $\Delta\alpha^{(i)}$ according to the procedure given in 4.2. The first iteration step is the result of the prediction method [82]. The iteration is ended once the following condition is met:

$$\left|\frac{K_{II}^{(i)}}{K_I^{(i)}}\right| \leq \varepsilon. \tag{4.3}$$

The coordinates $x_1^{(i)}$, $x_2^{(i)}$ and the tangent angle $\alpha^{(i)}$ at the end of the iteration are the starting point $x_1^{(0)}$, $x_2^{(0)}$ and $\alpha^{(0)}$ for the next crack growth increment.

For the simulation ε was chosen as 10^{-3}. In slightly curved pieces of the crack contour only one iteration is necessary for $\Delta a = 0.1$ mm, while in the deflected regime it requires 2 to 3 iterations for $\Delta a = 0.05$ mm. This confirms that the prediction methods alone are not suitable for a strongly curved crack.

The simulated and experimental crack contour almost coincide, even in the very strongly curved region (figure 4.23). The negligible deviation in the second unstable stage and thereafter may be ascribed to dynamic effects which are not considered in this analysis.

4.3.4 Crack Extension

The K_I-curve as a function of crack length in figure 4.24 is utilized as the basis for crack length determination. Comparing with figure 1.8 it is apparent that the second unstable stage and the subsequent stable stage are caused by the minimum of K_I at $a = 4.55$ mm and the following increase and decrease. This is a consequence of the compressive stresses behind the electrode edge (figure 4.20) and boundary effects in the finite sample.

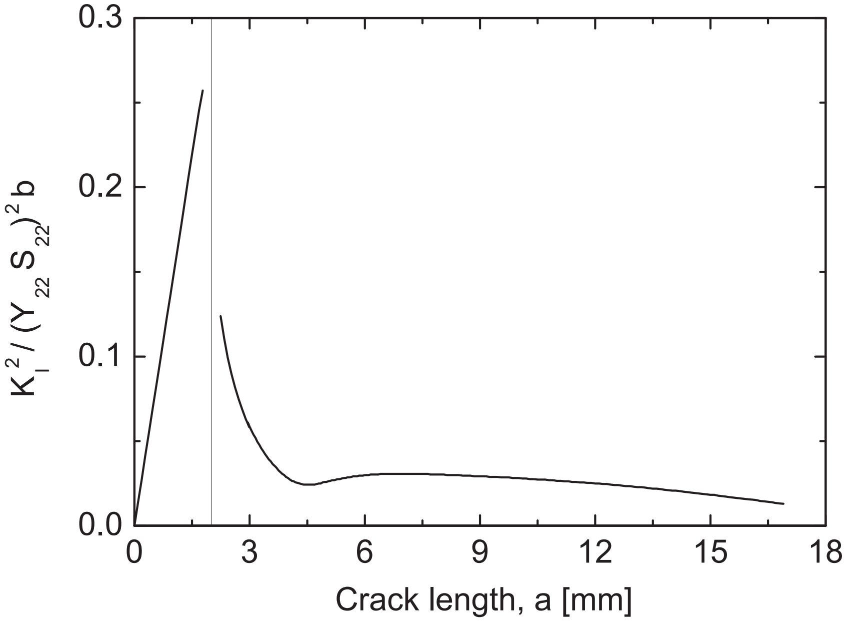

Figure 4.24: Squared normalized mode I stress intensity factor as calculated by FEM along the path for the curved crack in an unpoled specimen.

Crack propagation for curved cracks as function of the electric field E can be discussed by means of K_I - curves. In the upper half of figure 4.25, the curves denoted by E_0 to E_3 are the squared stress intensity factors K_I^2 for a crack of length a under the electric field E_0 to E_3, respectively. The electric field increases with larger index. Dashed and solid arrows describe stable and unstable crack propagation, respectively.

The scenario for the propagation of a deflected crack can now be derived from this diagram as follows: an initial crack a_0 starts at E_0 due to (1.10) $K_I = K_{Ic}$ (corresponding to the starting value of the R - curve for a poled material) and grows stably ($dK_I/da < dK_R/da$) up to E_1 because of a developing process zone. At E_1 the condition $dK_I/da \geq dK_R/da$ is met for the first time and the crack will propagate unstable.

Quantification of the first stage of stable crack propagation would require a set of R-curves for different applied electric fields. As these measurements are not available, the modelling starts at the more interesting first unstable stage by adopting the experimental average values $E_1 =$ 1.0 kV/mm and $a_1 = 0.55$ mm. This unstable stage will end at a_2, where the condition $K_I =$ K_R-plateau (for unpoled material) is met on the downward slope of the E_1-curve. An increase of the electric field leads to a stable crack regime corresponding to the dashed arrows up to E_2, where the minimum of the E_2 - curve at $a_3 = 4.45$ mm is equal to the K_R-plateau (for unpoled material). At this electric field, the crack will jump to $a_4 = 12.45$ mm. It is worth noting that the jump from a_3 to a_4 and the values a_3 and a_4 derived from the K_I-curve above are quite independent of the K_R-plateau value. After this second unstable stage, only stable crack growth

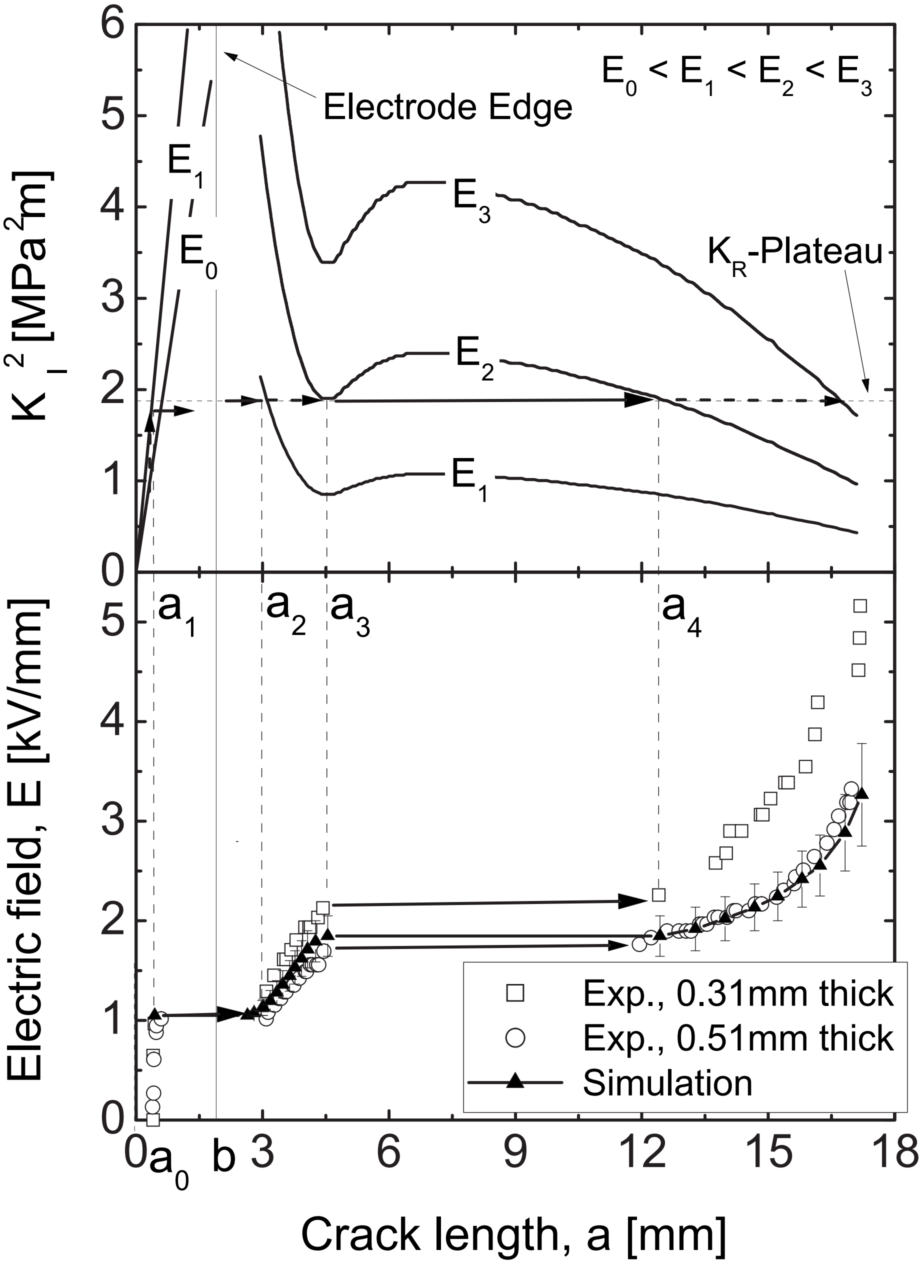

Figure 4.25: Fracture mechanical analysis of the propagation for the curved crack depending on the electrical field. Upper half: Squared mode I stress intensity factor for different electrical fields E_0 - E_3. The regions of stable and unstable crack propagation are indicated by dashed and solid arrows, respectively. Lower half: Comparison of the experimentally measured and theoretically determined crack length depending on the electrical field.

is possible with a further increase of the electric field.

Accordingly the five stable and unstable stages of crack propagation as observed in the experiments are completely reconstructed and are also provided in figure 4.25. The characteristic lengths a_3 and a_4 were computed without the knowledge of the load and the K_R-plateau value.

For the determination of E_2 to E_4 and of the crack length as function of the electric field the K_R-plateau value of the unpoled material (figure 3.4) and the incompatible strains as a function of the electric field are required. The result is shown in the lower half of figure 4.25, where the simulated crack length depending on the electric field is compared with the experiment. With respect to the transitions between stable and unstable stages, the agreement is excellent. The computed crack length as a function of the electric field is exhibiting some variability due to scatter in the incompatible strains (figure 4.19) and the plateau values in the R-curves (figure 3.4). The simulated curve lies closer to the experimental curve with specimen thickness of 0.51 mm, with increasing deviation for higher electric fields. The latter is attributed to two effects. First, the formation of secondary cracks at the electrode edge at higher electric fields. These can unload the main crack, which in turn requires higher strains and therefore higher electric fields for the same crack driving force. Second, as for high electric fields, the stress-free strains represent the lower limit of the incompatible strains in figure 4.19. The effective poling in x_3 - direction is reduced by tensile mechanical stresses σ_{22} and therefore the strains S_{22} are smaller in magnitude than the used strains of a free specimen.

4.4 Discussion

Experiments were described, which allow the controlled study of crack propagation due to strain incompatibility. It represents an electrically driven equivalent to crack propagation under thermal shock conditions [30]. As in thermal shock, propagation of straight cracks and deflected cracks is observed with the expected transition between both modes. Starting with a well defined precrack and using the electric field as a means of providing strain incompatibility affords superior control over crack propagation and detailed observation of incremental crack growth in the optical microscope.

The basic behavior follows the qualitative analysis in section 1.2.2. Crack length differences by electrode width variation are easily explained by figure 1.9. Larger b yields a higher crack driving force and therefore a larger crack. However, the qualitative analysis is not able to explain the crack turning towards the electrode edge in the deflected crack contour and the third additional stable stage for large crack lengths. Those effects can only be described using the real specimen geometry. They are therefore side effects and depend on the geometry.

From the introduction in section 1.2.2 it can be concluded that every crack in every geometry will deflect once it has attained a critical length. An upper limit for that length is the deflection depth λ_D, which is the distance from the specimen edge at which the crack runs parallel to the edge after it has deflected. To achieve that length, K_I has to be greater then K_R along the full path as otherwise the crack would arrest and not attain the critical length or it would not deflect because $K_I < K_R$ in the deflected direction. In an unpoled specimen K_R is isotropic and therefore only K_I determines whether the crack attains the critical length. The applied stress intensity factor, the driving force, is given by the electrode width b and the applied stress σ_{22} respective strain S_{22}. Narrow electrode widths lead to a lower K_I and the crack will arrest before it can deflect.

In poled specimens K_R is not isotropic any more. It is lower if the crack runs perpendicular to the poling direction and higher if it runs parallel thereto (figure 3.5). In consequence, the crack in a specimen poled parallel to the electrode edge should run rather straight than deflect, because a lower K_I is required in that direction. However, K_I also depends on the strain S_{22} which is by a factor 1.6 higher in the poling direction parallel to the electrode edge (figures 4.6 and 4.7) and overcompensates the higher K_R-plateau in the deflected direction. The large strains even compensate the effect of the narrow electrode and thus the crack in a specimen with $b = 1$ mm does also deflect. A second consequence of the high achievable strain is that, compared to an unpoled specimen, a significantly lower electric field is required to obtain the same stress and therefore crack length.

The same argumentation, but in inverse direction, is also valid for the specimens poled perpendicular to the electrode edge. The K_R-plateau would imply a deflected crack, but the low strain prohibits attaining the critical deflection crack length. Even a wider electrode of 3 mm cannot compensate the low strains. Accordingly, a higher electric field is needed to achieve the same level of stress. The ranking of E_1 and E_2 with respect to the polarization state can thus be easily understood.

According to [27] the deflection depth λ_D in a linear elastic case is governed by the elastic mismatch between the active and the inactive material. Increasing stiffness of the inactive part leads to a smaller depth, if the properties of the active strip remain constant. In these experiments the active strip is always poled in x_3 direction once the crack has attained a length critical for deflection. The properties can therefore be assumed to remain the same in all specimens, while they vary in the inactive part according to the polarization state of the specimen. In a poled specimen the modulus parallel to the electrode edge is the critical one [27]. It is 68.0 GPa in an unpoled specimen and $Y_{33}^D = 83.3$ GPa in the parallel poled specimens[2]. Accordingly, the deflection depth of the poled specimens should be smaller than that of the unpoled specimens, which is only observed for the first 6 mm after deflection. First preliminary modelling results for the poled specimens indicate that the piezoelectric effect at the crack tip of a poled specimen which is not present in an unpoled specimen is responsible for this behavior [83]. Additionally the investigated specimens are finite and therefore edge effects have to be considered, which are not included in [27].

---

[2] The values differ from the ones used previously as these are measured by ultrasonic method whereas the others were by bending. This is the only method by which the Young's modulus has been measured for all boundary conditions [72].

Utilization of a ferroelectric material to provide the electrical field generated strain incompatibility also generates some complications. Careful choice of specimen dimensions and measurement procedure reduced the observed complicating issues to small effects as proven in figure 4.23 and 4.25.

The non-homogeneous electric field at the electrode edge is problematic in two ways. An electric field singularity is located under the electrode edge which due to the piezoelectric coupling and ferroelectric switching gives rise to locally increased tensile stresses and leads to the formation of secondary cracks along the electrode edge (see chapter 2). These cracks observed at higher electric fields can relieve the stresses at the main crack which then requires higher strains and higher electric fields for crack propagation. The density of secondary cracks is strongly reduced, if the thinnest feasible specimens are selected. Furthermore, the electric field incorporates a fringing field next to the electrode edge, providing a volume between active and inactive material with ill-defined material properties and a highly non-homogenous stress field due to the electro-mechanical coupling in ferroelectrics. As mentioned in section 1.2.2 this region is neglected here.

As both secondary cracking and lateral extension of the fringing field could be reduced by utilizing the thinnest specimens possible, very thin plates of 0.5 mm were chosen. Yet, the fringing field still extends about 250 µm into the inactive part (see chapter 2). For an electrode width of 1 mm the initial condition of $b \gg t$ set to ensure a small extension of the fringing field as compared to the electrode width is violated. Accordingly, no conclusive fracture mechanical analysis was possible and only a qualitative analysis was made.

A slight drawback with the choice of 0.5 mm thick plates lies in the fact, that in this thickness regime the R-curve varies with specimen thickness. The ferroelastic toughening depends on the macroscopic stress state (plane stress or plane strain) and the R-curve therefore depends on specimen thickness (see chapter 3). Measuring the R-curve with plates of 1 mm thickness which is the thinnest possible for mechanical loading in our equipment, proved to be the best possible compromise. The thickness dependence of the R - curve can contribute to the experimental scattering in the electric field in figures 4.14 and 4.16.

Another issue arises from the crack growth velocity. Ferroelastic behavior leads to domain switching under the influence of the crack tip stress fields, thereby creating a process zone and providing crack toughening due to crack tip shielding. The amount of shielding again depends on the crack velocity. This effect was accounted for by obtaining R-curves on the specimens with controlled crack velocity and by obtaining the crack tip position after some waiting time in the electrically driven crack measurement. With respect to crack velocity, only the toughening effect and therefore the plateau value of the fracture toughness of an unstably grown crack could not be fully assessed. Work by Glazounov et al. [44], however, showed in X-ray diffraction studies that domain switching occurs even under the conditions of unstable crack growth. Given the very good agreement of the simulation with the experiment in the unstable crack growth regimes it can be concluded that a significant amount of toughening is obtained up to very high crack growth velocities.

A more probable approach to the problem of the K_I-level of the unstable crack growth is to assume that the crack did grow very fast, but still in a velocity regime in which significant domain switching is possible. In that case the K_R would increase because of the increased velocity (see figure 1.6). That would consume the applied energy to some extent and the crack would arrest earlier because the condition $K_I = K_R$ is met at smaller crack lengths. Using only the unmodified K_R-plateau value for the crack length leads to a crack arrest point that is slightly larger than the experimental findings. The "very fast" crack assumption seems to better represent the experimental conditions than the "unstable" crack growth assumption. Yet, in order to quantitatively calculate the crack extension with the velocity modified K_R-plateau knowledge of the influence of velocity on the R-curve is required. Another indication that the crack did not grow unstably is the crack surface. Areas of stable and unstable crack growth showed an identical crack surface. Observation of the crack surface in PLZT showed different crack surfaces for stable and unstable crack growth [43].

The K_R anisotropy discussed previously accounts for another effect concerning the crack growth velocity in the second unstable region. In specimens poled parallel to the electrode edge the crack does run parallel to the polarization direction after deflection. A higher K_R-plateau results from such a configuration (figure 3.5). The "hump" of the K_I-curve, however, should not be affected and the applied energy excess is diminished with the consequence that the crack runs slower than in the unpoled state (figures 4.14 and 4.16).

Since the material properties of the unpoled specimens are isotropic and no piezoelectric effect is obtained at the crack tip, the material behaves, in first approximation, as a regular linear elastic material. The crack path condition for the unpoled material is therefore the expected condition $K_{II} = 0$. In a poled specimen the material is not isotropic and the in plane poling leads to a piezoelectric effect and therefore the condition $K_{II} = 0$ is expected to be no longer valid. First preliminary results on the parallel poled material strongly indicate that a more complex energy criterion is needed to describe the crack growth direction [83].

Chapter 5

Summary

The investigation of failure mechanisms at electrode edges was done in three parts. In the first part concerning crack nucleation it was shown that mechanical clamping in x_2-direction yields very high tensile stresses around the electrode edge and moderate tensile stresses between the electrodes. The localized stresses around the electrode edges initiate cracks which in turn relieve some of the stress. As more energy is needed to switch the domains in the electric field direction (x_1-x_3-plane) with tensile stresses present in x_2-direction the coercive field is raised. Cracks will reduce the stresses and therefore the coercive field will also be reduced to an extent correlated to the amount and size of electrode edge cracks. Since there are still stresses in the specimen, the coercive field will be higher than that in a free specimen.

At low electric fields only the size of the half-cylinder of high tensile stresses under the electrode edges and not the actual specimen geometry is of importance. The actual geometry only influences the cracking by altering the electric potential that is needed for a certain extension of the half-cylinder. From these results it can be concluded that cracking will be present in any electrode edge configuration as long as the edge is inside the material and moderate to high electric fields are applied and the thickness of the ferroelectric material is above a certain threshold. Yet, there is also an upper threshold above which the only the crack length is increased but not the number of cracks.

With more refined tools to calculate the stress distribution under the electrode edge it may be possible to use such experiments to determine a failure probability similar to the Weibull distribution. Since many cracks develop, only a few specimens need to investigated. With the knowledge of the applied stresses, which are a function of the electric field, a critical flaw size can be calculated and by the amount of cracks formed at a given electric field a density of such flaws can be obtained. The main difficulty is the interaction of the cracks with each other and the consequence on the stress distribution.

In the next two parts the crack propagation was investigated. First the material response to crack propagation was measured as R-curves on compact tension specimens. A strong thickness dependence was observed in the measurements with two different behaviors given by the dominant stress state. Specimens in plane stress showed a significantly higher fracture toughness than those in plane strain. The polarization state in 1 mm thick specimens does not contribute to the same degree as in 3 mm thick specimens, but is still an important parameter. The reason for the long linear increase of the fracture toughness in the thin specimens is not yet understood in detail. More work is needed which could clarify some of the domain behavior on an advancing crack. The measured R-curves were then used for the last part of this work in which the crack was driven electrically.

Finally, the crack growth behavior of cracks driven by the strain incompatibility between an active and an inactive region is measured and simulated. Different crack types are achievable by variation of geometric and polarization conditions. The crack paths are reproducible with very high accuracy. Two principally different crack shapes were observed which are a consequence of the achievable strain incompatibility and thus stress. Low stresses lead to straight cracks with two transitions between stable and unstable crack growth regions, while high stresses result in curved cracks with four transitions. The stress level is given by the electrode width, because larger electrodes exhibit higher stresses. The polarization state alters the stress given by the strain incompatibility such that a polarization parallel to the electrode edge enhances the stress and a polarization perpendicular thereto lowers it. Furthermore, the crack shape of the deflected cracks itself is altered by the polarization state.

An iteration method based on finite element modelling is proposed to simulate the propagation of curved cracks also for the case of a strong crack curvature. This fracture mechanical analysis is able to explain the different crack paths depending on the electrode width b and the stable and unstable crack growth stages with their transitions on these paths. In case of an unpoled specimen the crack growth direction of a non-kinked crack is given only by $K_{II} = 0$ like it is the case in non-ferroelastic ceramics. The ferroelastic properties do not manifest themselves as they do in the poled specimens. A more complex energy criterion has to be used to describe the crack growth direction of a poled specimen, but the modelling efforts are still ongoing so no definitive statement can be made at present.

The crack growth condition of a crack growing stably at low speed is simply given by $K_I \geq K_R$. It could not be identified by the investigation, whether the crack grew unstably or only very fast in the areas with an excess of crack driving energy. The latter is strongly assumed, but it could not be verified by the present analysis. A more detailed investigation of the crack growth and domain behavior under various crack growth velocities is needed.

In summary, the results of the fracture mechanical analysis show a very good quantitative agreement with the experiments in the crack contours, in the stages of crack propagation and the transitions between them and also in the crack length as a function of the electric field. The crack propagation, wether unstable or very fast, can be described sufficiently well by the static fields used in the analysis.

Appendix A

Details on the Modelling of Crack Propagation

A.1 Calculation of the Incompatible Strains

The incompatible strains S_{jk} consisting of ferroelectric, ferroelastic and piezoelectric strain can also be understood as the difference between total and elastic strain and are calculated from the measured displacements u_i in figure 4.5. To relate incompatible strain and displacement, the proportionality factors A_{ijk} are introduced:

$$u_i = A_{ijk} S_{jk} \tag{A.1}$$

Due to symmetry conditions in the given asymmetric geometry no shear strains are involved and therefore $S_{jk} = 0$ for all $j \neq k$. In the present analysis only strains in x_2 are of importance. It is therefore of interest to find a measurement direction yielding S_{22} at high precision. With the experimentally easily accessible displacements u_2 equation A.1 becomes

$$u_2 = A_{211} S_{11} + A_{222} S_{22} + A_{233} S_{33}. \tag{A.2}$$

Under the plane stress assumption S_{33} can be expressed by $-\nu/Y(\sigma_{11}+\sigma_{22})$. The x_1 direction is not mechanically clamped and thus σ_{11} is negligible and S_{33} can be eliminated:

$$u_2 = A_{211} S_{11} + (A_{222} - \nu A_{233}) S_{22} = A_{211} S_{11} + A'_{222} S_{22}. \tag{A.3}$$

The coefficients A_{211} and A'_{222} are determined by means of a 2D-plane stress thermoelastic finite element analysis as described in section 4.3 with no crack present. The displacement $\hat{u}_2$ is extracted from the FE calculation at the positions of the real LVDTs in the experiments. In the first step a strain only in x_1 is introduced by choosing $\alpha^T = \left(\begin{smallmatrix} 1 & 0 \\ 0 & 0 \end{smallmatrix}\right)$ and $\Delta T = 1$ K to calculate A_{211} by

$$A_{211} = \hat{u}_2 / S_{11} = \hat{u}_2 / (\alpha^T_{11} \Delta T) = \hat{u}_2. \tag{A.4}$$

In the second step A'_{222} is calculated accordingly by introducing a strain only in x_2 direction. Finally the coefficients are checked by choosing α^T arbitrarily. While A_{211} is negligible for all electrode widths and LVDT positions because of the electrode and specimen geometry, A'_{222} is specific to the given sizes. Finally the relationship between displacement and strain is determined by

$$u_2 = A'_{222} S_{22}. \tag{A.5}$$

Measurement of the displacements in x_2 direction is sufficient to derive the incompatible strains S_{22} which are needed for the calculation of the applied stress intensity factors for a given electric field.

A.2 Calculation of the Stress Intensity Factors for the Applied Load

The stress intensity factors are calculated as described in section 4.3 for a reference load σ^{ref} given by the thermoelastic strain $S_{22}^{ref} = \alpha_{22}^T \Delta T$ which is constant throughout the whole simulation. K_I^{ref} is thus given by

$$K_I^{ref} = \sigma^{ref} f(a/b) = Y_{22} S_{22}^{ref} f(a/b). \tag{A.6}$$

With knowledge of the actually applied incompatible strain S_{22} the stress intensity factor can be easily calculated from the reference load case which provides the geometry term $f(a/b)$. Using equation A.5 the dependence of the stress intensity factor from the applied electric field can be obtained:

$$K_I(E) = Y_{22} \frac{u_2(E)}{A'_{222} S_{22}^{ref}} f(a/b) \tag{A.7}$$

Appendix B

Custom Software

All the custom designed software programs were written in Delphi 3 (Borland/Inprise) except for the Leica QWin interface which was programmed with the internal programming language Quips (Leica).

B.1 Data Logging Software

The data logging software was written with the requirement to simultaneously read four analogue inputs and control one analogue output with an AD/DA-card. Because of the high quality of the digitizer and the software libraries the card KPCI3102 from Keithley was used. The card offers 16 single ended analogue input and two analogue outputs of which the inputs 1-4 and the output 1 are used.

The operator can individually choose an on-board amplification of the input signal between a factor of 1×, 2×, 4× and 8×. With a maximum digitizer input of ±10 V the amplification leads to an input range of ±10 V, ±5 V, ±2.5 V or ±1.25 V, respectively. The digitizer has a resolution of 12bit yielding an input sensitivity between 9.8 mV for ±10 V and 1.2 mV for ±1.25 V. Additionally, each input channel can be given a conversion factor that is multiplied to the digital value to convert the measured input voltage to the desired unit. The output channel can be switched from bipolar to unipolar to use the full 12bit resolution in the range 0 - 10 V (2.4 mV / step).

Individual channels can be switched off for data logging to economize memory and the sample rate can be adjusted to values up to 1 kHz. Since the channels have to be sampled individually an internal sample rate of 100 kHz is chosen to simulate simultaneous sampling. Every time the software requests a sample, the channels are sampled sequentially at 100 kHz once, a data vector with all the channels is returned and the card then waits for the next request. To ensure precise timing the clock on the AD/DA card is used instead of the Windows clock which sometimes omits a “click” and does not guarantee constant timing. A maximum sample rate of 1 kHz is low compared to other sample solutions. But the fact that the input cycle is linked to the output cycle prohibits the use of almost all fast data transfer techniques available.

The analogue output can be set by the operator in steps of 0.01 V. The transition between two output voltages can be stepwise or as a ramp of 0.01 V/s to 1 V/s. In case of a ramp transition the new output voltage is calculated up to the full 12 bit output resolution at each sampling. Since the output cycle is linked to the input sampling the ramp becomes smoother with higher sampling rates as smaller steps can be used per sample. As mentioned before, the minimum step is 2.4 mV.

The data are stored in the volatile memory (RAM) of the computer and the amount of data is therefore limited by the memory size. Hard-disk storage of the data is too slow to guarantee a maximum sample rate of 1 kHz.

B.2 Connection to the Leica Microscope Software QWin

In order to read out the values of the computerized coordinate desk attached to the optical microscope an interface had to be programmed within the Leica software QWin using the internal programming language Quips. The data transfer between QWin and other programs itself was done by the DDE (Direct Data Exchange) subsystem of the Microsoft Windows operating system. DDE is a client-server type system that enables independent software to interact with each other over so-called channels. The server has a list of functions and listens to incoming "calls" from the client software which then can use the functions to control the server. The data flow is open in both directions. In this case the custom software is programmed as server while QWin was technically the client. This means that the connection has to be opened and closed by QWin. A schematic overview over the data flow is given in figure B.1

After QWin and the custom software are loaded the user initiates the connection by starting the interface. QWin then opens a channel to the custom software and goes into a "listening-mode" (step 1). Three commands are defined which the custom software can send to QWin. QWin in turn answers with the desired data or with "`ok`" after execution of the request. A list of commands and answers is given in table B.1. The custom software now sends commands (step 2) and QWin answers (step 3) until the command "`end`" is send (step 4) which tells

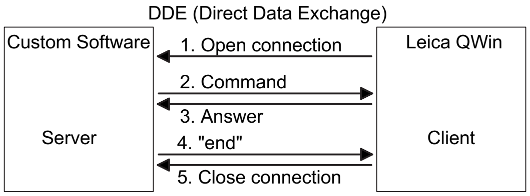

Figure B.1: Schematic overview over the data flow between Leica QWin and other software

Table B.1: Overview of the functions for the DDE connection between Leica QWin and custom software.

Command send to QWin	Answer from QWin
`givexy`	`stage xxxx;yyyy`
	where xxxx and yyyy are the actual coordinates
`setorigin`	`ok`
`end`	close the connection

QWin to close the connection (step 5) and terminate the interface program. With this custom designed program a versatile interface to operate with different external programs is provided. Two applications are described in the next sections.

B.3 Crack Mapping Software

The software for the crack mapping makes use of the interface to the coordinate desk. The purpose of this program is to provide an up-to-scale map of the cracks on the surface as seen in the optical microscope. To do so the program reads the coordinates of the coordinate desk 5 times per second and stores the data with a description upon user request. The screen output is scaled such that all data-points fit on the screen. Furthermore the software can export the data as text-file for use in other programs for further analysis and as HPGL-file for plotting. The latter is a standard format for vector-data. A screen-shot of the program is shown in figure B.2.

Several description categories for distinguishing the data-points are available. The first consists of four descriptions for the four outer edges of the specimen. The four edges of the electrodes are marked by the next category. Each description of the those two categories can be used only once per specimen as the descriptions are such as “specimen edge top-left” and there is only one such per specimen. All the following descriptions can be used as often as needed. The main category for the description of the cracks consists of the descriptions “crack start/end”, “crack intersection with electrode edge” and “crack-kink”. The different cracks are distinguished by a number set by the operator. There is one description called “others” to mark other types of artifacts and finally the option to add text at the current coordinate. This is especially used to add information about the electric field in the crack growth experiments. The descriptions are used by the software to generate the crack map.

The program has a subroutine to calculate the mean specimen and electrode size by evaluating the coordinates of the specimen and electrode edges marked previously. Both electrodes and the specimen are assumed to have trapezoidal shape. The program calculates the mean width and the mean height of the trapezoid. The output is seen in the centered dialog-box in figure B.2.

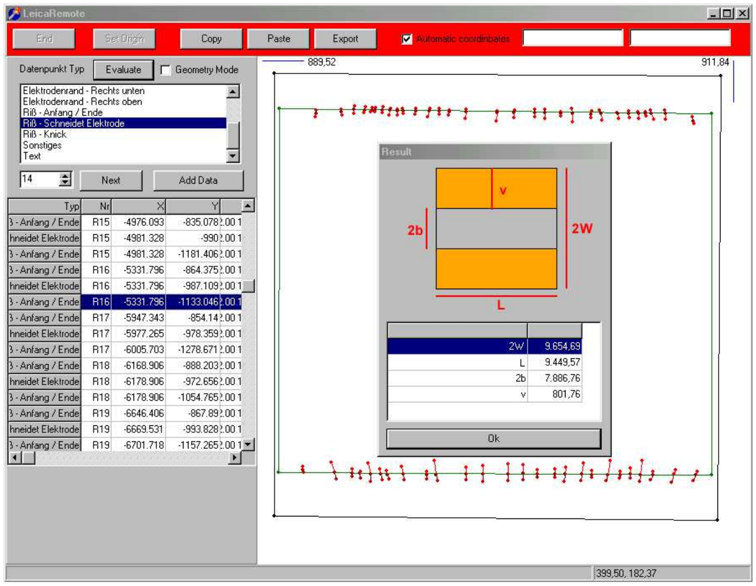

Elektrodenrand - Rechts unten
Elektrodenrand - Rechts oben
Riß - Anfang / Ende
Riß - Schneidet Elektrode
Riß - Knick
Sonstiges
Text

Typ	Nr	X	Y
- Anfang / Ende	R15	-4976.093	-835.078
hneidet Elektrode	R15	-4981.328	-990
- Anfang / Ende	R15	-4981.328	-1181.406
- Anfang / Ende	R16	-5331.796	-864.375
hneidet Elektrode	R16	-5331.796	-987.109
- Anfang / Ende	R16	-5331.796	-1133.046
- Anfang / Ende	R17	-5947.343	-854.14
hneidet Elektrode	R17	-5977.265	-978.359
- Anfang / Ende	R17	-6005.703	-1278.671
- Anfang / Ende	R18	-6168.906	-888.203
hneidet Elektrode	R18	-6178.906	-972.656
- Anfang / Ende	R18	-6178.906	-1054.765
- Anfang / Ende	R19	-6646.406	-867.89
hneidet Elektrode	R19	-6669.531	-993.828
- Anfang / Ende	R19	-6701.718	-1157.265

2W	9.654,69
L	9.449,57
2b	7.886,76
v	801,76

Figure B.2: Screen-shot of the crack mapping software

B.4 R-Curve Measurement Software

The R-curve measurement software does also use the QWin interface to the coordinate desk. Additionally, the computer is connected to the measuring bridge by a serial cable to read out the value of the load cell. Both coordinates (x - and y - position) and the load P are read 5 times per second. Furthermore, the specimen dimensions (thickness B, ligament length W and the coordinate offset δx) are typed into the software.

Then the specimen is loaded and the crosshairs in the eye-pieces are placed some distance ahead of the crack tip. When the crack tip passes the crosshairs the data point is stored by pressing a key. At the same time the internal clock is reset by which the time between two data points is measured and the crack growth velocity is calculated. With those inputs the software can calculate the applied stress intensity factor by equation B.1 with the real crack length $a = \delta x + x$ according to [73, 16] as well as the crack growth velocity.

$$K_I = \frac{P}{B \cdot \sqrt{W}} \cdot \frac{(2 + \frac{a}{W}) \cdot (0.886 + 4.64\frac{a}{W} - 13.32(\frac{a}{W})^2) + 14.72(\frac{a}{W})^3 - 5.6(\frac{a}{W})^4)}{(1 - \frac{a}{W})^{\frac{3}{2}}} \tag{B.1}$$

The software maintains a list consisting of the crack length a, load P, stress intensity factor K_I, time between two data points Δt and the crack growth velocity between two data points v which can be exported to further use with other programs. The list is visible during the experiment such that the operator can check the velocity after each data point. Furthermore, the R-curve is shown on the screen in real time.

Appendix C

Tables

Table C.1: Material constants for the nonlinear finite element model chosen as approximation for the material used in the experiments (PIC 151). The parameters in the lower section are described in [33].

Young's modulus	Y^E	$6.0{\times}10^{10}$ N/m^2
Poisson's ratio	ν	0.37
Dielectric constant	$\varepsilon^T/\varepsilon_0$	2260
Piezoelectric constants	d_{33}	$4.5{\times}10^{-10}$ m/V
	d_{31}	$-2.1{\times}10^{-10}$ m/V
	d_{15}	$5.8{\times}10^{-10}$ m/V
Coercive field	E_C	$1.0{\times}10^{6}$ V/m
Maximum irreversible polarization	P_{irrev}	0.29 C/m^2
Coercive stress	σ_C	$4.0{\times}10^{7}$ N/m^2
Maximum irreversible strain	S_{irrev}	0.002
	c^p	$1.0{\times}10^{6}$ Vm/C
	c^f	$2.0{\times}10^{10}$ N/m^2
	m	$2.0{\times}10^{8}$ N/m^2
	n	$2.0{\times}10^{7}$ N/m^2
	P_δ	0.1 C/m^2

Table C.2: Overview over the specimens in each batch.

Batch	Thickness	Dimension
S1	3.0 mm	50 × 48 mm^2
S2	3.0 mm	50 × 48 mm^2
S3	3.0 mm	50 × 48 mm^2
	1.0 / 2.0 / 4.0 / 8.0 mm	40 × 40 mm^2
	1.0 / 3.0 / 6.0 mm	35 × 33.6 mm^2
S4	0.5 / 1.0 mm	40 × 40 mm^2
S5	0.5 / 1.0 mm	40 × 40 mm^2
	1.0 mm	35 × 33.6 mm^2

Table C.3: Material properties for PIC PZT 151.

		Manufacturer data
Young's Moduls	S_{11}	6.667×10^{10} N/m^2
	S_{33}	5.263×10^{10} N/m^2
Poisson's ratio	ν	0.25
Dielectric constants	$\varepsilon_{33}/\varepsilon_0$	2100
	$\varepsilon_{11}/\varepsilon_0$	1980
Piezoelectric constants	d_{33}	4.5×10^{-10} m/V
	d_{31}	-2.1×10^{-10} m/V
	d_{15}	5.8×10^{-10} m/V
Curie temperature	T_C	250℃
Coercive Field	E_C	650 V/mm
Grain size	G	3-5µm

Bibliography

[1] K. Uchino. “Piezoelectric Actuators and Ultrasonic Motors”. *Kluwer Academic Publ., Boston*, 1997.

[2] G. H. Haertling. “Ferroelectric Ceramics: History and Technology”. *J. Am. Ceram. Soc.*, 82[4], pp. 797–818, 1999.

[3] B. Jaffe, W. R. Cook and H. Jaffe. “Piezoelectric Ceramics”. *Academic Press, London*, 1971.

[4] Y. Xu. “Ferroelectric Materials and their Applications”. *Elsevier Science Publishers B.V., Amsterdam*, 1990.

[5] A. S. Sonin and B. A. Strukow. “Einführung in die Ferroelektrizität”. *Akademie Verlag, Berlin*, 1974.

[6] J. F. Nye. “Physical Properties of Crystals”. *Oxford Science Publ., Oxford*, 1984.

[7] W. Kleber. “Einführung in die Kristallographie”. *Verlag Technik GmbH, Berlin*, 1990.

[8] S. C. Hwang, C. S. Lynch and R. M. McMeeking. “Ferroelectric/Ferroelastic Interactions and a Polarization Switching Model”. *Acta Mater.*, 43[5], pp. 2073–2084, 1995.

[9] V. M. Rudyak. “Viscosity Phenomena and Switching Process in Ferroelastics”. *Ferroelectrics*, 48, pp. 131–141, 1983.

[10] C. S. Lynch. “The effect of uniaxial stress on the electro-mechanical response of 8/65/35 PLZT”. *Acta Mater.*, 44[10], pp. 4137–4148, 1996.

[11] C. A. Randall, N. Kim, J.-P. Kucera, W. Cao and T. R. Shrout. “Intrinsic and Extrinsic Size Effects in Fine-Grained Morphotropic-Phase-Boundary Lead Zirconate Titanate Ceramics”. *J. Am. Ceram. Soc.*, 81[3], pp. 677–688, 1998.

[12] R. E. Newnham. “Molecular Mechanisms in Smart Materials”. *MRS Bulletin*, [5], pp. 20–33, 1997.

[13] B. Noheda, J. A. Gonzalo, S.-E. Park, L. E. Cross, D. E. Cox and G. Shirane. "The Monoclinic Phase in PZT: New Light on Morphotropic Phase Boundaries". *Proc. Ferroelectric Workshop, Aspen, CO*, 2000.

[14] G. Helke and W. Kirsch. "Dielektrische und piezoelektrische Eigenschaften der ternären keramischen festen Lösungen $\mathrm{Pb(Ni_{1/3}Sb_{2/3})O_3 - PbTiO_3 - PbZrO_3}$". *Hermsdorfer Technische Mitteilungen*, 32, pp. 1010–1015, 1971.

[15] S. L. dos Santos e Lucato. "Rißausbreitung in Blei-Zirconat-Titanat in Abhängigkeit des Polungszustandes". *Diploma Thesis, Darmstadt University of Technology*, 1999.

[16] H. Tada, P. C. Paris and G. R. Irwin. "The Stress Analysis of Cracks Handbook". *Paris Prod. Inc., St. Louis*, 1985.

[17] Y. Murakami. "Stress Intensity Factors Handbook". *Pergamon Press, New York*, 1987.

[18] B. R. Lawn. "Fracture of Brittle Solids". *Cambridge Univ. Press., Cambridge*, 2nd. Ed., 1993.

[19] R. M. McMeeking and A. G. Evans. "Mechanics of Transformation-Toughening in Brittle Materials". *J. Am. Ceram. Soc.*, 65[5], pp. 242–246, 1982.

[20] D. C. Lupascu, S. L. dos Santos e Lucato, J. Rödel, M. Kreuzer and C. S. Lynch. "Liquid-Crystal Display of Stress Fields in Ferroelectrics". *Appl. Phys. Let.*, 78[17], pp. 2554–2556, 2001.

[21] S. M. Wiederhorn. "Subcritical Crack Growth in Ceramics". *Frac. Mech. Ceram.*, [Vol. 2], pp. 613–646, 1973.

[22] T. Fett. "A Fracture-Mechanical Theory of Subcritical Crack Growth in Ceramics". *Int. J. Fract. Mech.*, 54, pp. 117–130, 1992.

[23] S. M. Wiederhorn. "Influence of Water Vapor on Crack Propagation in Soda-Lime Glass". *J. Am. Ceram. Soc.*, 50[8], pp. 407–414, 1967.

[24] M. C. Knechtel, D. E. Garcia, J. Rödel and N. Claussen. "Subcritical Crack Growth in Y-TZP and $\mathrm{Al_2O_3}$-Toughened Y-TZP". *J. Am. Ceram. Soc.*, 76[10], pp. 2681–2684, 1993.

[25] J. Menchaca, S. L. dos Santos e Lucato, D. C. Lupascu, J. Rödel and C. S. Lynch. "Polarization and Electrode Dependence of the v-K behavior in PZT". unpublished.

[26] S. L. dos Santos e Lucato, H.-A. Bahr, V. B. Pham, D. C. Lupascu, H. Balke, J. Rödel and U. Bahr. "Electrically Driven Cracks in PZT: Experiments and Fracture Mechanical Analysis". *J. Mech. Phys. Solids*, submitted.

[27] J. W. Hutchinson and Z. Suo. "Mixed Mode Cracking in Layered Materials". *Adv. Appl. Mech.*, 29, pp. 63–191, 1991.

[28] B. Cotterell and J.R. Rice. “Slightly Curved or Kinked Cracks”. *Int. J. Fract.*, 16, pp. 155–169, 1980.

[29] Z. Suo, C.-M. Kuo, D.M. Barnett and J.R. Willis. “Fracture Mechanics for Piezoelectric Ceramics”. *J. Mech. Phys. Solids*, 40, pp. 739–765, 1992.

[30] H.-A. Bahr, U. Bahr, A. Gerbatsch, I. Pflugbeil, A. Voijta and H.-J. Weiss. “Fracture Mechanical Analysis of Morphological Transitions in Thermal Shock Cracking”. *Fracture Mechanics of Ceramics*, Vol. 11, pp. 507–522, 1995.

[31] D. Fang, A. K. Soh and J.-X. Liu. “Advances in Studies of Electromechanical Deformation and Fracture of Piezoelectric / Ferroelectric Materials”. *Acta Mech. Sinica*, 17[3], pp. 193–213, 2001.

[32] N. Setter and R. Waser. “Electroceramic Materials”. *Acta Mater.*, 48, pp. 151–178, 2000.

[33] M. Kamlah. “Ferroelectric and Ferroelastic Piezoceramics - Modelling of Electromechanical Hysteresis Phenomena”. *Cont. Mech. Thermo.*, 13[4], pp. 219–268, 2001.

[34] K. Okazaki. “Mechanical Behavior of Ferroelectric Ceramics”. *Ceram. Bul.*, 63[9], pp. 1150–1152, 1984.

[35] G. G. Pisarenko, V. M. Chushko and S. P. Kovalev. “Anisotropy of Fracture Toughness of Piezoelectric Ceramics”. *J. Am. Ceram. Soc.*, 68[5], pp. 259–265, 1985.

[36] T. Fett, D. Munz and G. Thun. “Fracture Toughness and R-Curve Behaviour of PZT”. *Wiss. Berichte d. Forschungszentrums Karlsruhe, FZKA*, 6058, 1998.

[37] F. Meschke, A. Kolleck and G. A. Schneider. “R-Curve Behaviour of $BaTiO_3$ due to Stress-Induced Ferroelastic Domain Switching”. *J. Europ. Ceram. Soc.*, 17, pp. 1143–1149, 1997.

[38] S. L. dos Santos e Lucato, D. C. Lupascu and J. Rödel. “Effect of Poling Direction on R-Curve Behavior in Lead Zirconate Titanate”. *J. Am. Ceram. Soc.*, 83[2], pp. 424–426, 2000.

[39] S. L. dos Santos e Lucato, J. Lindner, D. C. Lupascu and J. Rödel. “Influence of the Electrical and Geometrical Boundary Conditions on Crack Growth in PZT”. *Key Eng. Mat.*, 206-213, pp. 609–612, 2002.

[40] A. Kolleck, G. A. Schneider and F. Meschke. “R-Curve Behavior of $BaTiO_3$- and PZT-Ceramics Under the Influence of an Electric Field Applied Parallel to the Crack Front”. *Acta Mater.*, 48[16], pp. 4099–4113, 2000.

[41] K. Mehta and A. V. Virkar. “Fracture Mechanisms in Ferroelectric-Ferroelastic Lead Zirconate Titanate (Zr:Ti=0,54:0,46) Ceramics”. *J. Am. Ceram. Soc.*, 73[3], pp. 567–574, 1990.

[42] S. W. Freiman and R. C. Pohanka. “Review of Mechanically Related Failures of Ceramic Capacitators and Capacitator Materials”. *J. Am. Ceram. Soc.*, 72[12], pp. 2258–2263, 1989.

[43] W. Chen, D. C. Lupascu, J. Rödel and C. S. Lynch. “Short Crack R-Curves in Ferroelectric and Electrostrictive PLZT”. *J. Am. Ceram. Soc.*, 84[3], pp. 593–597, 2001.

[44] A. E. Glazounov, T. Fett, J.-Th. Reszat, M. J. Hoffmann, D. Munz and T. Wroblewski. “Influence of Domain Switching State on R-curves Interpreted by using X-ray Diffraction”. *J. Mat. Sci. Letters*, 20, pp. 877–880, 2001.

[45] S. Hackemann. “Ortsaufgelöste röntgendiffraktometrische Charakterisierung von Domänenumklappvorgängen in ferroelektrischen Keramiken”. *Ph.D. thesis, Universität Karlsruhe*, 2001.

[46] W. Chen and C. S. Lynch. “Multiaxial Constitutive Behavior of Ferroelectric Materials”. *J. Eng. Mat. Tech.*, 123[April], 2001.

[47] Y. E. Pak. “Crack Extension Force in a Piezoelectric Material”. *J. Appl. Mech.*, 57, pp. 647–653, 1990.

[48] H. Sosa. “On the Fracture Mechanics of Piezoelectric Solids”. *Int. J. Solids Struct.*, 29[21], pp. 2613–2622, 1992.

[49] S. B. Park and C.-T. Sun. “Fracture Criteria for Piezoelectric Ceramics”. *J. Am. Ceram. Soc.*, 78[6], pp. 1475–1480, 1995.

[50] H. Gao, T.-Y. Zhang and P. Tong. “Local and Global Energy Release Rates for an Electrically Yielded Crack in a Piezoelectric Ceramic”. *J. Mech. Phys. Solids*, 45[4], pp. 491–510, 1997.

[51] R. M. McMeeking. “Towards a Fracture Mechanics for Brittle Piezoelectric and Dielectric Materials”. *Int. J. Fract.*, 108, pp. 25–41, 2001.

[52] F. Yang. “Fracture Mechanics for a Mode I Crack in Piezoelectric Materials”. *Int. J. Solids Struct.*, 38, pp. 3813–3830, 2001.

[53] T. Zhu and W. Yang. “Toughness Variation of Ferroelectrics by Polarization Switch under Non-Uniform Electric Field”. *Acta Mater.*, 45[11], pp. 4695–4702, 1997.

[54] W. Yang and T. Zhu. “Switch-Toughening of Ferroelectrics Subjected to Electric Field”. *J. Mech. Phys. Solids*, 46[2], pp. 291–311, 1998.

[55] W. Yang, F. Fang and M. Tao. “Critical Role of Domain Switching on the Fracture Toughness of Poled Ferroelectrics”. *Int. J. Solids Struct.*, 38, pp. 2203–2211, 2001.

[56] A. Furuta and K. Uchino. “Dynamic Observation of Crack Propagation in Piezoelectric Multilayer Actuators”. *J. Am. Ceram. Soc.*, 76[6], pp. 1615–1617, 1993.

[57] H. Aburatani, S. Harada, K. Uchino, A. Furuta and Y. Fuda. “Destruction Mechanisms in Ceramic Multilayer Actuators”. *Jpn. J. Appl. Phys.*, 33[1 / 5b], pp. 3091–3094, 1994.

[58] S. Takahashi, A. Ochi, M. Yonezawa, T. Yano, T. Hamatsuki and I. Fukui. “Internal Electrode Piezoelectric Ceramic Actuator”. *Ferroelectrics*, 50, pp. 181–190, 1983.

[59] G. A. Schneider, A. Rostek, B. Zickgraf and F. Aldinger. “Crack Growth in Ferroelectric Ceramics under Mechanical and Electrical Loading”. *Electroceramics IV, Augustinus Buchhandlung, Aachen*, ed. 1, pp. 1211–1216, 1995.

[60] G. A. Schneider, H. Weitzing and B. Zickgraf. “Crack Growth in Ferroelectric Ceramics and Actuators under Mechanical and Electrical Loading”. *Frac. Mech. Ceram.*, 12, pp. 149–160, 1996.

[61] Z. Suo. “Models for Breakdown Resistant Dielectric and Ferroelectric Ceramics”. *J. Mech. Phys. Solids*, 41, pp. 1155–1176, 1993.

[62] C. L. Hom and N. Shankar. “A Finite Element Method for Electrostrictive Ceramic Devices”. *Int. J. Solids Struct.*, 33[12], pp. 1757–1779, 1996.

[63] T. H. Hao, X. Y. Gong and Z. Suo. “Fracture Mechanics for the Design of Ceramic Multilayer Actuators”. *J. Mech. Phys. Solids*, 44[1], pp. 23–48, 1996.

[64] X. Y. Gong and Z. Suo. “Reliability of Ceramic Multilayer Actuators: a Nonlinear Finite Element Simulation”. *J. Mech. Phys. Solids*, 44[5], pp. 751–769, 1996.

[65] P. H. Hasselman. “Unified Theory of Thermal Shock Fracture Initiation and Crack Propagation of Brittle Ceramics”. *J. Am. Ceram. Soc.*, 52, pp. 600–604, 1969.

[66] S. Nemat-Nasser, L.M. Keer and K.S. Parihar. “Unstable Growth of Thermally Induced Interacting Cracks in Brittle Solids”. *Int. J. Solids Struct.*, 14, pp. 409–430, 1978.

[67] S. Nemat-Nasser, Y. Sumi and L.M. Keer. “Unstable Growth of Tension Cracks in Brittle Solids: Stable and Unstable Bifurcations, Snap Through, and Imperfection Sensitivity”. *Int. J. Solids Struct.*, 16[11], pp. 1017–1035, 1980.

[68] H.-A. Bahr, H. Balke, M. Kuna and H. Liesk. “Facture Analysis of a Single Edge Cracked Strip under Thermal Shock”. *Theor. Appl. Fract. Mech.*, 8, pp. 33–39, 1987.

[69] P. J. Potts. “A Handbook of Silicate Rock Analysis”. *Blackie & Son Ltd., London*, 1987.

[70] S. L. dos Santos e Lucato, D. C. Lupascu, M. Kamlah, J. Rödel and C. S. Lynch. “Constraint - Induced Crack Initiation at Electrode Edges in Piezoelectric Ceramics”. *Acta Mater.*, 49[14], pp. 2751–2759, 2001.

[71] M. Kamlah and U. Böhle. “Finite Element Analysis of Piezoceramic Components Taking into account Ferroelectric Hysteresis Behavior”. *Int. J. Solids Struct.*, 38[4], pp. 605–633, 2001.

[72] T. Fett and D. Munz. “Measurement of Young’s Moduli for Lead Zirconate Titanate (PZT) Ceramics”. *J. Test. Eval.*, [Jan.], pp. 27–35, 2000.

[73] ASTM. “Standard Test Method for Plane-Strain Fracture Toughness of Metallic Materials, E399-90”. *Annual Book of ASTM standards*, 3.03, pp. 407–437, 1996.

[74] A. Kotousov and C. H. Wang. “Effect of Plate Thickness on Crack-Tip Plasticity”. *Int. J. Fract.*, 111, pp. L53–L58, 2001.

[75] T. Fett, D. Munz and G. Thun. “Nonsymmetric Deformation Behavior of Several PZT Ceramics”. *J. Mat. Sci. Letters*, 18, pp. 1641–1643, 1999.

[76] Ansys Rev. 5.5.3. *Swanson Analysis Systems Inc., Houston, USA*, 1998.

[77] D. Gross. “Bruchmechanik”. *Springer-Verlag, Berlin*, 2. Aufl., 1996.

[78] K.P. Herrmann and H. Grebner. “Curved Thermal Crack Growth in Nonhomogeneous Materials with Different Shaped External Boundaries I. Theoretical Results”. *Theor. Appl. Fract. Mech.*, 2, pp. 133–146, 1984.

[79] K.P. Herrmann and M. Dong. “Thermal Cracking of Two-phase Composite Structures under Uniform and Non-Uniform Temperature Distribution”. *Int. J. Solids Struct.*, 29, pp. 1789–1812, 1992.

[80] J. Gunnars, P. Stähle and T.C. Wang. “On Crack Path Stability in a Layered Material”. *Comp. Mech.*, 19, pp. 545–552, 1997.

[81] Y. Sumi. “Computational Crack Path Prediction”. *Theor. Appl. Fract. Mech.*, 4, pp. 149–156, 1985.

[82] H. Theilig. “A Higher Order Fatigue Crack Paths Simulation by the MVCCI-Method”. *Advances in Fracture Research, Proceeding of the 9th ICF*, pages 2235–2243, 1997.

[83] H. Balke, H.-A. Bahr, V. B. Pham, U. Bahr, S. L. dos Santos e Lucato, J. Rödel, R. Niefanger and G. A. Schneider. “Fracture Mechanical Modelling of Electrically Driven Cracks in PZT”. *Presentation, DFG Status Seminar, Materialwoche*, 2001.

Symbols

All quantities are given in SI - units.

a	Crack length [m]
d	Piezoelectric constant [m/V]
D	Dielectric displacement [C/m^2]
D^R	Remnant dielectric displacement [C/m^2]
E	Electric field [V/m]
E_c	Coercive field [V/m]
E^S	Electric field at strain saturation [V/m]
$\mathcal{G}$	Energy release rate [N/m]
$\mathcal{G}_c$	Critical energy release rate [N/m]
K_I, K_{II}	Mode I and II stress intensity factors [MPam$^{\frac{1}{2}}$]
K_{Ic}	Fracture toughness [MPam$^{\frac{1}{2}}$]
K_R	Crack resistance [MPam$^{\frac{1}{2}}$]
P^S	Spontaneous polarization [C/m^2]
s	Compliance tensor [m^2/N]
S	Strain
S^R	Remnant strain
S^S	Saturation strain
T	Temperature [°C]
t_c	Critical layer thickness for cracking [m]
T_c	Curie temperature [°C]
Y	Young's modulus [GPa]
ε	Dielectric constant [C^2/Nm^2]
λ_D	Depth at start of crack deflection [m]
λ_T	Depth at end of crack deflection [m]
σ	Stress [N/m^2]
σ_c	Coercive stress [N/m^2]
σ_y	Yield stress [N/m^2]
ϕ	Electric potential [V]

Specimen geometry

a	Crack length
b, $2b$	Electrode width (Half width for the symmetric geometry)
L	Specimen length (Parallel to the electrode)
t	Specimen thickness
W, $2W$	Specimen width (Half width for the symmetric geometry)

Curriculum Vitae

Education

Schillerschule, Frankfurt (High-school)	(7/85 - 5/93)
Darmstadt University of Technology	(10/93 - 5/02)
M. S. Materials Science	(2/99)
Ph. D. Materials Science	(2/02)

Experience

Darmstadt University of Technology, Ph. D. Research	(4/99 - 5/02)
Georgia Institute of Technology, Visiting Researcher	(1/00 - 3/00)
Georgia Institute of Technology, Visiting Researcher	(1/01 - 3/01)
University of Florida, Visiting Researcher	(7/97 - 10/97)
Darmstadt University of Technology, Undergraduate Research Assistant	(5/96 - 3/98)
Hochtief AG, Project Manager, Computational Department	(8/90 - 3/98)

Honors and Certifications

• Hans - Walter - Hennicke - Prize (1st Prize) of the 'Deutsche Keramische Gesellschaft' (German Ceramic Society)	(10/99)
• 1st Place in the Ceramographic contest of the American Ceramic Society in the category 'Optical Mircoscopy'	(4/01)
• 2nd Place in the Ceramographic contest of the American Ceramic Society in the category 'Problem Solving'	(4/01)

Refereed Publications

S. L. dos Santos e Lucato, D. C. Lupascu, J. Rödel, “Effect of Poling Direction on R-Curve Behavior in Lead Zirconate Titanate”, *J. Am. Cer. Soc.*, 83[2]2000, pp. 424-426

S. L. dos Santos e Lucato, D. C. Lupascu, M. Kamlah, J. Rödel, C. S. Lynch, “Constraint - Induced Crack Initiation at Electrode Edges in Piezoelectric Ceramics”, *Acta Mater.*, 49[14]2001, pp. 2751-2759

S. L. dos Santos e Lucato, D. C. Lupascu, J. Rödel, “Crack Initiation and Crack Propagation in Partially Electroded PZT”, *J. Europ. Cer. Soc.*, 21[10-11]2001, pp. 1425-1428

D. C. Lupascu, S. L. dos Santos e Lucato, J. Rödel, M. Kreuzer, C. S. Lynch, “Liquid-Crystal Display of Stress Fields in Ferroelectrics”, *Appl. Phys. Let.*, 78[17]2001, pp. 2554-2556

S. L. dos Santos e Lucato, H.-A. Bahr, V. B. Pham, D. C. Lupascu, H. Balke, J. Rödel, U. Bahr, “Electrically Driven Cracks in PZT: Experiments and Fracture Mechanical Analysis”, *J. Mech. Phys. Solids*, submitted

Oral Presentations

S. L. dos Santos e Lucato, “Einfluß des Polungszustandes auf das Rißausbreitungsverhalten in PZT”, Annual meeting of the German Ceramic Soc., Freiberg, Germany, 1999

S. L. dos Santos e Lucato, D. C. Lupascu, J. Rödel, “Electrically Driven Cracks in PZT”, SPIE conference on ‘Smart Structures 2000’, Newport Beach, USA, 2000

S. L. dos Santos e Lucato, D. C. Lupascu, J. Rödel, “Crack initiation and crack propagation in partially electroded PZT”, Electroceramics, Portoroz, Slovenia, 2000

S. L. dos Santos e Lucato, D. C. Lupascu, H.-A. Bahr, H. Balke, J. Rödel, “Deflection of Electrically Driven Cracks in PZT: Experiments”, SPIE conference on ‘Smart Structures 2001’, Newport Beach, USA, 2001

S. L. dos Santos e Lucato, J. Rödel, A. B. Kounga, D. C. Lupascu, “Ferroelastic Toughening in PZT” (Invited Talk), Annual meeting of the American Ceramic Soc., Indianapolis, USA, 2001

S. L. dos Santos e Lucato, D. C. Lupascu, A. Kounga, J. Rödel, “Crack Growth and Crack Characterization in PZT”, 7th meeting of the European Ceramic Society, Brugge, Belgium, 2001

S. L. dos Santos e Lucato, D. C. Lupascu, J. Rödel, H. Balke, H.-A. Bahr, V.-B. Pham, M. Kamlah, U. Bahr, “Electrically Driven Crack Initiation and Propagation in PZT”, Materials Week, Munich, Germany, 2001

Zusammenfassung

Keramische Vielschichtaktuatoren werden in zahlreichen Anwendungen eingesetzt, in denen es auf schnelle und genaue Positionierung bei verhältnismäßig großen Verstellwegen ankommt. Die kostengünstigste Herstellungsweise dieser Aktuatoren setzt eine kammartige Anordnung der Elektroden voraus. Die dadurch bedingten internen Elektrodenkanten führen zu einer nur teilweisen Elektrodenbedeckung, die ihrerseits zu einer Dehungungsinkompatibilität zwischen den aktiven und inaktiven Bereichen im Bauelement führt. Die daraus resultierenden Risse führen schließlich zum Versagen des gesamten Bauteils.

In der vorliegenden Arbeit wird die Rißentstehung und das Rißwachstum an Modellexperimenten unter verschiedenen elektrischen und mechanischen Randbedingungen untersucht. Dabei wird die partielle Elektrodenbedeckung im Aktuator durch dünne Scheiben einer piezoelektrischen Keramik (PZT) mit unterschiedlichen Geometrien, Elektrodenbedeckungen und Probendicken modelliert. Nichtlineare finite Elemente Modellierung und bruchmechanische Analysen werden herangezogen, um das Materialverhalten und die vorliegenden Gleichgewichtsbedingungen zu untersuchen.

Die Untersuchung der Versagensmechanismen an Elektrodenkanten wurde in drei Teilen durchgeführt. Der erste Teil befaßt sich mit der Rißentstehung. Darin wurde gezeigt, daß die mechanische Klemmung in x_2 - Richtung sehr hohe mechanische Zugspannungen an der Elektrodenkante und geringe Zugspannungen zwischen den Elektroden zur Folge hat. Die lokalisierten Spannungen um die Elektrodenkante führen zu Rißentstehung, die wiederum mit einer teilweisen Entlastung der Probe einher geht. Mechanische Zugspannung in x_2 - Richtung bedingt, daß mehr Energie benötigt wird, um Domänen in Richtung des elektrischen Feldes ($x_1 - x_3$ - Ebene) zu schalten. Risse reduzieren die Spannung, und dementsprechend wird die Koerzitivfeldstärke in einem Maße erniedrigt, die mit der Anzahl der Risse korreliert. Da die Probe durch die Risse nicht komplett entlastet wird, liegt die Koerzitivfeldstärke über der einer freien Probe.

Bei niedrigen elektrischen Feldern ist nur die Größe des Halbzylinders unter der Elektrodenkante, die unter hoher mechanischer Zugspannung steht, wichtig und nicht die eigentliche Probengeometrie. Letztere beeinflußt die Rißbildung nur insofern, als sie das elektrische Potential ändert, das benötigt wird, um eine bestimmte Ausdehnung des Halbzylinders zu erreichen. Aus diesen Ergebnissen kann gefolgert werden, daß Risse immer an Elektrodenkanten entstehen, sofern diese innerhalb des Materials liegen und mittlere bis hohe elektrische Felder angelegt werden, sowie die Dicke des ferroelektrischen Materials einen Schwellwert überschreitet. Es existiert jedoch auch ein oberer Schwellwert über den nur die Länge der Risse zunimmt, nicht aber deren Anzahl.

Mit besseren Methoden zur Berechnung der Spannungsverteilung unter der Elektrodenkante, ist es vielleicht möglich, derartige Experimente zu benutzen, um eine Versagenswahrscheinlichkeit ähnlich der Weibull-Verteilung zu bestimmen. Da sehr viele Risse an einer Probe entstehen, müssen nur wenige Proben untersucht werden. Mit Kenntnis der vorliegenden mechanischen Spannungen, die von dem angelegten elektrischen Feldes abhängig sind, kann eine kritische Defektgröße berechnet werden. Mit der Anzahl der entstandenen Risse kann die Dichte derartiger Defekte bestimmt werden. Die Hauptschwierigkeit besteht jedoch in der Wechselwirkung der Risse untereinander und den daraus resultierenden Konsequenzen für die Spannungsverteilung.

In den beiden folgenden Teilen wurde das Rißwachstum betrachtet. Zunächst wurde das Materialverhalten bei Rißfortschritt in Form von R-Kurven in Kompaktproben gemessen. Eine ausgeprägte Dickenabhängigkeit wurde beobachtet, wobei das Materialverhalten vom vorliegenden Spannungszustand abhängt. Proben unter ebener Spannung zeichnen sich durch eine deutlich höhere Bruchzähigkeit gegenüber solchen unter ebener Dehnung aus. Der Polungszustand spielt bei 1 mm dicken Proben eine geringere Rolle als bei 3 mm dicken Proben, ist aber dennoch von Bedeutung. Die Ursache für den langen linearen Anstieg der Bruchzähigkeit ist noch nicht im Detail geklärt. Eine eingehende Untersuchung, die auch das Verhalten der Domänen gegenüber einem wachsenden Riß erklären könnte, ist hier noch nötig. Die gemessenen R-Kurven wurden für den letzten Teil der Untersuchung verwendet, bei dem die Risse elektrisch getrieben wurden.

Im letzten Teil wurde das Verhalten von Rissen gemessen und simuliert, die durch eine Dehnungsinkompatibilität zwischen dem aktiven und inaktiven Bereichen getrieben wurden. Zwei unterschiedliche Rißtypen konnten durch Variation der Polungsrichtung und Geometrie erzeugt werden, wobei die Rißpfade sehr gut reproduzierbar waren. Die Unterschiede resultieren aus der maximal möglich Dehnungsinkomptibilität, d.h. Spannung. Niedrige Spannungen führen zu einem geraden Riß mit zwei Übergängen zwischen stabilem und instabilem Rißwachstum, während hohe Spannungen zu einem umgelenkten Riß mit vier Übergängen führen. Die mechanische Spannung skaliert mit der Elektrodenbreite. Der Polungszustand wiederum beeinflußt die Spannungen derart, daß eine Polung parallel zur Elektrodenkante die Spannungen erhöhen und eine Polung senkrecht zur Elektrodenkante die Spannungen erniedrigen. Außerdem wird der Rißpfad selbst durch den Polungszustand beeinflußt.

Eine auf finiter Elemente Modellierung basierende Iterationsmethode wird benutzt, um den Rißfortschritt auch von stark gekrümmten Rissen zu simulieren. Diese bruchmechanische Analyse ist in der Lage, den Rißpfad in Abhängigkeit von der Elektrodenbreite b ebenso wie die Übergänge zwischen stabilem und instabilem Rißfortschritt zu erklären. Für eine ungepolte Probe ist die Wachstumsrichtung eines nicht abgelenkten Risses nur durch die Bedingung $K_{II} = 0$ gegeben, wie es auch bei nicht ferroelastischen Keramiken der Fall ist. Die ferroelastischen Eigenschaften manifestieren sich nicht in der Art wie sie es in gepolten Proben tun. Entsprechend wird ein komplexeres Energiekriterium benötigt um die Rißwachstumsrichtung in einer gepolten Probe zu bestimmen. Die Arbeiten dauern jedoch noch an, so daß für diesen Sachverhalt keine definitive Aussage getroffen werden kann.

Die Bedingung für stabilen Rißfortschritt bei niedrigen Geschwindigkeiten ist $K_I \geq K_R$. Im Rahmen dieser Untersuchungen konnte nicht abschließend geklärt werden, ob der Riß in Bereichen mit einem Überschuß an Rißtriebkraft wirklich instabil ist oder nur sehr schnell wächst. Letzteres wird stark angenommen, konnte jedoch nicht verifiziert werden. Eine detailliertere Untersuchung unter verschiedenen Rißfortschrittsgeschwindigkeiten ist daher geboten.

Die Ergebnisse der bruchmechanischen Untersuchung zeigen eine hervorragende Übereinstimmung mit den Experimenten bezüglich des Rißpfades, der stabilen und instabilen Bereiche und der Rißlänge in Abhängigkeit des elektrischen Feldes. Der Rißfortschritt, ob instabil oder nur sehr schnell, kann mit den in der Modellierung genutzten statischen Feldern hinreichend gut beschrieben werden.